Detection of Superparticles Beyond the Standard Model

Dissertation
zur
Erlangung des Doktorgrades (Dr. rer. nat.)
der
Mathematisch-Naturwissenschaftlichen Fakultät
der
Rheinischen Friedrich-Wilhelms-Universität Bonn

vorgelegt von
SASCHA BORNHAUSER
aus Bonn

Bonn 2008

Angefertigt mit Genehmigung der Mathematisch-Naturwissenschaftlichen Fakultät der Universität Bonn

Referent:	Prof. Manuel Drees
Korreferent:	Prof. Herbert K. Dreiner
Tag der Promotion:	02. Juli 2008

Diese Dissertation ist auf dem Hochschulschriftenserver der ULB Bonn
http://hss.ulb.uni-bonn.de/diss_online elektronisch publiziert
Erscheinungsjahr: 2008

Danksagung

Ich möchte mich bei meinen Eltern bedanken, die mich im Leben immer unterstützt haben, mit Rat zur Seite standen und immer an mich geglaubt haben. Dann will ich mich bei meinen drei „kleinen“ Brüdern bedanken, ohne die ich heute zwar noch einige hundert Millionen Nervenzellen mehr hätte, mein Leben aber auch um einiges langweiliger gewesen wäre. Sie waren immer da, wenn ich Hilfe gebraucht habe und haben mich auch immer nach Kräften unterstützt
Meinem Betreuer Herrn Prof. Manuel Drees möchte ich dafür danken, dass er es mir ermöglicht hat, in seiner Arbeitsgruppe zu promovieren, auf meine Fragen immer eine Antwort wusste und für die sehr angenehme und produktive Arbeitsatmosphäre. Im weiteren bedanke ich mich bei Herrn Prof. Herbi K. Dreiner, der sich für meine Fragen immer Zeit genommen hat und der es ermöglicht hat, dass ich im zweiten Teil meiner Promotion mit ihm und Jong Soo zusammenarbeiten konnte.
Bei Jong Soo moechte ich mich für eine kreative und produktive Zusammenarbeit bedanken und dass er mich beim Klettern nie hat abstürzen lassen.
Im besonderen bedanke ich mich bei der “Universitätsgesellschaft Bonn – Freunde, Förderer, Alumni e.V.” für die finanzielle Unterstützung meiner Promotion, die mir vieles leichter gemacht hat und durch die ich mehr meiner Zeit für meine Promotion verwenden konnte.
Ich möchte mich bei Dagmar, Patricia und Sandra bedanken, die mir immer geholfen haben, wenn ich mit irgendeinem Anliegen zu ihnen kam. Darüber hinaus möchte ich mit bei Andreas für seinen unermüdlichen Einsatz bedanken, dass wir immer möglichst optimale Arbeitsbedingungen in Hinsicht auf Hardware und Software hatten.
Zu(nahezu)letzt will ich mich bei meinen Zimmergenossen meines alten und neuen Büros und meinen Arbeitsgruppenmitgliedern bedanken, mit denen ich manche hilfreiche Diskussion hatte und oft gelacht habe.
Abschließend möchte ich mich bei allen bisher noch nicht genannten Mitglieder des Physikalischen Institutes bedanken, die mich kennen und mit denen ich in den letzten Jahren zu tun hatte. Denn zusammen mit den oben genannten Personen sorgten alle diese in der Gesamtheit für ein paar sehr schöne Jahre, die ich am PI verbringen durfte, DANKE!!!

Inhaltsverzeichnis

Abbildungsverzeichnis

Tabellenverzeichnis

1 General Introduction

1.1 Motivation

The Standard Model (SM) of particle physics being finally developed in the 1970s [87] is a relativistic, renormalizable quantum field theory which is based on the gauge group $SU(3)_C \times SU(2)_L \times U(1)_Y$. Since the SM combines the electroweak theory together with quantum chromodynamics (QCD), it describes the matter particles, leptons and quarks, and their interactions [88, 92]. Nearly all experimental results regarding the precise predictions of this theory have confirmed that these predictions are right. For example, it was possible to predict the approximate value of the top quark mass before its discovery in 1995 due to electroweak precision measurements; the reason is that the electroweak radiative corrections depends on the top quark mass, see ,e. g., [89]. However, one does not believe that the SM is the “final answer” because it has several weak points and does not provide the answers to many open questions [104, 95]; the SM does NOT

- include the fourth known fundamental interaction, gravity
- predict neutrino masses
- give an answer to the question why we have three generations of particles
- determine its 21 free parameters itself
- account for the Dark Matter in the Universe,
- give an explanation for the baryon asymmetry in the Universe

and so one.

Therefore we consider the SM usually as a low energy effective theory of a more fundamental theory and expect some kind of new physics at a higher energy scale Λ. In the context of this scale a quite serious imperfection of the SM, the so–called “SM fine–tuning” and “hierarchy problem” [76, 75], respectively, appears. On the other hand, one of the possible solutions for this problem is connected with the introduction/postulate of a new symmetry – Supersymmetry (SUSY) [57] – which leads to an extension of the particle content of the SM; the reason for this is that SUSY predicts a partner particle for each particle of the SM and therefore provides a rich new phenomenology beyond the SM. These new particles are often called “superparticles” as a whole. Great efforts have been made to detect these new particles in the last decades but until now there has been no direct experimental evidence for any of these particles [90, 91]. However, the line of argumentation within the discussion of the hierarchy problem leading to the theory of SUSY also gives rise to the strongly motivated assumption that the masses of superparticles are in the range of a few TeV [76]. This energy range will be reachable by the Large Hadron Collider (LHC) at CERN [93] which is scheduled to go on line in the end of 2008; moreover, a few future experiments [15, 14] within the context of astroparticle physics might also be able to detect the lightest supersymmetric particle. Since the topic of my PhD thesis is the detection of superparticles beyond the SM, I deal with topics of astroparticle and collider physics in the two following chapters of my thesis. Finally, I give a concluding summary of the results of these two chapters.

In the remaining part of the introduction I first give a short explanation of the hierarchy problem and why it provides a motivation for the existence of superparticles. Then I add a few quantitative results of a theory including superparticles which give additional reasons to many physicists, including myself, to believe in Supersymmetry and its impacts on particle physics. Finally, I say a few more words about SUSY with the intention to introduce the concepts of neutralinos and charginos. These two kinds of particles will play an important role in the considerations of my PhD thesis either as object of direct detection and final state particles, respectively, or exchange particles leading to corrections of certain processes with final state superparticles. I refer to [76, 75, 57], which are examples of the numerous literature on this subject, for a more precise and detailed discussion of the hierarchy problem and Supersymmetry.

1.2 Hierarchy Problem

The SM fine–tuning and the hierarchy problem, respectively, appears when we include one–loop contributions to the scalar sector (Higgs sector) of the SM and it is closely linked with the concept of symmetry. At first, we consider the photon and electron self–energy contributions as a starting point for the further discussion. The one–loop level two–point function of the photon, see Fig. 1, at vanishing external momentum is given by, see [75],

$$-4e^2 \int^{\Lambda} \frac{d^4k}{(2\pi)^4} \frac{2k^\mu k^\nu - g^{\mu\nu}(k^2 - m_e^2)}{(k^2 - m_e^2)^2} = 0\,. \tag{1}$$

Here, Λ is a cut–off parameter and m_e is the electron mass. Eq. (1) is only equal to zero if the theory, QED, is regularized in a gauge–invariant way. So the symmetry of gauge invariance, in this case the $U(1)$ gauge invariance of QED, makes sure that the photon is massless.

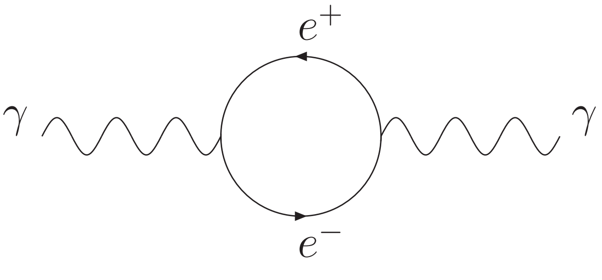

Abbildung 1: Photon self–energy at one–loop level in QED.

On the other hand, the one–loop level two–point function of the electron, see Fig. 2, at vanishing external momentum leads to a contribution of the form, cf. [75],

$$-4e^2 m_e \int^{\Lambda} \frac{d^4k}{(2\pi)^4} \frac{1}{k^2(k^2 - m_e^2)}\,. \tag{2}$$

Apparently, the correction (2) to the electron mass has a logarithmic divergence at large momenta k (four powers of k in the denominator, see,e. g., [78]):

$$\delta m \sim \alpha_{em} m_e \log \frac{\Lambda}{m_e} \,. \tag{3}$$

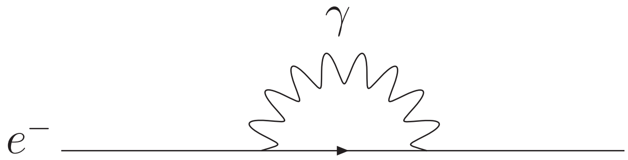

Abbildung 2: Electron self–energy at one–loop level in QED.

As mentioned in the motivation, we consider the SM as part of a larger theory; Λ denotes the scale at which this theory and the associated new physics appears and therefore the SM has to be enlarged. The largest scale in particle physics is the Planck scale where we believe that quantum gravity becomes important. The Planck scale is given by $M_P \approx 1.22 \cdot 10^{19}$ GeV[44] but even this inconceivable large number only leads to a correction of

$$\delta m \sim O(m_e/10) \,. \tag{4}$$

The origin of this protection of the electron mass is again a symmetry; the Lagrangian for QED becomes invariant under chiral rotations,

$$\psi_e \rightarrow e^{i\gamma_5 \varphi} \psi_e \,, \tag{5}$$

if $m_e \rightarrow 0$ [78]. Since the electron mass m_e is the reason that this chiral symmetry is broken, we get a correction which is just proportional to this mass.

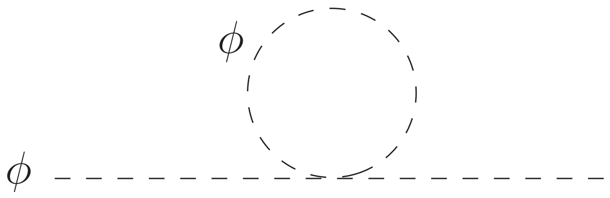

Abbildung 3: Higgs self–energy at one–loop level in the Standard Model.

Let us now consider the two–point function at one–loop level for the Higgs sector of the SM, see Fig. 3. The Higgs potential is given by, see [76],

$$V = -\mu^2 \phi^\dagger \phi + \frac{\lambda}{4} (\phi^\dagger \phi)^2 \,, \tag{6}$$

where λ is the strength of the Higgs self–interaction, $\lambda > 0$, $\mu^2 > 0$ and ϕ is the $SU(2)$ doublet Higgs field. The 4–boson self–interaction of Eq. (6) give rise to a correction, cf. [76], of the form:

$$\sim \lambda \int^{\Lambda} d^4k \frac{1}{k^2 - m_H^2} \,, \tag{7}$$

where m_H is the Higgs mass. Expression (7) is quadratically divergent (two powers of k in the denominator), and we get a correction

$$\sim \lambda\Lambda^2 \approx \lambda 1.5 \times 10^{38}\mathrm{GeV}^2 \tag{8}$$

to the $-\mu^2$ term of Eq. (6) if one replaces Λ by the Planck mass $M_P \approx 1.22 \cdot 10^{19}$ GeV. This correction is not proportional to the Higgs mass and therefore does not vanish for $m_H \to 0$ like in the case of the electron–loop contribution; one does not have a symmetry which gives rise to a protection of the Higgs mass in the SM. So we must replace $-\mu^2$ by its one–loop corrected physical value $-\mu^2_{\text{phys}}$, see [76], which is given, up to numerical factors, by

$$\mu^2_{\text{phys}} = \mu^2 - \lambda\Lambda^2 \,. \tag{9}$$

In addition $-\mu^2_{\text{phys}}$ is related to λ, cf. [76], via

$$-\mu^2_{\text{phys}} \approx \sqrt{\lambda} \cdot 123\mathrm{GeV} \,. \tag{10}$$

However, Eq. (10) imposes a quite strong restriction on the value of $-\mu^2_{\text{phys}}$ if we want to maintain the possibility of a perturbative treatment of the Higgs coupling λ [76]. This implies that we need a nearly exact cancellation of the two terms which contain respectively either the μ or λ parameter; this requires a extreme fine–tuning. In my opinion, there is no “natural” reason for this amazing cancellation.

The connection between the fine–tuning and hierarchy problem can be obtained from the following slightly different point of view: The Higgs mass m_H is connected to the parameter $-\mu^2_{\text{phys}}$, see again [76], via the relation

$$m_H = \sqrt{2} \cdot \mu_{\text{phys}} \,. \tag{11}$$

Moreover, fermion loops give rise to additional corrections of the Higgs mass, cf. Fig. 4, as well. Such contributions at one loop–level again lead to quadratic divergences which we can renormalize away, but there are still contributions of order $m_f^2 \lambda_f^2$ left [75]. These corrections are quite small as long as we only consider SM fermions with relatively small masses m_f; however, once we are taking into account fermions of a more fundamental theory at, for example, the Planck scale, one also gets large mass corrections of order M_P^2. So the question arises, why the Higgs mass is so much smaller than the Planck mass, despite these large radiative corrections. We already know a possible answer: there has to be a extreme fine–tuning in the SM between a necessarily large bare mass and the large loop corrections in order to achieve a nearly perfect cancellation.

Our introductory discussion regarding the protection of QED particle masses due to symmetries provides us with a hint for a solution of the fine–tuning and hierarchy problem, respectively: A protection of the Higgs sector of the SM from the quadratic divergences might be possible

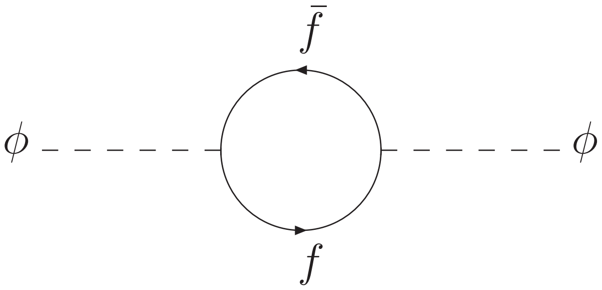

Abbildung 4: Fermion anti–fermion contribution to the self–energy of the Higgs boson.

if we can find a symmetry which groups scalar particles together with massless fermions, so that the former ones are protected against quadratic divergences via a symmetry as well [79]. Calculating the contribution of a hypothetical fermion loop which would cancel the quadratic divergences of the 4–boson self–interaction leads to the following condition for the couplings constants [76]:

$$g_f^2 = \lambda \,, \tag{12}$$

where g_f is a fermion–boson coupling. A supersymmetric theory just gives rise to fermions, called superpartners of the Higgs field, with such a adequate coupling. In addition, every SM fermion has a scalar symmetry superpartner which makes sure that the corresponding quadratic divergences of the fermion loop contributions to the Higgs mass will be canceled, see [75]. Likewise, now even the gauge bosons of the SM have superpartners because there is also the possibility of divergences due to gauge boson loops contributions to the Higgs mass. If we impose additional restrictions to the masses and couplings of these superpartners, like equal masses of the SM fermions m_f and their scalar superpartners $\tilde{m}_f$, all contributions to the Higgs mass due to radiative corrections vanish [75]. In case of a non–equality of the masses of SM particles and their partner particles we still have corrections which might be a problem if the masses of these superpartners are to high. For example, one gets a correction of order $\lambda(m_H^2 - m_f^2)\ln\lambda$ for the contribution of a hypothetical model which has one single new fermion and one Higgs [76]; this implies that the masses of the superpartners should not be higher than a few TeV because there are definitely no superpartners which have the same mass as their SM counterparts, see subsection 1.3. In the case of masses much larger than the TeV scale we would be back at a situation that we need a fine–tuning again.

The simplest possible realistic realization of supersymmetry is given within the Minimal Supersymmetric extension of the SM, the so–called MSSM [57]. The MSSM has many advantages in comparison to the SM because it provides, for example:

- a unification of the three running gauge couplings of the SM at the GUT scale [28]
- candidates for dark matter [29], which gives rise to $\sim 80\%$ of all matter in the Universe [30]
- the additional quantum correction to the anomalous magnetic moment of the muon [31]

that seems to be required by current data [32], if the SM prediction [33] based on $e^+e^- \rightarrow$ hadrons data is correct.

1.3 Supersymmetry

As motivated by the last subsection, Supersymmetry is a symmetry connecting fermions and bosons. So, if Q are the generators of this symmetry, they have to fulfil

$$Q \mid \mathrm{bosons} >= |\mathrm{fermion}> , \quad \mathrm{Q}|\mathrm{fermion} >= |\mathrm{bosons}> \ . \tag{13}$$

Since these generators connect particles which differ in spin 1/2, they are fermionic and their algebra of anticommutation ({,}) and commutation ([,]) relations is given by [75]

$$\begin{aligned} \{Q_\alpha, \bar{Q}_{\dot{\beta}}\} &= 2\sigma^\mu_{\alpha\dot{\beta}} P_\mu && (14) \\ \{Q_\alpha, Q_\beta\} &= \{\bar{Q}_{\dot{\alpha}}, \bar{Q}_{\dot{\beta}}\} = [Q_\alpha, P_\mu] = 0 \,, && (15) \end{aligned}$$

where Q is a $2-$component Weyl Spinor for the simplest choice of the SUSY generators, thus the indices α,β,$\dot{\alpha}$ and $\dot{\beta}$ run from one to two. P_μ is the momentum generator and $\sigma^\mu = (\mathbf{1}, \sigma_\mathbf{i})$, where σ_i are the Pauli matrices. The above algebra of Q and $\bar{Q}$ ($\bar{Q}$ is the conjugate of Q) is the result of the Haag–Lopuszanski–Sohnius extension [80] of the Coleman–Mandula theorem [81] which gives strong restrictions for the symmetry of a non–trivial (interacting), unitary field theory.

When we are working within the framework of a supersymmetric theory like the MSSM each particle of the SM gets a superpartner due to the connection of fermions and bosons. In case of the MSSM the matter fermions have spin zero scalar superpartners, called sfermions, which can be divided into scalar leptons (sleptons) and scalar quarks (squarks). The spin one–half superpartner of the SM gauge bosons are called gauginos. The corresponding superpartners of the eight gluons g of $SU(3)$ are the eight gluinos $\tilde{g}$. The three $SU(2)$ gauge bosons W^a have three winos $\tilde{W}^a$ as partners and finally, the bino $\tilde{B}$ is the partner of the $U(1)_Y$ gauge boson. A slight deviation from this one–to–one assignment scheme occurs in the Higgs sector of the SM, where we have to introduce a second $SU(2)$ Higgs doublet H_1^i with hypercharge $Y = -1$ at first. One of the reason for this is that without a second Higgs doublet it would be not possible to give masses to up–type as well as down–type quarks, see, e. g., 8.2 of [57]. The spin one-half superpartners of the Higgs bosons are called higgsinos. Tab. 1 shows the particle content of the MSSM.

If Supersymmetry is not broken, a superpartner would have the same mass as its SM partner particle, see, e. g., 3f. of [75]; Supersymmetry must be therefore broken, since no superpartners have been found until now [82, 83, 84]; there is certainly no selectron with a mass of 511keV. However, the problem is that is not easy to break supersymmetry spontaneously. In principle this is possible, for example via F– or D–type SUSY breaking [76], but it results in the necessity of introducing many additional superfields, which are not required for the minimal field content of MSSM. Because of this, many phenomenological analyses simply parametrize SUSY breaking by introducing by hand SUSY breaking terms into the Langrangian [57]. These terms, which are called "soft", should have positive mass dimension since such terms do not introduce new divergences and maintain the cancellation of quadratic divergences, respectively [75]. However,

Superfield	Boson Fields	Fermionic Partners	$SU(3)_C$	$SU(2)_L$	$U(1)_Y$
$\hat{G}$	g	$\tilde{g}$	8	1	0
$\hat{V}$	$W^a(W^\pm, W^0)$	$\tilde{W}^a(\tilde{W}^\pm, \tilde{W}^0)$	1	3	0
$\hat{V}'$	B	$\tilde{B}$	1	1	0
$\hat{L}$	$\tilde{L}^j = (\tilde{\nu}, \tilde{e})_L$	$(\nu, e)_L$	1	2	-1
$\hat{E}$	$\tilde{E} = \tilde{e}_R^*$	$e_R^\dagger$	1	1	$+2$
$\hat{Q}$	$\tilde{Q}^j = (\tilde{u}, \tilde{d})_L$	$(u, d)_L$	3	2	$+\frac{1}{3}$
$\hat{U}$	$\tilde{U} = \tilde{u}_R^*$	$u_R^\dagger$	3^*	1	$-\frac{4}{3}$
$\hat{D}$	$\tilde{D} = \tilde{d}_R^*$	$d_R^\dagger$	3^*	1	$+\frac{2}{3}$
$\hat{H}_1 = \hat{H}_d$	H_1^i	$(\tilde{H}_1^0, \tilde{H}_1^-)_L$	1	2	-1
$\hat{H}_2 = \hat{H}_u$	H_2^i	$(\tilde{H}_2^+, \tilde{H}_2^0)_L$	1	2	$+1$

Tabelle 1: Field content of the MSSM [76]; the superpartners of the matter fermions and gauge bosons of the SM. The first column shows the superfield which contains the corresponding boson fields and their superpartners. The last three columns show the quantum numbers of these fields with respect to the three gauge groups $SU(3)_C$, $SU(2)_L$ and $U(1)_Y$.

as a result of adding these terms we get 104 new free parameters in comparison to the SM. Apart from these parameters, the MSSM has only one last additional free parameter, the Higgsino mass term μ. The μ parameter appears in the superpotential of the MSSM, which encodes all the allowed interactions. The choice of a superpotential, which only has the minimal number of necessary terms for a realistic model, leads to the requirement of sparticle production in pairs and "R–parity" conservation, respectively, [75]:

$$R = (-1)^{3(b-l)+2s} . \tag{16}$$

Here, b is the baryon number, l is the lepton number and s the spin. A theory with R–parity conserves lepton as well as baryon number automatically. All SM particles (matter fermions, Higgs bosons and gauge bosons) have $R = +1$, whereas all SUSY particles (sfermions, higgsinos and gauginos) have $R = -1$. Therefore a sparticle only have the possibility to decay into an odd number of sparticles, that means at the same time that there is a lightest supersymmetric particle, the so–called "LSP", which cannot decay. The MSSM with conserved R–parity provides therefore a candidate for dark matter because the observations indicate that it has to be a weakly–interacting massive particle [29]; moreover, R–parity protects the proton from rapid decay, see, e. g., sec. 3 of [100] or [99]. In this PhD thesis I am working within the framework of R–parity conservation, so one always assume the existence of LSPs.

After the breaking of the electroweak symmetry $SU(2)_L \times U(1)_Y$, particles with different $SU(2)_L \times U(1)_Y$ quantum numbers but equal $SU(3)_c \times U(1)_{\rm em}$ quantum numbers as well as equal lepton number can mix. The hypercharge Y is connected to the charge Q of a particle [85] via

$$Q = I_z + \frac{Y}{2} \tag{17}$$

where I_Z is the third component of isospin.

Therefore, a look at Tab. 1 shows that, on the one hand, charged winos $\tilde{W}^{\pm}$ and charged higgsinos $\tilde{H}_2^+/\tilde{H}_1^-$ can mix. On the other hand, there is a possible mixing between the bino $\tilde{B}$, neutral wino $\tilde{W}^0$ and neutral higgsinos $\tilde{H}_1^0/\tilde{H}_2^0$. The physical mass–eigenstates of the former (latter) fields are called charginos (neutralinos).

The charged charginos $\tilde{\chi}_k^{\pm}/$ are given, see [57], by

$$\begin{aligned} \tilde{\chi}_k^+ &= \mathcal{V}_{km}\Psi_m^+ && (18) \\ \tilde{\chi}_k^- &= \mathcal{U}_{km}\Psi_m^- \,, && (19) \end{aligned}$$

where

$$\begin{aligned} (\Psi^+)^T &:= \left(\; \tilde{W}^+ , \tilde{H}_2^+ \; \right) && (20) \\ (\Psi^-)^T &:= \left(\; \tilde{W}^- , \tilde{H}_2^- \; \right) \,. && (21) \end{aligned}$$

Here, the chargino 2×2 mixing matrices $\mathcal{V}$ and $\mathcal{U}$ are defined through the diagonalisation of the chargino mass matrix:

$$\mathbf{X} = \begin{pmatrix} M_2 & \sqrt{2}M_W \sin(\beta) \\ \sqrt{2}M_W \cos(\beta) & \mu \end{pmatrix} \qquad (22)$$

where

$$\mathcal{U}^*\mathbf{X}\mathcal{V}^{-1} = M_c^D \,. \qquad (23)$$

The index k of the charginos runs from one to two and the convention was chosen in such a way that $k = 1$ is assigned to the lighter chargino.

The index n of the neutral neutralinos $\tilde{\chi}_n^0$ runs from one to four; again, the larger n the larger the mass of the corresponding neutralino. Neutralinos are Majorana particles and are determined as the eigenvalues of the mass-matrix, c. f. [57],

$$\mathcal{M}^n = \begin{pmatrix} M_1 & 0 & -M_Z\cos(\beta)\sin(\theta_W) & +M_Z\sin(\beta)\sin(\theta_W) \\ 0 & M_2 & +M_Z\cos(\beta)\cos(\theta_W) & -M_Z\sin(\beta)\cos(\theta_W) \\ -M_Z\cos(\beta)\sin(\theta_W) & +M_Z\cos(\beta)\cos(\theta_W) & 0 & -\mu \\ +M_Z\sin(\beta)\sin(\theta_W) & -M_Z\sin(\beta)\cos(\theta_W) & -\mu & 0 \end{pmatrix} \,. \qquad (24)$$

Again one requires the diagonalisation of the mass matrix with help of a 4×4 matrix Z:

$$Z^*\mathcal{M}^n Z^{-1} = \mathcal{M}_n^D \,. \qquad (25)$$

Therefore the four neutralinos are given for the binobasis by

$$\tilde{\chi}_n^0 \;=\; Z_{nl}\Psi_l^0 \,, \tag{26}$$

where

$$(\Psi^0)^T \;:=\; \left(\; \tilde{B},\tilde{W}^0,\tilde{H}_1^0,\tilde{H}_2^0 \;\right) \,. \tag{27}$$

Above, the quantities in the chargino (22) and neutralino (24) mass matrix are the masses of the $W^\pm$ and Z bosons M_W, M_Z, the Weinberg-angle θ_W, the ratio between the vacuum expectation values v_i of the Higgs fields $\tan\beta = v_2/v_1$; finally, M_1, M_2 are the $SU(1)_Y$ and $SU(2)_L$ gaugino mass parameters

Therefore the masses and the mixing–angles of the charginos and neutralinos are defined completely through the four parameters $\tan(\beta)$, M_1, M_2 and μ. The three last–mentioned mass parameters are, in general, completely arbitrary. Though you can further restrict this parameter space by assumption of equal gaugino masses M_i at the GUT scale ($M_G \approx 10^{16}$ GeV). This is motivated by the, already mentioned shortly in the last subsection, observation that the three gauge couplings apparently unify at this scale [78], if you take their experimental values at the scale M_Z and continue these values to higher energies with aid of the renormalization group equations (RGEs) [86].

$M_1 = M_2$ at the scale M_G implies now [75]

$$M_1(M_Z) = \frac{5}{3}\tan^2(\theta_W)M_2(M_Z) \simeq \frac{1}{2}M_2(M_z) \,, \tag{28}$$

the factor $\frac{5}{3}$ shows up by the difference in the normalization of a simply unifying gauge group, the GUT, and the electroweak hypercharge generator in the SM. With aid of Eq. (24) and (28) one can consider two special cases of components–mixing which give rise to different lightest neutralinos $\tilde{\chi}_1^0$ [75]:

1. $\boxed{|\mu| \ll |M_{1,2}|}$: The two lightest neutralinos and the lightest chargino have a higgsino dominated mixing, that means that the higgsino–fields give the main contribution to the linear combination of the corresponding physical mass eigenstates. So the masses of these three particles are nearby the higgsino mass parameter $|\mu|$. By contrast, the heavy chargino is quasi the charged wino field and the two heavy neutralinos are also dominated by the neutral gaugino fields.

2. $\boxed{|\mu| \gg |M_{1,2}| \gg |M_Z|}$: The two lightest neutralinos are gaugino dominated in their mixing, in consideration of Eq. (28) they are quasi the pure bino and wino field, respectively, and the two heaviest neutralinos are dominated in their mixing by the higgsino fields. Moreover, the lightest chargino is quasi the charged wino and the heavy chargino is mainly the charged higgsino. It holds the follwing equations for their masses:

$$M_{\tilde{\chi}_k^\pm} \simeq M_{\tilde{\chi}_2^\circ} \simeq 2M_{\tilde{\chi}_1^0} \quad \text{and} \quad |\mu| \simeq \mathrm{M}_{\tilde{\chi}_3^\circ} \simeq \mathrm{M}_{\tilde{\chi}_4^\circ} \simeq \mathrm{M}_{\tilde{\chi}_2^\pm} \gg \mathrm{M}_{\tilde{\chi}_1^\pm}$$

Teil I

Astroparticle Physics

2 Introduction Chapter I

Every square meter at the top of the Earth's atmosphere is hit by thousends of cosmic ray (CR) particles per second. The energy spectrum of the CRs runs from 1 to beyond 10^{11} GeV. The flux rate for the tail of the spectrum is very low; particles with energy 10^{11} GeV or higher, the so–called ultra high energy (UHE) component of the CRs, occur at a rate of about 1 per km^2 per 100 years [77]. Nevertheless, they have been detected by every major cosmic ray experiment like Fly's Eye [54], AGASA [55] or Auger [69]. This raises the question of the origin of the UHE CRs. The efforts to answer this question can be roughly assigned to two classes of models.

The first class consists of more conventional, so–called "bottom–up", scenarios [1] describing the acceleration of charged particles in special astrophysical environments like supernova remnants or active galactic nuclei (AGNs). However, the problem of these scenarios is to find astronomical objects which are able to accelerate ultra–relativistic charged particles to the needed energies; this requires a sufficiently strong magnetic field which extends over a sufficiently large space volume. In this context it is important to know if the distribution of the arrival directions of UHE events is homogeneous or not. The former case would exclude one or a few local point sources; the reason is that even charged UHE particles like protons would not be deflected much by the magnetic fields in our galaxy. A largely homogeneous distribution can be produced by a large group of very distant sources like, for example, AGNs. But the particles which are produced at such very large distances should not be able to reach us without losing a good portion of their energy. The reason for this is that all known UHE particles which interact high in the atmosphere (as required by observation) lose their energy through inelastic scattering on the photons of the cosmic microwave background (CMB); this is known as the GZK [2] effect;

protons with $E \gtrsim 5 \cdot 10^{10}$ GeV lose their energy via

$$\begin{array}{rcl} p + \gamma_{2.7K} & \rightarrow & n + \pi^+ \\ & \rightarrow & p + \pi^0 \,, \end{array}$$

the flux of photons with $E \gtrsim 10^6$ GeV is depleted through the reaction

$$\gamma + \gamma_{2.7K} \rightarrow e^+ + e^-$$

and heavier ions suffer break–up reactions on CMB photons. In consequence of the GZK effect all these UHE particles are not able to travel over distances exceeding ~ 50 Mpc [56]. Moreover, they should still point back approximately to their sources since intergalactic magnetic fields should not be able to randomize the arrival directions of UHE particles over such distances. Until recently, there was no assured connection between known near sources of high–energy particles and the directions of the most energetic events. However, the current results of Auger indicate a correlation between nearby AGNs and the origin of these events [70].

The second class consists of the so–called "top–down" models [71, 72]. These models postulate the existence of superheavy, yet long–lived particles, so–called "X particles". The decay of these particles then gives rise to the UHE CRs since it causes a parton cascade, followed by hadronization and the decay of the unstable particles. The lower bond on the mass of the X particles is $M_X \gtrsim 10^{12}$ GeV, since the most energetic CR event that has been observed to date has $E \simeq 3 \cdot 10^{20}$ eV [4]. Since UHE CR are observed today, the lifetime of a X particle must be at least comparable to the age of the Universe. Several particle physics models containing candidates with sufficiently large mass and long lifetime have been suggested [1, 5]. For example, X particles could be associated with a Grand Unified theory and their required long lifetime can be achieved by embedding them into topological defects. The X particles would have been produced in the very early Universe [3, 6] due to the – more than one hundred orders of magnitude – higher energy density, as compared to our today's Universe, just after inflation.

On the one hand, top–down models can be made compatible with all existing data, including the first data from the Pierre Auger observatory [7]. But, on the other hand, one has two different classes of models (top–down and bottom–up), so we have to find a way to distinguish between these classes. One possibility might be a discrimination due to slightly different spectra for neutrinos and photons at high energies, and/or different distributions of the arrival directions. A necessary requirement for top–down models would be the detection of some very energetic neutrinos because these models predict an UHE neutrino flux which is even larger than the photon flux. But it is not easy to distinguish between UHE protons and photons, and bottom–up models also lead to a sizeable UHE neutrino flux, for example because of the GZK effect itself. In case of a possible discrimination due to the arrival directions there might be indeed anisotropies for top–down models [9] if X particles are distributed like Dark Matter in our galaxy. But the problem is that one has to know the distribution of the matter near the galactic center, which is not well known, in order to specify quantitative predictions.

By reason of these difficulties one is anxious to find signals where bottom–up and top–down models make *qualitatively* different predictions. One possibility opens up if we are taking into account the potential existence of Supersymmetry and superparticles, respectively. Independent of the primary decay mode of the X particle there will be a large number of superparticles; the reasons for this is that the mass M_X is much larger than the sparticle mass scale and if one has primary decay into SM particles, superparticles will be produced in the subsequent parton shower [10, 11]. Under the assumption of $R-$parity conservation, all these superparticles will decay into stable lightest superparticles (LSPs), which are assumed in this PhD thesis to be the lightest of the four neutralinos. On the other hand, bottom–up models will only give rise to a marginal flux of superparticles; the reason is that nearly all interactions of UHE photons and protons only lead to new light particles due to the very small total cross section for the production of superparticles (even at such high energies).

So a "smoking gun" signature for top–down scenarios is the detection of UHE neutralino LSPs. But we have to remember that we obtain UHE neutrinos as well as UHE neutralino LSPs at the location of a X particle decay since both are stable final state particles of the decay cascade. In addition, both particles are weakly interacting, so we have to find a way to distinguish them from each other. In this context, the crucial observation [12] is that the Earth is opaque for neutrinos of a certain energy range, but neutralinos are still able, even though they might lose a part of their energy, to traverse it. This is the result of a larger neutrino–nucleon two–to–two scattering cross section, and/or the larger neutrino energy loss per interaction, cf. [13]. Therefore UHE neutralino LSPs can still give rise to a measurable upgoing air shower event of high energy, see [12, 16, 17] as examples of existing analyses. The total neutralino LSP flux is conserved because its interactions give rise to either the lightest neutralino or a heavier superparticle, which will decay back into the lightest neutralino; thus the interactions of a neutralino LSP flux only lead to shift of the flux to lower energies, which makes the detection of the neutralino LSPs more difficult.

Intended future satellite experiments like OWL [14] and EUSO [15], observing fluorescence in the atmosphere of the Earth, will be able to detect a surface area up to $\mathcal{O}(10^6)$ km^2 simultaneously. The central point of this first chapter is the calculation of the neutralino LSP event rates for these future cosmic ray detectors, including the neutrino background. In conjunction with this aim, we describe neutralino LSP and neutrino propagation through matter by means of transport equations. This offers the possibility to use our results as well for event rates calculation with respect to the Moon.

A promising idea, which was first suggested by Dagkesamanskii and Zheleznyk [73], for the detection of UHE particle fluxes is the measurement of radio waves when these particles hit the Moon [74]. These radio waves are produced due to the Askaryan effect [68] and the emission of Cerenkov radiation, respectively. UHE particles cause a cascade of secondary particles when they are interacting in the Moon's matter. This cascade develops a cloud of negative charge in a dense dielectric medium because electrons are entrained from the surrounding matter. As a result, Cerenkov light is produced since these electrons are moving with a velocity which is faster than the velocity of light in the medium. Coherence builds up for the range of wavelengths which is about the dimension of the cloud; the wavelengths of radio frequencies are just comparable to the dimension of the electron shower [64]. Therefore we can use a part of the outer layer of the Moon as an effective detector volume of the order of 100 teratons.

This first chapter is organized as follows. The derivation and solution of the transport equations for neutralino LSP and neutrino fluxes is described in section 3. Here, we consider bino– as well as higgsino–like neutralino LSPs and include for the tau neutrino flux the energy loss of the tau leptons, which are produced by charged current interactions, before they decay back to neutrinos. Section 4 deals with the calculation of the event rates; at first we consider the usage of the Earth's matter as a filter and detector volume, then we go on with the calculation of the event rates for the Moon. In section 5 we present our numerical results for both the Earth and the Moon. We find that it might be possible to detect higgsino–like neutralino LSP fluxes impinging on the Earth if we consider a satellite experiment which can monitor at least a few 10^5 km^2 of the Earth's surface; bino–like neutralino LSP fluxes most likely remain out of reach even for an experiment which can monitor a surface area of 10^6 km^2. Moreover, an experiment which detects radio waves and covers half of the Moon's surface might be able to detect UHE neutrinos which interact in the Moon's matter; on the other hand, a successful detection might be only possible for higgsino–like neutralino LSP fluxes, but not for bino–like neutralino LSPs. The final section 9 of this thesis will give a closing summary and conclusion of the first and second chapter.

3 Transport Equations

The final aim of this chapter, based on the idea of using the Earth's and Moon's matter as a detector volume, is the calculation of event rates with respect to neutrino and neutralino LSP fluxes. The knowledge of these fluxes for a given energy E and matter depth X is part and parcel of this calculation. The latter quantity is customarily given as a column depth, measured in g/cm^2 or, in natural units, in GeV^3. For example, a neutrino travelling a distance of 100 cm through a medium of density 30 g/cm^3 has a column depth of $X = 3000$ g/cm^2. Therefore this section deals with the derivation and the solution of the so–called "transport equations", which describe the propagation of UHE neutralino LSPs and neutrinos through matter. A short derivation of the required total and differential cross sections for the scattering of UHE neutralinos LSPs on nuclei is given in appendix A. In the following we will consider scenarios where the total cross section is dominated by either $s-$ or $t-$channel contributions (for a definition of these terms see, e. g. , [78]). This corresponds to scenarios with a bino- and higgsino-like LSP, respectively, see appendix B.1 for a short explanation. Thus we will deal the cases of the transport equations for $s-$ and $t-$channel scattering separately, where the former interaction channel is only possible for neutralino LSPs.

3.1 Transport Equation for $s-$Channel Scattering

The aim of this subsection is to compute the differential neutralino LSP flux $F_{\tilde{\chi}_1^0}$ for each possible value of the LSP energy E and the above mentioned column depth X. Since a UHE LSP of energy E interacting with matter at rest can only lose energy, there is always a reduction of $F_{\tilde{\chi}_1^0}(E)$ for fixed energy E. The key quantity for the description of this effect is the so–called "interaction length" $\lambda_{\tilde{\chi}_1^0}$, which is given by

$$\lambda_{\tilde{\chi}_1^0}(E)^{-1} = N_A \sigma^{\text{tot}}_{\tilde{\chi}_1^0 N}(E)\,, \tag{29}$$

where $N_A = 6.022 \times 10^{23}$ g^{-1} is Avogadro's number, and in the given scenario $\sigma^{\text{tot}}_{\tilde{\chi}_1^0 N} \simeq \sigma^{\text{tot}}_s$ of Eq.(105) of appendix B. On the other hand, $F_{\tilde{\chi}_1^0}(E)$ can be *increased* by the interactions of LSPs which have a larger energy than E; when a LSP looses the fraction y of its energy because of an interaction with matter, it will increase $F_{\tilde{\chi}_1^0}(E)$ if it had the initial energy $E_y \equiv E/(1-y)$. Therefore one needs for the $s-$channel description of the change of differential flux two terms,

$$\frac{\partial F_{\tilde{\chi}_1^0}(E,X)}{\partial X} \;=\; -\frac{F_{\tilde{\chi}_1^0}(E,X)}{\lambda_{\tilde{\chi}_1^0}(E)} + \frac{1}{\lambda_{\tilde{\chi}_1^0}(E)} \int_0^{y_{\max}} \frac{dy}{1-y} K_s(E,y) F_{\tilde{\chi}_1^0}(E_y,X)\,, \tag{30}$$

describing the reduction (the first term of the left hand side of Eq. (30)) and the regeneration (the second term of the left hand side of Eq. (30)) of the flux. The integration kernel is determined by the differential cross section given in Eq.(110) of appendix A:

$$K_s(E,y) \;=\; \frac{1}{\sigma_s^{\text{tot}}(E)} \frac{d\sigma_s(E_y)}{dy}\,, \tag{31}$$

and $y_{\max}$ has been given in Eq.(111) of A. The above mentioned second term is the result of a convolution between $F_{\tilde{\chi}_1^0}(E,X)$ and $d\sigma_s(E)/dy$ However, note that Eq.(30) assumes collinear kinematics, where the produced LSP goes in the same direction as the original one. But the scattering angle of ultra–relativistic LSPs is given by

$$\theta \lesssim m_{\tilde{q}}/E_{\rm in} \lesssim 10^{-3} \tag{32}$$

for energies of interest, thus this assumption is justified.

As shown in [13] we cannot use the standard solution method for the analogous transport equation for neutrinos, basing on an iteration method [60, 61, 62], because it badly violates flux conservation, cf. section 3.4. So we use a first order Taylor expansion for the numerical solution of the transport equation (30):

$$F_{\tilde{\chi}_1^0}(E, X + dX) = F_{\tilde{\chi}_1^0}(E, X) + dX \frac{\partial F_{\tilde{\chi}_1^0}(E, X)}{\partial X} + \cdots . \tag{33}$$

We found that a more sophisticated algorithm, e.g. the Runge–Kutta method, does not offer much of an advantage in terms of accuracy achieved for a fixed CPU time spent. We parametrize $F_{\tilde{\chi}_1^0}(E)$ for given X as cubic spine. Note that the second term of Eq. (33) is just given by the right hand side of Eq. (30) times a stepsize dX. For example, if we divide X into 10^4 steps one gets $dX = X/10^4$.

3.2 Transport Equation for $t-$Channel Scattering

In case of $t-$channel scattering we consider the transport equations for neutrino and neutralino LSP fluxes. The first part of this subsection describes the derivation of the solution for a neutralino LSP flux; the second part deals with the changes, especially the treatment of energy loss of taus in matter, of this solution when considering a neutrino flux.

A higgsino–dominated LSP has a total cross section being dominated by charged and neutral current $t-$channel scatterings which predominately lead to the production of $\tilde{\chi}_2^0$ and $\tilde{\chi}_1^\pm$, see appendix B. So we will ignore the contributions from all other final states.

Since the interactions of the $\tilde{\chi}_1^0$ flux with matter leads to fluxes of $\tilde{\chi}_1^\pm$ and $\tilde{\chi}_2^0$, collectively denoted by $\tilde{\chi}_{\rm out}$, we would actually need three coupled transport equations; this would be similar to the two coupled transport equations in case of ν_τ propagation [61, 62], describing the changes of the ν_τ and tau flux. In order to avoid this, we are assuming that these heavier produced particles, $\tilde{\chi}_2^0$ and $\tilde{\chi}_1^\pm$, decay well before they lose a significant fraction of their energy through interactions. Since this assumption is even true for τ leptons of the relevant energy, it is also acceptable for $\tilde{\chi}_1^\pm$ and $\tilde{\chi}_2^0$; these states have a much shorter lifetimes (by a factor of order $(m_{\tilde{\chi}_{\rm out}} - m_{\tilde{\chi}_1^0})^5/m_\tau^5$) for our considered scenarios and significantly shorter decay lengths for a given lifetime (due to their larger masses, i.e. smaller γ factors).

This gives rise to three terms describing the change of the differential flux $F_{\tilde{\chi}_1^0}(E, X)$. The first one again describes the reduction of the flux $F_{\tilde{\chi}_1^0}(E, X)$ due to interactions in matter; the second and third one describe the regeneration of the $F_{\tilde{\chi}_1^0}(E, X)$ as a result of the decay of $\tilde{\chi}_1^\pm$ and $\tilde{\chi}_2^0$, which are produced because of charged and neutral current interactions; we convolute the $\tilde{\chi}_{\rm out}$ production and decay spectra for the calculation of the two integration kernels. Therefore, the $s-$ and $t-$channel scattering transport equations are very similar, and the latter one is given by

$$\begin{aligned}\frac{\partial F_{\tilde{\chi}_1^0}(E,X)}{\partial X} &= -\frac{F_{\tilde{\chi}_1^0}(E,X)}{\lambda_{\tilde{\chi}_1^0}(E)} + \frac{1}{\lambda_{\tilde{\chi}_1^0}(E)} \int_0^1 \frac{dy}{1-y} K_{\tilde{\chi}_1^0}^{NC}(E,y) F_{\tilde{\chi}_1^0}(E_y,X) \\ &\quad + \frac{1}{\lambda_{\tilde{\chi}_1^0}(E)} \int_0^1 \frac{dy}{1-y} K_{\tilde{\chi}_1^0}^{CC}(E,y) F_{\tilde{\chi}_1^0}(E_y,X)\,, \end{aligned} \tag{34}$$

where the interaction length $\lambda_{\tilde{\chi}_1^0}$ has been given by Eq.(29). The integration kernels are most easily written as convolutions in the variable $z = E_{\tilde{\chi}^0_{1,\mathrm{out}}}/E_{\tilde{\chi}^0_{1,\mathrm{in}}} = 1-y$:

$$\begin{aligned} K_{\tilde{\chi}_1^0}^{NC,CC}(E,y) &= \frac{1}{\sigma_t(E)} \int_{z_{1,\min}}^{z_{1,\max}} dz_1 \int_{z_{2,\min}}^{z_{2,\max}} dz_2 \delta(z - z_1 z_2) \frac{d\sigma^{NC,CC}(E_y,z_1)}{dz_1} \frac{1}{\Gamma} \frac{d\Gamma(z_1 E_y, z_2)}{dz_2} \Bigg|_{y=1-z} \\ &= \frac{1}{\sigma_t(E)} \int_{z}^{z_{1,\max}} \frac{dz_1}{z_1} \frac{d\sigma^{NC,CC}(E_y,z_1)}{dz_1} \frac{1}{\Gamma} \frac{d\Gamma(z_1 E_y, \frac{z}{z_1})}{dz_2} \theta(z - z_{\min}) \theta(z_{\max} - z) \Bigg|_{y=1-z} . \end{aligned} \tag{35}$$

The limits $z_{1,\min,\max}$ for the outer integration in the first line of Eq.(35) follow from Eq.(122) of appendix A with $x \to 1$, i.e. $\hat{s} \to s = 2E_y m_N + m^2_{\tilde{\chi}_1^0}$. The limits for the inner integration follow from $\tilde{\chi}_{\mathrm{out}}$ decay kinematics described below. $z_1 = E_{\tilde{\chi}_{\mathrm{out}}}/E_{\tilde{\chi}^0_{1,\mathrm{in}}}$ describes the energy transfer from the incoming lightest neutralino to the heavier neutralino or chargino, and $z_2 = E_{\tilde{\chi}^0_{1,\mathrm{out}}}/E_{\tilde{\chi}_{\mathrm{out}}}$ describes the energy transfer from this heavier neutralino or chargino to the lightest neutralino produced in its decay. z_2 is chosen such that $z \equiv z_1 z_2 = 1-y$; the $\theta-$functions in the second line of Eq.(35) ensure that y lies within the kinematical limits, with $z_{\min} = z_{1,\min} z_{2,\min}$ and $z_{\max} = z_{1,\max} z_{2,\max}$. Note that both integration kernels in Eq.(34) are normalized to the *total* $\tilde{\chi}_1^0-$nucleon scattering cross section, which is here approximated by the $t-$channel contribution given by Eq.(112) appendix of A. Note that Eq.(34) again assumes collinear kinematics, where the LSP produced in $\tilde{\chi}_{\mathrm{out}}$ decay goes into the same direction as the original LSP.

The missing piece in Eq.(35) is the differential decay spectrum of the produced $\tilde{\chi}_{\mathrm{out}}$. Under the assumption of scenarios with small $\tilde{\chi}_{\mathrm{out}} - \tilde{\chi}_1^0$ mass difference for higgsino–like LSP, cf. Tab. 13 of appendix A, we only need to consider three–body decays, $\tilde{\chi}_{\mathrm{out}} \to \tilde{\chi}_1^0 f_1 f_2$, where f_1, f_2 are two SM (anti)fermions whose masses we neglect. In the $\tilde{\chi}_{\mathrm{out}}$ rest frame one then has:

$$\frac{d\Gamma}{dE^*_{\tilde{\chi}_1^0}} = \frac{1}{8 m_{\tilde{\chi}_{\mathrm{out}}} (2\pi)^3} \int_{E^*_{f,\min}}^{E^*_{f,\max}} dE^*_f |\mathcal{M}|^2 \,, \tag{36}$$

where E^*_f is the energy of one of the two massless (anti)fermions (the energy of the other being determined by energy conservation). The integration limits in Eq.(36) are given by

$$E^*_{f\,\substack{\min\\ \max}} = \frac{2 m_{\tilde{\chi}_{\mathrm{out}}} E^*_{\tilde{\chi}_1^0} - m^2_{\tilde{\chi}_1^0} - m^2_{\tilde{\chi}_{\mathrm{out}}}}{2E^*_{\tilde{\chi}_1^0} - 2m_{\tilde{\chi}_{\mathrm{out}}} \pm 2\sqrt{E^{*2}_{\tilde{\chi}_1^0} - m^2_{\tilde{\chi}_1^0}}} \,. \tag{37}$$

The total $\tilde{\chi}_{\mathrm{out}}$ decay width Γ appearing in Eq.(35) can be obtained by integrating Eq.(36) over $E^*_{\tilde{\chi}_1^0}$, the lower and upper integration limit being given by $m_{\tilde{\chi}_1^0}$ and $(m^2_{\tilde{\chi}_1^0} + m^2_{\tilde{\chi}_{\mathrm{out}}})/(2m_{\tilde{\chi}_{\mathrm{out}}})$, respectively.

In order to boost into the frame where $\tilde{\chi}_{\text{out}}$ has energy energy $E_{\tilde{\chi}_{\text{out}}}$, we have to know the angular distribution of the produced $\tilde{\chi}_1^0$ in the $\tilde{\chi}_{\text{out}}$ rest frame relative to the $\tilde{\chi}_{\text{out}}$ flight direction. Here we assume an isotropic distribution, which is appropriate for an unpolarized $\tilde{\chi}_{\text{out}}$, and also if $\tilde{\chi}_{\text{out}}$ decays via a pure vector coupling. This yields

$$\frac{d\Gamma}{dE_{\tilde{\chi}_1^0}} = \int_{E^*_{\tilde{\chi}_1^0,\min}}^{E^*_{\tilde{\chi}_1^0,\max}} dE^*_{\tilde{\chi}_1^0} \frac{m_{\tilde{\chi}_{\text{out}}}}{E_{\tilde{\chi}_{\text{out}}}} \frac{1}{\beta\sqrt{E^{*2}_{\tilde{\chi}_1^0} - m^2_{\tilde{\chi}_1^0}}} \frac{1}{16 m_1 (2\pi)^3} \int_{E^*_{f,\min}}^{E^*_{f,\max}} dE^*_f |\mathcal{M}|^2 \,. \tag{38}$$

The limits for the inner integration in Eq.(38) have been given in Eq.(37), and the limits for the outer integration are:

$$\begin{aligned} E^*_{\tilde{\chi}_1^0,\min} &= \gamma\left(E_{\tilde{\chi}_1^0} - \beta\sqrt{E^2_{\tilde{\chi}_1^0} - m^2_{\tilde{\chi}_1^0}}\right) , \\ E^*_{\tilde{\chi}_1^0,\max} &= \frac{m^2_{\tilde{\chi}_{\text{out}}} + m^2_{\tilde{\chi}_1^0}}{2m_{\tilde{\chi}_{\text{out}}}} \,. \end{aligned} \tag{39}$$

Here, and in Eq.(38), $\gamma = 1/\sqrt{1-\beta^2} = E_{\tilde{\chi}_{\text{out}}}/m_{\tilde{\chi}_{\text{out}}}$. Notice that $E^*_{\tilde{\chi}_1^0,\min}$ reduces to the absolute kinematical minimum of $m_{\tilde{\chi}_1^0}$ for $E_{\tilde{\chi}_1^0} = \gamma m_{\tilde{\chi}_1^0}$, whereas $E^*_{\max}$ is always determined from the $\tilde{\chi}_{\text{out}}$ decay kinematics, independent of $E_{\tilde{\chi}_1^0}$. Finally, in the relevant limit $\gamma \gg 1$ the limits on the energy $E_{\tilde{\chi}_1^0}$ of the LSP produced in $\tilde{\chi}_{\text{out}}$ decay are

$$\begin{aligned} E_{\tilde{\chi}_1^0,\min} &= \frac{\gamma\left[m^2_{\tilde{\chi}_1^0} + m^2_{\tilde{\chi}_{\text{out}}} - \beta\left(m^2_{\tilde{\chi}_{\text{out}}} - m^2_{\tilde{\chi}_1^0}\right)\right]}{2m_{\tilde{\chi}_{\text{out}}}} \longrightarrow \gamma\frac{m^2_{\tilde{\chi}_1^0}}{m_{\tilde{\chi}_{\text{out}}}} , \\ E_{\tilde{\chi}_1^0,\max} &= \frac{\gamma\left[m^2_{\tilde{\chi}_1^0} + m^2_{\tilde{\chi}_{\text{out}}} + \beta\left(m^2_{\tilde{\chi}_{\text{out}}} - m^2_{\tilde{\chi}_1^0}\right)\right]}{2m_{\tilde{\chi}_{\text{out}}}} \longrightarrow \gamma m_{\tilde{\chi}_{\text{out}}} = E_{\tilde{\chi}_{\text{out}}} \,. \end{aligned} \tag{40}$$

Now we turn to the modifications of our above results when considering neutrino fluxes. In the case of muon and electron neutrino fluxes we get a simplified version of Eq.(34):

$$\frac{\partial F_{\nu_{\mu,e}}(E,X)}{\partial X} = -\frac{F_{\nu_{\mu,e}}(E,X)}{\lambda_{\nu_{\mu,e}}(E)} + \frac{1}{\lambda_{\nu_{\mu,e}}(E)} \int_0^1 \frac{dy}{1-y} \frac{d\sigma^{NC}_{\nu_{\mu,e}}(E_y,y)}{dy} F_{\nu_{\mu,e}}(E_y,X) \,. \tag{41}$$

Beside the logical replacement of $\tilde{\chi}_1^0$ by ν cross sections, the integration kernel for the neutral current interactions $K^{NC}(E,y)$ is substituted by the corresponding differential cross section $d\sigma^{NC}_{\nu_{\mu,e}}(E_y,y)/dy$. The reason for this is that a neutral current interaction gives rise to a neutrino immediately without the detour of a decaying particle. The second regeneration term of the right hand side of Eq. (34) does not exist anymore; the reason is that electrons and muons, produced by charged current interaction, do not contribute to the regeneration of the corresponding neutrino flux. On this account the Earth is opaque for these fluxes so we can neglect them for the event rate calculation. By contrast, the tau neutrino flux have a regeneration due to charged current interactions and the short lifetime of the tau, respectively. So the transport equation for tau neutrinos reads as follows:

$$\begin{aligned} \frac{\partial F_{\nu_\tau}(E,X)}{\partial X} &= -\frac{F_{\nu_\tau}(E,X)}{\lambda_{\nu_\tau}(E)} + \frac{1}{\lambda_{\nu_\tau}(E)} \int_0^1 \frac{dy}{1-y} \frac{d\sigma^{NC}_{\nu_\tau}(E_y,y)}{dy} F_{\nu_\tau}(E_y,X) \\ &\quad + \frac{1}{\lambda_{\nu_\tau}(E)} \int_0^1 \frac{dy}{1-y} K^{CC}_{\nu_\tau}(E,y) F_{\nu_\tau}(E_y,X) \,, \end{aligned} \tag{42}$$

Here, $K_{\nu_\tau}^{CC}$ is the integration kernel for the decay of taus and it is given by Eq.(35) if we do not account a energy loss of the tau while traversing the Earth's or Moon's matter before it decay back into a tau neutrino.

However, since we are interested in very high energies, the tau leptons produced in charged current ν_τ reactions may lose a significant fraction of their energy before decaying. Therefore we modify the integration kernel $K_{\nu_\tau}^{CC}$ in order to at least crudely estimate the effects of τ energy loss in matter. We do this by formally treating this energy loss as additional scattering:

$$\frac{1}{\sigma(E_y)}\frac{d\sigma(E_y,z)}{dz} \rightarrow \int \frac{1}{\sigma(E_y)}\frac{d\sigma(E_y,z_1)}{dz_1}\frac{1}{L}\frac{dL(z_1E_y,E'')}{dE''}dE''\bigg|_{z=E''/E} . \tag{43}$$

Here the function $dL(E_{\tau,\text{in}},E_{\tau,\text{out}})/dE_{\tau,\text{out}}$ describes the τ energy loss. We make the very simple ansatz [22]

$$\frac{dE_\tau}{dz} = -\beta\rho E_\tau \quad \text{with } \beta = 0.85\cdot 10^{-6}\text{cm}^2\text{g}^{-1} = \text{const.} \tag{44}$$

This implies $E_\tau(z) = E_\tau(0)\text{e}^{-\beta\rho z}$. We assume that all τs decay after traveling a distance $z_{\text{dec}} = E_\tau c\tau_\tau/m_\tau$, where τ_τ is the lifetime of the τ lepton and c is the speed of light. Note that we estimate the average decay length from the τ energy *after* propagation. This underestimates the decay length, and hence the effect of τ energy loss. On the other hand, for $E_{\nu_\tau} < 10^{10}$ GeV the ansatz (44) overestimates the energy loss [22]. Our approximation of a fixed decay length leads to

$$\frac{dL(E',E'')}{dE''} = \delta\left(E'' - E'\exp(-\kappa E'')\right) , \tag{45}$$

with constant $\kappa = \beta\rho c\tau_\tau/m_\tau$. The integral over dL/dE'', which appears in Eq.(43), is then given by:

$$L = \int dE''\delta(E'' - E'\exp(-\kappa E'')) = \frac{1}{1+\kappa E'\exp(-\kappa E'')} , \tag{46}$$

where in the last expression E'' has to be interpreted as a function of E', as determined by the argument of the $\delta-$function. We can then evaluate the integral in Eq.(43):

$$\frac{1}{\sigma(E_y)}\frac{d\sigma(E_y,z)}{dz} \rightarrow (1+\kappa z_1 E_y)\exp(\kappa z_1 E_y)\frac{1}{\sigma(E_y)}\frac{d\sigma(E_y,z')}{dz'}\bigg|_{z'=z_1\exp(\kappa z_1 E_y)} . \tag{47}$$

The obvious advantage of our simplified treatment is that it does not necessitate the numerical evaluation of additional integrals. This would have been very costly, since the length scales involved in τ energy loss and decay (a few km for $E_\tau \sim 10^8$ GeV) are very much shorter than the ν_τ interaction length in rock ($\sim 10^3$ km for $E_{\nu_\tau} = 10^8$ GeV) [22]. A more accurate treatment would therefore have required to use many more steps in X when integrating the transport equation; even with out simple treatment, or indeed without including the effects of τ energy loss, calculating the ν_τ flux emerging from Earth takes up to several CPU days. On the other hand, our simplified treatment can only give us an indication of the size of effects due to τ energy losses. We find that the effect on the ν_τ flux emerging from Earth is essentially negligible for $E_{\nu_\tau} \lesssim 10^7$ GeV. This is also true for $X \gtrsim 0.45X_{\max}$, since then the flux at $E_{\nu_\tau} > 10^7$ GeV is negligible even if the τ energy loss is ignored. However, it can reduce the ν_τ flux by a factor of two or more at large E_{ν_τ} and small X, cf. Fig. 5.

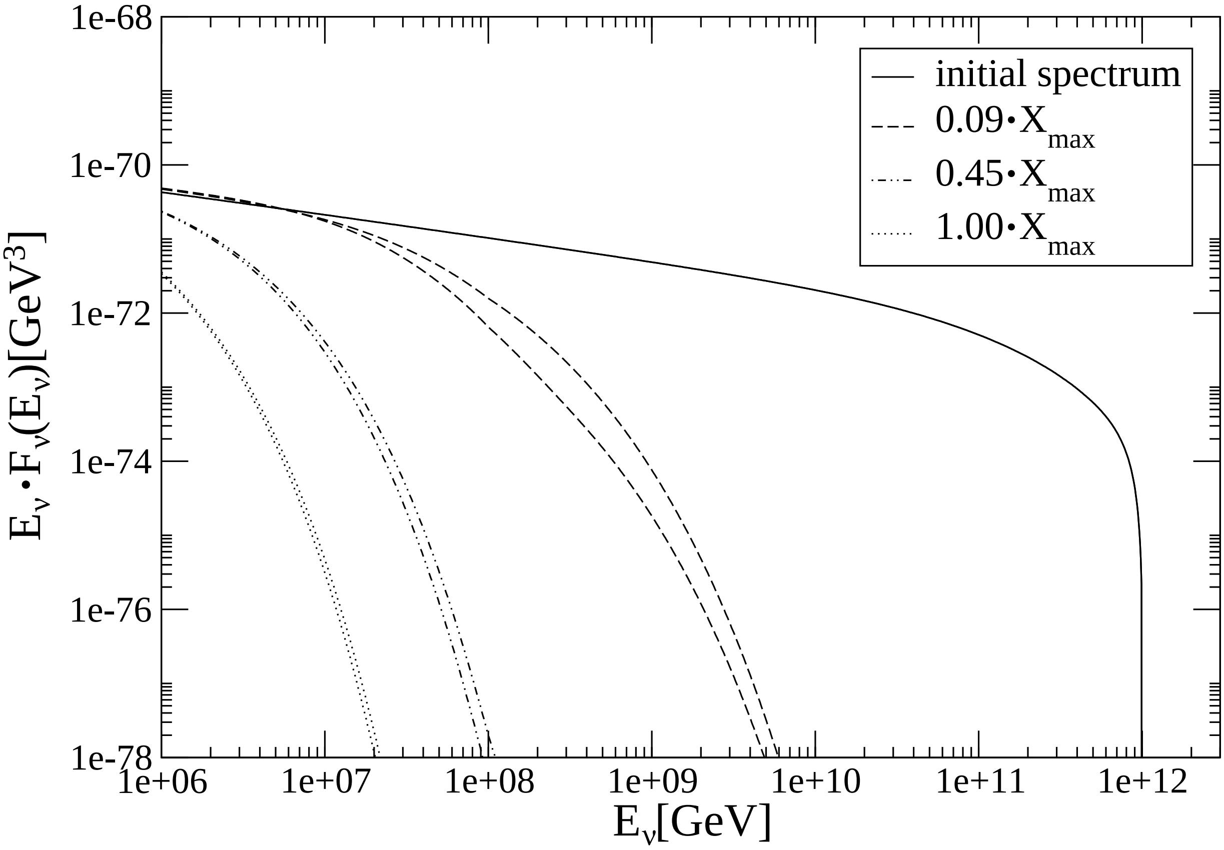

Abbildung 5: Example for the modification of a tau neutrino spectrum due to energy loss. For each pair of curves the upper (lower) curve shows the result without (with) consideration of energy loss. The solid curves show the initial spectrum and the dashed, dot–dashed and dotted curves show the flux after a column depth of of $0.09X_{\max}$, $0.45X_{\max}$ and $X_{\max} = 2.4 \cdot 10^6$ GeV^3.

3.3 Neutralino LSP and Neutrino fluxes

In principle we are now able to solve the transport equations for neutralino LSP and neutrino fluxes. However, since the transport equation is a first order differential equation, we have to specify the boundary conditions $F_{\tilde{\chi}_1^0}(E, 0)$ and $F_{\nu_{\mu,e,\tau}}(E, 0)$, i.e. the initial spectra for the fluxes. For this purpose we use the program SHdecay [11]; it provides us with the complete spectra of all stable particles at the end of shower causing by the decay of a X particle within the framework of the MSSM. Some input parameters of this program are the mass of the X particle as well as its primary decay mode. Neutralinos are produced along with protons, photons, electrons and neutrinos at the location of X decays, so the last remaining piece is to determine the normalization of these fluxes, which we fix through the proton flux at 10^{20} eV. We take this flux to be

$$E^3 F_p(E) = 1.6 \cdot 10^{24} \ \mathrm{eV}^2\mathrm{m}^{-2}\mathrm{s}^{-1}\mathrm{sr}^{-1} \tag{48}$$

at $E = 10^{20}$ eV. This roughly corresponds to the flux observed by the HiReS experiment [19], which is somewhat smaller than that observed by AGASA [18]. Note, however, that we ignore the contribution of photons to the UHE CR flux. This is phenomenologically motivated by the observation that UHE CR events seem to be proton–like, rather than photon–like [20]. Normalizing to the sum of the proton and photon fluxes would obviously reduce the predicted neutralino flux, and hence the event rate; depending on the X decay model, the reduction factor would roughly lie between two and five. On the other hand, we ignore all propagation effects. If most X decays occur at significant distance from our galaxy, which may well be true if X particles are confined to topological defects, both the proton and photon fluxes might be depleted by propagation, while leaving the neutralino (and neutrino) flux essentially unchanged. The presence of significant propagation effects would therefore increase the predicted neutralino flux on Earth.

A few exemplary results for neutralino LSP and neutrino fluxes are given in Fig. 6–9 for a X particle of mass 10^{12} GeV and its primary decay mode into a first generation lepton slepton pair ("$l\tilde{l}$"). Here, $X_{\mathrm{max}} = 2.398 \cdot 10^6$ GeV^3 ($X_{\mathrm{max,Moon}} \approx 2.5 \cdot 10^5$ GeV^3) is the maximal Earth (Moon) column depth, corresponding to neutralinos and/or neutrinos which emerge vertically out of the Earth (Moon). Fig. 6 and 7 show the changes of the spectra for neutralino LSP and tau neutrino, respectively, traversing through the Earth; Fig. 8 shows the result for tau neutrinos traversing through the Moon. Finally, the difference between the transition of the total Moon diameter ($X_{\mathrm{max,Moon}} \approx 2.5 \cdot 10^5$ GeV^3) and 9% of the Earth diameter $0.09 \cdot X_{\mathrm{max,Earth}} \approx 2.2 \cdot 10^5$ GeV^3 for a tau neutrino flux is displayed by Fig. 9.

3.4 Total Flux Conservation

We can take advantage of the fact that $\tilde{\chi}_1^0$–nucleon scattering always produces another $\tilde{\chi}_1^0$ in the final state to check our procedure used to solve the transport equation. Since due to the $\tilde{\chi}_1^0$ regeneration, the total flux,

$$\Phi_{\tilde{\chi}_1^0} = \int_{m_{\tilde{\chi}_1^0}}^{E_{\mathrm{max}}} F_{\tilde{\chi}_1^0}(E, X)\,, \tag{49}$$

must remain constant, independent of the column depth X; here E_{max} is the maximal $\tilde{\chi}_1^0$ energy, beyond which the incident LSP flux vanishes. This is reflected in the fact that integrating the right hand side of Eq.(30) over the energy gives zero, i.e. $d\Phi_{\tilde{\chi}_1^0}/dX = 0$. To see this, one re–writes the double integral over E and y into an integral over E_y and y and uses the definition (29) of the $\tilde{\chi}_1^0$ interaction length. We checked that our numerical solution of the transport equations satisfies this constraint very well, with maximal deviation of less than 0.1% even for the hardest spectrum and largest column depth.

4 Calculation of Event Rates

Since we have now the differential fluxes $F_{\tilde{\chi}_1^0}$ and $F_{\nu_{e,\mu,\tau}}$ as function of the neutralino LSP/neutrino energy E and column depth X, we concentrate our attention in this section to the calculation

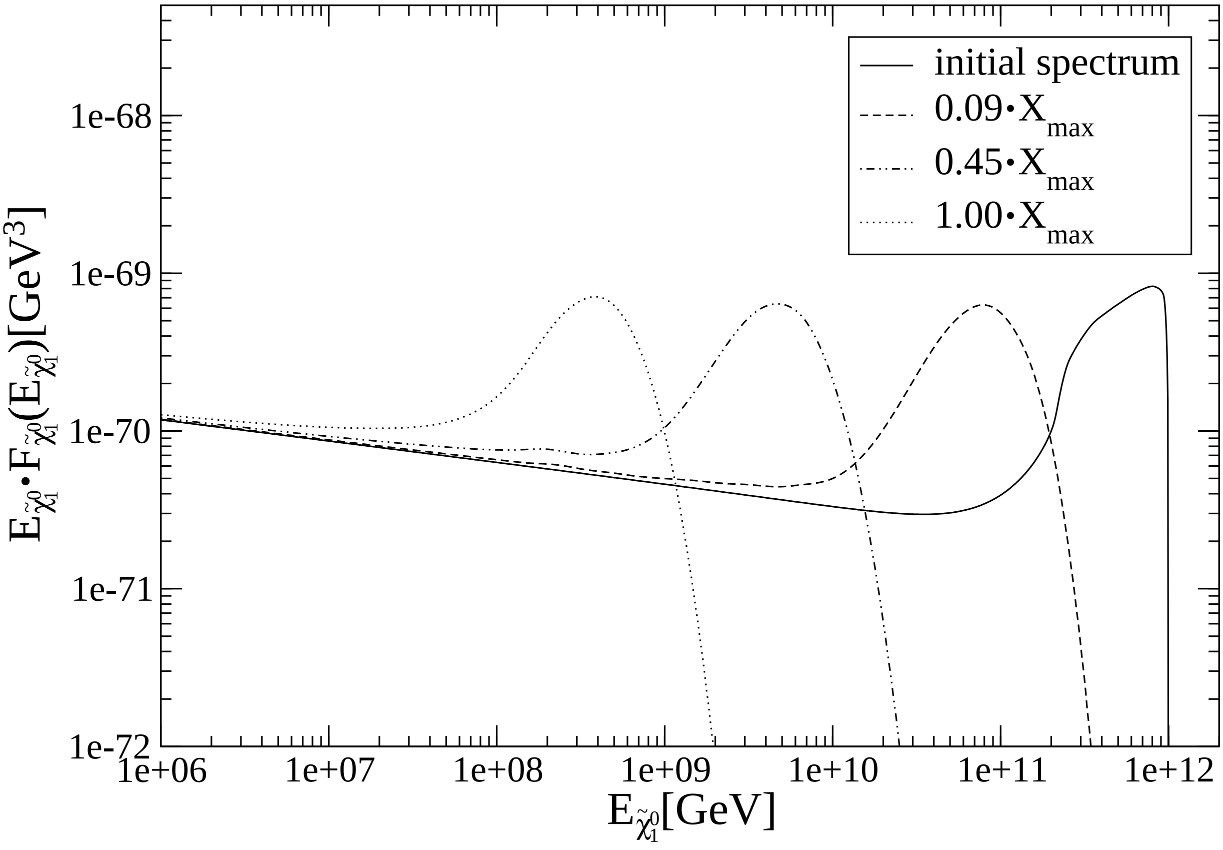

Abbildung 6: Modification of higgsino–like neutralino spectrum from primary $X \to l\tilde{l}$ decays due to propagation through the Earth for scenario H2. The solid curve shows the initial spectrum and the dashed, dot–dashed and dotted curves show the flux after a column depth of of $0.09 \cdot X_{\max}$, $0.45 \cdot X_{\max}$ and $X_{\max} = 2.4 \cdot 10^6$ GeV^3.

of the event rates. The first following subsection gives attention to the usage of the Earth as a detector, the second one of the Moon as a detector.

4.1 Use of the Earth as a Detector

Since we consider scenarios where the total cross section is dominated by either $s-$channel (bino-like LSPs) or $t-$channel (higgsino-like LSPs) contributions, we treat these two contributions in turn for the calculation of the event rates, before discussing the calculation of the neutrino–induced background in the concluding subsubsection of this subsection.

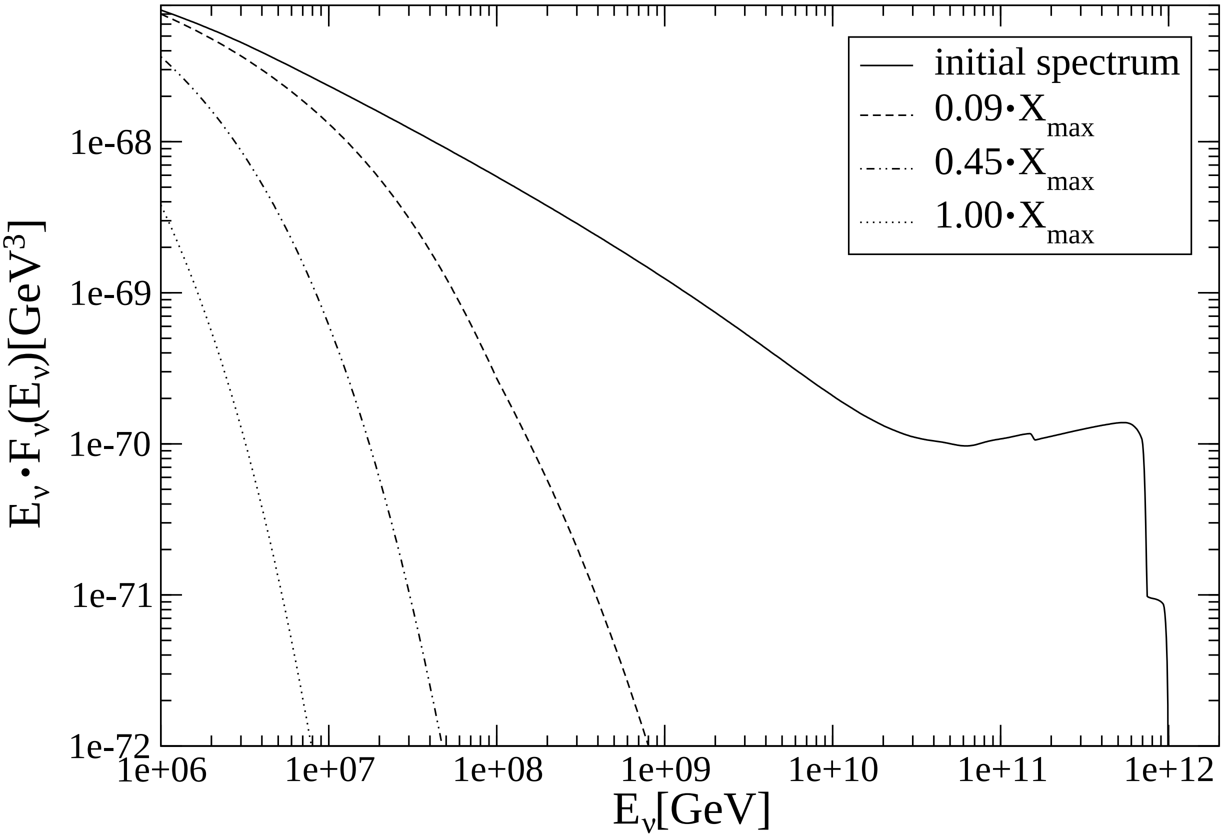

Abbildung 7: Modification of tau neutrino spectrum from primary $X \rightarrow l\tilde{l}$ decays due to propagation through the Earth. The solid curve shows the initial spectrum and the dashed, dot–dashed and dotted curves show the flux after a column depth of of $0.09 \cdot X_{\max}$, $0.45 \cdot X_{\max}$ and $X_{\max} = 2.4 \cdot 10^6$ GeV^3.

4.1.1 Neutralino Signal

As explained in [16, 17, 13], the *s−channel* contribution is dominated by the exchange of on–shell squarks. The event rate is given by:

$$\mathcal{N}_s = \sum_q \int_{E_{\min}}^{E_{\max}} dE_{\mathrm{vis}} \int_{X_{\min}}^{X_{\max}} dX \int_0^{y_{\max\mathrm{q}}} dy \frac{1}{y} F_{\tilde{\chi}_1^0}(\frac{E_{\mathrm{vis}}}{y}, X) \frac{d\sigma_s(\frac{E_{\mathrm{vis}}}{y}, y)}{dy} \mathcal{V}\,. \tag{50}$$

Here, the sum runs about all quark flavors q, and the first integration is over the visible energy $E_{\mathrm{vis}} = E_{\tilde{\chi}^0_{1,\mathrm{in}}} - E_{\tilde{\chi}^0_{1,\mathrm{out}}} = yE_{\tilde{\chi}^0_{1,\mathrm{in}}}$. Eq. (50) is similar to the regeneration part of the corresponding transport equation (30) because both expressions are the answers to similar questions; we want

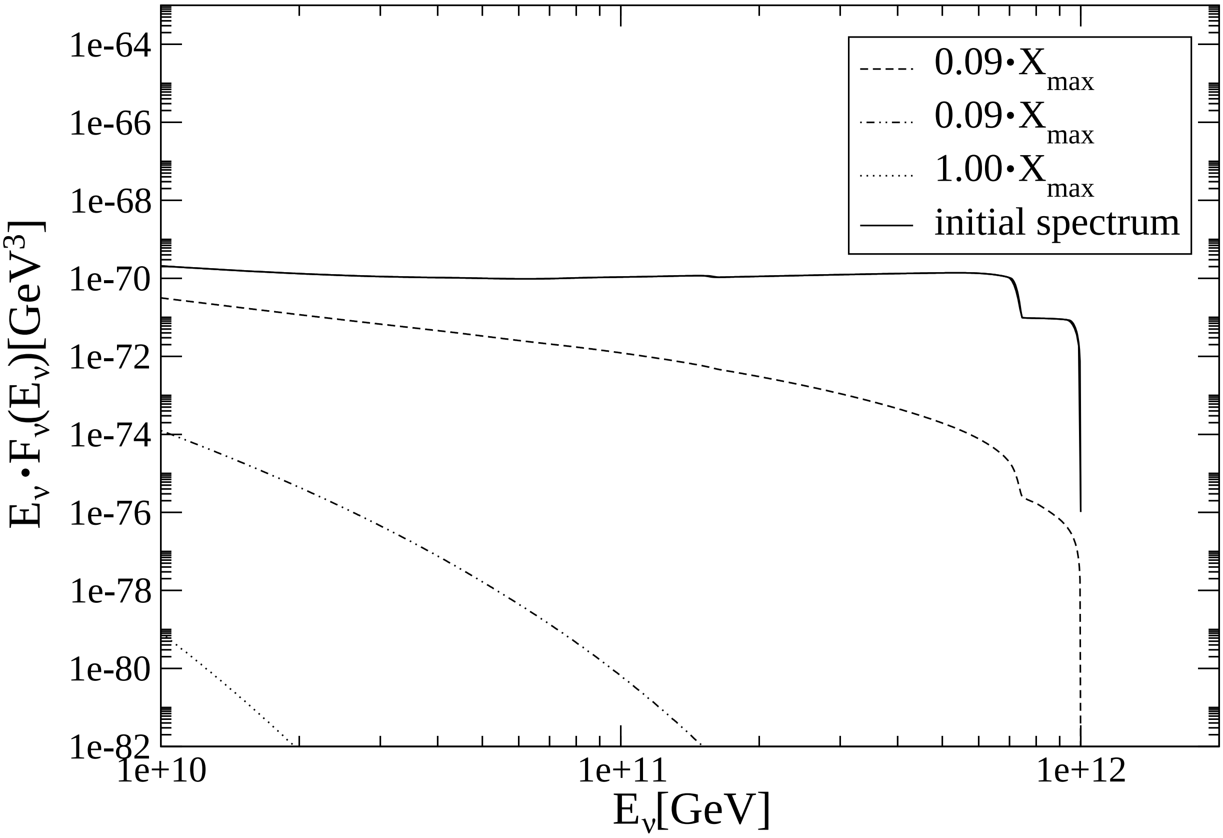

Abbildung 8: Modification of tau neutrino spectrum from primary $X \rightarrow l\tilde{l}$ decays due to propagation through the Moon. The solid curve shows the initial spectrum and the dashed, dot–dashed and dotted curves show the flux after a column depth of of $0.09 \cdot X_{\mathrm{max}}$, $0.45 \cdot X_{\mathrm{max}}$ and $X_{\mathrm{max}} = 2.5 \cdot 10^5$ GeV^3.

to know the number of particles which have a certain amount of energy E and lost a certain amount E_{vis} of their energy, respectively, after their interactions with matter. The differences between the two expression are that one performs two additional integrations about E and X; the reason is that we have a range of possible values for each of this two parameters in case of the event rate calculation and we want to calculate the total event rate, respectively; the factors $1 - y$ are substituted by y since we integrate over the visible, rather than total, energy. The factor $\mathcal{V}$ takes the experimental basic data like detector volume or detection time into account. The lower limit E_{min} on E_{vis} is determined by the energy sensitivity of the experiment, whereas the upper limit E_{max} is determined by kinematics, $E_{\mathrm{max}} \sim M_X/2$; however, after propagation

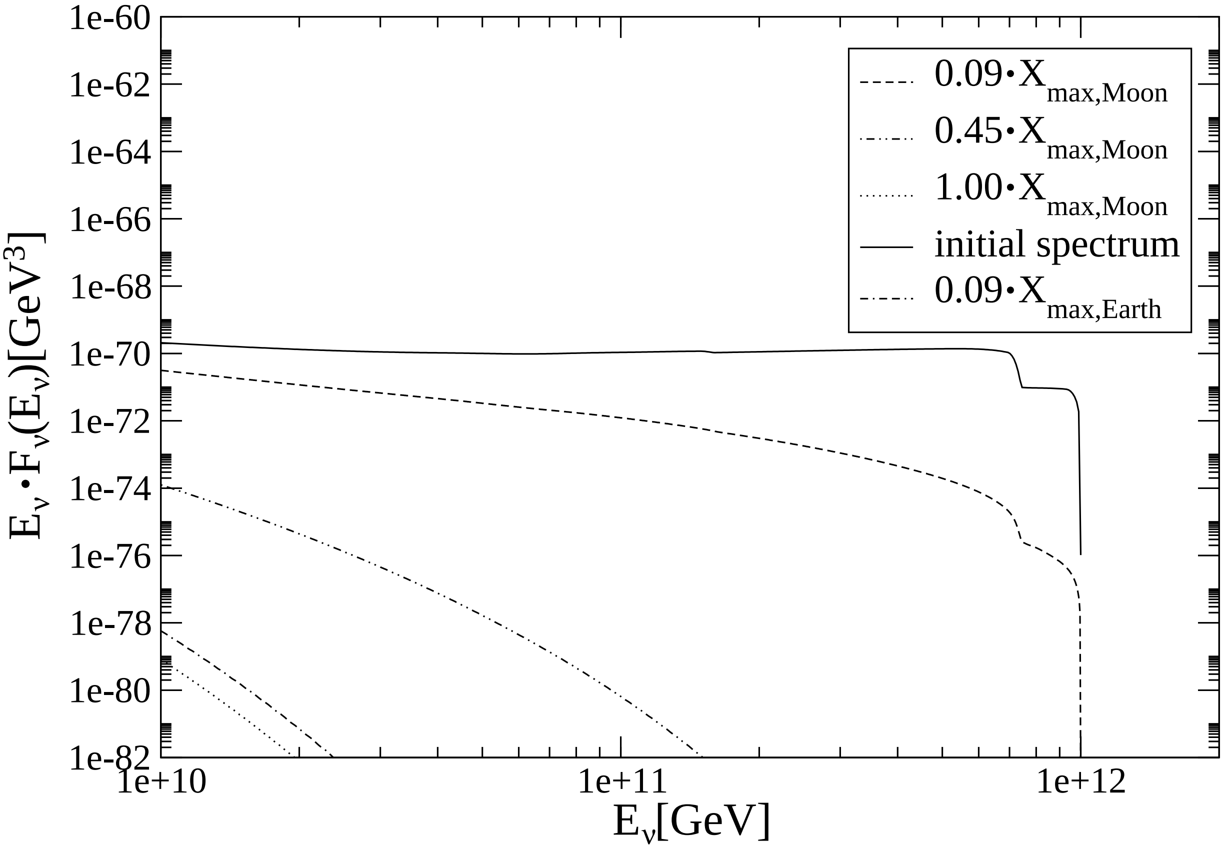

Abbildung 9: Comparison between tau neutrino spectra for Earth and Moon. Conventions are as in Fig. 8 for the neutrino fluxes with the labels *Moon*. The dot–dashed neutrino curve with the label *Earth* shows the change of the initial spectrum for a column depth of $0.09 \cdot X_{\rm max,Earth} = 2.2 \cdot 10^5$ GeV^3

through the Earth the neutralino flux at the highest kinematically allowed energy is very small, see Fig. 6. The lower bound on the column depth, which is given by $X_{\rm min} = 0.13 \cdot 10^6$ GeV^3, corresponds to an angular cut of about 5% on the signal, i.e. we only count events that emerge at least five degrees below the horizon; this cut reduces the neutrino background. The kinematic maximum of the scaling variable y, for 2–body decays $\tilde{q} \rightarrow q + \tilde{\chi}_1^0$, is $y_{\rm max_q} = 1 - m^2_{\tilde{\chi}_1^0}/m^2_{\tilde{q}}$. Since the maximal neutralino energy is finite, there should strictly speaking also be a non–vanishing lower bound on y; note that we need the neutralino flux at $E_{\tilde{\chi}_1^0} = E_{\rm vis}/y$. Finally, the constant factor $\mathcal{V}$ is given by

$$\mathcal{V} \equiv 2\pi V_{\rm eff} \epsilon_{\rm DC} t N_A \rho_w J_D \, . \tag{51}$$

Here, V_{eff} is the water equivalent (w.e.) effective volume, ϵ_{DC} is the duty cycle (the fraction of time where the experiment can observe events), t is the observation time, $N_A = 6.022 \times 10^{23}$ g^{-1} is Avogadro's number, $\rho_w = 10^6$ gm^{-3} is the density of water, and $J_D = \mid d\cos\theta/dX \mid$ is the Jacobian for the transformation $\cos\theta \to X(\cos\theta)$.

Since the $t-$*channel* exchange diagrams predominantly lead to the production of heavier neutralinos $\tilde\chi_1^\pm$ or charginos $\tilde\chi_1^\pm$, collectively denoted by $\tilde\chi_{\text{out}}$, the visible energy also depends on the $\tilde\chi_{\text{out}}$ decay kinematics. The event rate can be written as:

$$\mathcal{N}_t = \int_{E_{\min}}^{E_{\max}} dE_{\text{vis}} \int_{X_{\min}}^{X_{\max}} dX \int_0^1 dy \frac{1}{y} F_{\tilde\chi_1^0}(\frac{E_{\text{vis}}}{y}, X) \left(G^{\text{NC}}_{\tilde\chi_1^0}(E_{\text{vis}}, y) + G^{\text{CC}}_{\tilde\chi_1^0}(E_{\text{vis}}, y) \right) \mathcal{V}\,. \tag{52}$$

Again, Eq. (52) is, in some respects, the counterpart, taking into account the above mentioned differences, to the two regeneration terms of the $t-$channel transport equation (34). The convolutions of Eq. (52) are given by

$$G^{NC,CC}_{\tilde\chi_1^0}(E_{\text{vis}}, y) = \int_z^{z_{1,\max}} \frac{dz_1}{z_1} \frac{d\sigma^{NC,CC}_{t_{\tilde\chi}}(\frac{E_{\text{vis}}}{y}, z_1)}{dz_1} \frac{1}{\Gamma} \frac{d\Gamma_{\tilde\chi_{\text{out}}}(z_1 \frac{E_{\text{vis}}}{y}, z_2 = \frac{z}{z_1})}{dz_2} \theta(z - z_{\min}) \theta(z_{\max} - z) \Bigg|_{z=1-y} . \tag{53}$$

Apart from the substitution $E_y \to E_{\text{vis}}/y$, the $G^{NC,CC}_{\tilde\chi_1^0}$ of Eq.(53) are the integration kernels $K^{NC,CC}_{\tilde\chi_1^0}$ of Eq.(34), multiplied with the total cross section for $t-$channel scattering.

4.1.2 Neutrino Background

The *background* is dominated by ν_τ scattering through $t-$channel exchange of W or Z bosons. At the relevant energies electron and muon neutrinos get absorbed efficiently in the Earth. However, since ν_τ interactions regenerate another ν_τ, albeit at lower energy, τ neutrinos can always traverse the Earth, although their energy may be reduced drastically. Again treating charged and neutral current processes separately, the background rate can be written as

$$\mathcal{N}_{\nu_\tau} = \int_{E_{\min}}^{E_{\max}} dE_{\text{vis}} \int_{X_{\min}}^{X_{\max}} dX \int_0^1 dy \frac{1}{y} F_{\nu_\tau}(\frac{E_{\text{vis}}}{y}, X) \left(\frac{d\sigma^{\text{NC}}_{t_\nu}(\frac{E_{\text{vis}}}{y}, y)}{dy} + N^{\text{CC}}_\nu(E_{\text{vis}}, y) \right) \mathcal{V}\,, \tag{54}$$

where $y = 1 - E_{\nu,\text{in}}/E_{\nu,\text{out}}$. In the case of NC scattering ($Z-$exchange) the entire visible energy results from the hadronic vertex. In case of CC scattering ($W-$exchange) we add the visible energy released in τ decay to that produced at the hadronic vertex and include the tau energy loss in matter:

$$\begin{aligned} N^{CC}_\nu(E_{\text{vis}}, y) \; = \; & \int_z^{z_{1,\max}} \frac{dz_1}{z_1} (1 + \kappa z_1 \frac{E_{\text{vis}}}{y}) \exp(\kappa z_1 \frac{E_{\text{vis}}}{y}) \frac{d\sigma^{CC}_\nu(\frac{E_{\text{vis}}}{y}, z')}{dz'} \\ & \cdot \frac{1}{\Gamma} \frac{d\Gamma(z_1 \frac{E_{\text{vis}}}{y}, z_2 = \frac{z}{z_1})}{dz_2} \theta(z - z_{\min}) \theta(z_{\max} - z) \Bigg|_{z=1-y, z'=z_1 \exp(\kappa z_1 \frac{E_{\text{vis}}}{y})} . \end{aligned} \tag{55}$$

This expression is formally very similar, apart from the changes due the energy loss of the tau, to Eq.(53), which also includes contributions to the visible energy from the decay of an unstable particle. This treatment is conservative since it ignores the fact that a τ produced inside the target volume may decay outside of it. Moreover, if τ production and decay both occur inside the target volume, it may be possible to use this "double bang" signature to remove these background events. On the other hand, we ignore the background from τs produced outside the target which decay inside the observed volume. This contribution should be smaller, since one would need higher neutrino energy to produce a given visible energy in this manner. The τ energy losses in rock or water reduce the energy released in τ decay even further. Recall that after propagation through the Earth the ν_τ flux is a steeply falling function of energy, see Fig. 7.

The background rate (54) is proportional to the tau neutrino flux F_{ν_τ} emerging from the Earth. The ν_τ flux at the location of X decay is usually quite small [11]. However, due to near–maximal neutrino flavor mixing, the three neutrino fluxes impinging on Earth are very nearly equal, i.e. we take one third of the total neutrino flux, normalized according to Eq.(48), as estimate of the incoming ν_τ flux.

4.2 Use of the Moon as a Detector

This subsection concentrates on the derivation of the equations for the calculation of event rates using the Moon as a detector. We make the simplifying assumption that the Moon is a sphere with an average radius r_M of 1737.1 km [98]. The outer layer of the Moon is considered as a suitable medium to observe the Askarayan effect. The reason for this is that the solid rock of the Moon is covered by loose, heterogeneous material up to a height of 10 m [64]. This so–called "regolith" can be modeled as a homogeneous dielectric medium with density $\rho_r = 1.7 \cdot 10^6 \text{ gm}^{-3}$ [63, 64]. We can conclude from this that one has an detector volume of approximately 320 teratons. However, there is an important difference with respect to the calculations of subsection 4.1: An interacting UHE neutralino LSP or neutrino gives rise to Cerenkov light, which is radiated under the Cerenkov light angle θ_C with respect to its former trajectory, cf. Fig. 10; we can only detect this Cerenkov light if its direction of radiation points to the Earth. This restriction leads to a cone of "possible" particle trajectories for every point within the integration volume. Here, "possible" means that the Cerenkov light caused by such a particle can be detected at Earth, cf. Fig. 10. Moreover, we have to assign an individual column depth X_M to every single particle trajectory of the cone.

So the former three dimensional integral of Eq. (54) for the calculation of the neutrino event rates

$$\mathcal{N}_\nu = \int_{E_{\min}}^{E_{\max}} dE_{\text{vis}} \int_{X_{\min}}^{X_{\max}} dX \int_0^1 dy \frac{1}{y} F_\nu(\frac{E_{\text{vis}}}{y}, X)\mathcal{V}\cdots , \tag{56}$$

is substituted by a six dimensional integral

$$\begin{aligned}\mathcal{N}_\nu &= \int_{E_{\min}}^{E_{\max}} dE_{\text{vis}} \int_0^1 dy \int_0^{\pi/2} d\theta' \underbrace{\int_0^{2\pi} d\phi'}_{=2\pi} \int_{r_{M-10m}}^{r_M} dr' r'^2 \sin\theta' \int_0^{2\pi} d\phi \int_{53.5^\circ}^{56.5^\circ} d\theta \sin\theta \\ &\quad \frac{1}{y} F_\nu(\frac{E_{\text{vis}}}{y}, X_M(\theta', \phi', r', \phi, \theta))\mathcal{V}'\cdots \\ &=: \int d\mathcal{M} \frac{1}{y} F_\nu(\frac{E_{\text{vis}}}{y}, X(\theta', \phi', r', \phi, \theta))\mathcal{V}'\cdots , \end{aligned} \tag{57}$$

where $\mathcal{V}$ is now replaced by

$$\mathcal{V}' \equiv \epsilon_{\mathrm{DC_M}} t N_A \rho_M \, . \tag{58}$$

$\int d\mathcal{M}$ is a placeholder for the six integrations.

Above, the primed variables θ', ϕ', r' denote the spherical coordinates for the integration about the volume, c. f. Fig. 10; the unprimed variables ϕ, θ are used for the parametrization of the cone of all "possible" particle trajectories , c. f. Fig. 11. We integrate θ' from zero to $\pi/2$ since one can see one half of the Moon's surface from Earth and we assume that an experiment for the detection of radio waves can detect one half of the Moon's surface, respectively. θ denotes the angle of incidence (roughly the Cerenkov light angle θ_C, see below) of the UHE particles with respect to the $z-$axis of the spherical coordinates, which is orientated in direction to the Earth; ϕ determines the exact position of a trajectory on the circle around the $z-$axis of the cone for a fixed value of θ.

The Cerenkov angle is given by $\cos\theta_C = 1/n$ [64], where n is the index of refraction of the medium. Since the intensity distribution of the radiation is not a sharp peak at the Cerenkov angle $\theta_C \approx 55°$ for regolith [63, 65], the θ integration is carried out for an angle range of 1.5° around θ_C.

The distance r_t which a particle traversed in the Moon's matter between its entrance and interaction point depends on where we are in the integration volume, the angle of incidence θ and finally ϕ. Therefore, the column depth $X_M(\theta', \phi', r', \phi, \theta)$ is now a function of these variables. Moreover, F_ν denotes a neutrino flux; ϵ_{DC_M} is the duty cycle (the fraction of time where the experiment can observe events and the Moon appears above the radio telescope, respectively) and $\rho_M = 3.345 \cdot 10^6$ gm^{-3} is the average density of the Moon [98].

The calculation of the column X_M depth, which is the product of r_t and ρ_M, gives the following result:

$$X_M(\theta', \phi', r', \phi, \theta)) = \sqrt{(\vec{x}' - \vec{r}_p)^2}\rho_M \, , \tag{59}$$

where

$$\begin{aligned}
\vec{x}' &= \vec{r}_p(\theta', \phi', r') + k\vec{e}(\phi, \theta) && (60)\\
k &= -c - \sqrt{r_M^2 - \vec{r}_p^{\,2} + c^2} && (61)\\
c &= \sum_i r_{p_i} e_i && (62)
\end{aligned}$$

$$\begin{aligned}
\vec{e} &= \begin{pmatrix} \cos\phi\sin\theta \\ \sin\phi\sin\theta \\ \cos\theta \end{pmatrix} && (63)\\
\vec{r}_p &= r' \begin{pmatrix} \cos\phi'\sin\theta' \\ \sin\phi'\sin\theta' \\ \cos\theta' \end{pmatrix} \, . && (64)
\end{aligned}$$

Here, $\vec{x}'$ is the position vector between the center of the Moon and the entrance point of the neutrino; $\vec{r}_p$ is the position vector between the center of the Moon and the interaction point of the neutrino; $\vec{e}$ is a unit vector in direction of the particle trajectory which encloses the angle θ with respect to the z-axis of the coordinate system of the cone, see Fig. 11.

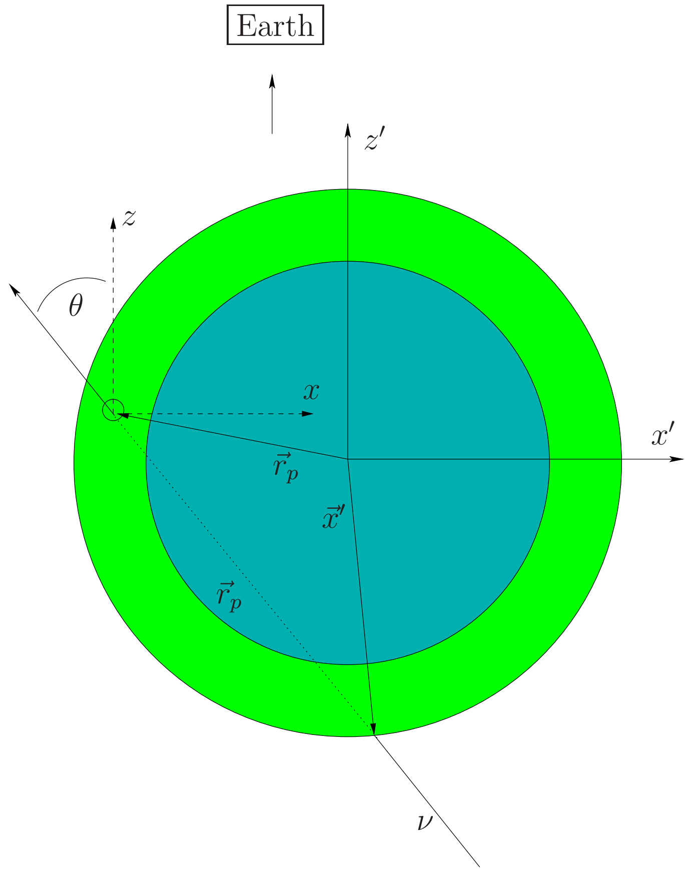

Abbildung 10: Two dimensional cut through the z'-y'-plane of the spherical coordinates. The Earth is located in z-direction. The small circle on the left hand side denotes the interaction point of a UHE particle within the integration volume, which is not plotted true to scale. The parametrization of the angle of incidence of this particle is given with help of the polar angle θ of the unprimed coordinate system.

We only included the tau neutrino flux for the calculation of the event rates in case of the use of the Earth as a detector, cf. subsection 4.1. However, the electron and muon fluxes are not negligible anymore with regard to the event rates for the Moon since here it is possible to have comparatively short covered distances in the Moon's matter. In neutral current interactions there is no difference between the three neutrino fluxes, and the scattered neutrinos keep roughly 80% of their initial energy [64]. However, in case of charged current interactions we have to differ between muon/tau neutrinos and electron neutrinos. All three flavors of neutrinos lose again 20% of their initial energy at the hadronic vertex [64], but in contrast to the produced muon or tau, the resulting electron will initiate an electromagnetic cascade. Indeed, energy

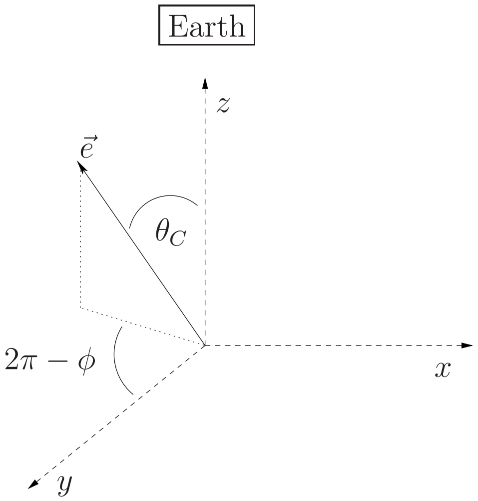

Abbildung 11: Parametrization of the cone of all UHE particles which have the suitable trajectories to radiate Cerenkov light exactly to the direction of the Earth (positive z direction). The unit vector $\vec{e}$ denotes the original direction of incidence for a UHE particle. The Cerenkov light will be emitted in direction of the $z-$axis under an angle which is denoted by θ_C. The angle ϕ describes the orientation of this incident particle with respect to the x-y-plane.

depositions result from the muon and tau due to photonuclear [67] and electromagnetic [66] interactions, but the portions of deposited energy are to small to be detectable. Likewise, the possible decay of the tau is not detectable since it happens for energies $E \leq 10^9$ GeV far away from its creation point [65]. Therefore we only incorporate the energy of the electromagnetic cascade which is initiated by the electron in the calculation of the event rates.

According to this, we make the following modifications of Eq. (54):

$$\mathcal{N}_{\nu_{\mu,\tau}} = \int d\mathcal{M} \frac{1}{y} F_{\nu_{\mu,\tau}}\left(\frac{E_{\text{vis}}}{y}, X(\theta', \phi', r', \phi)\right) \left(\frac{d\sigma^{\text{NC}}_{t_\nu}(\frac{E_{\text{vis}}}{y}, y)}{dy} + \frac{d\sigma^{\text{CC}}_{t_\nu}(\frac{E_{\text{vis}}}{y}, y)}{dy} \right) \mathcal{V}' \,, \tag{65}$$

$$\mathcal{N}_{\nu_e} = \int d\mathcal{M} \frac{1}{y} F_{\nu_e}\left(\frac{E_{\text{vis}}}{y}, X(\theta', \phi', r', \phi)\right) \left(\frac{d\sigma^{\text{NC}}_{t_\nu}(\frac{E_{\text{vis}}}{y}, y)}{dy} + N^{\text{CC}}_{\nu_e}(E_{\text{vis}}, y) \right) \mathcal{V}' \,, \tag{66}$$

where

$$\mathcal{N}^{\text{CC}}_{\nu_e}(E_{\text{vis}}, y) = \delta(y-1)\sigma^{\text{CC}}_{t_\nu}(E_{\text{vis}}) \,, \tag{67}$$

In the following we can use the same Eq. (65) for tau and muon neutrinos as a result of their above mentioned equal properties with respect to the charged current interactions. The sum of the differential cross sections of both kind of interactions inside the bracket of (65) mirrors the fact that the visible energy comes from the hadronic vertex in both cases. There is no change regarding the neutral current interaction part of equation (66) for electron neutrinos; due to the produced electromagnetic cascade we assume that 100% of the electron energy is transformed into detectable Cerenkov light for a charge current interaction. Thus the relevant quantity is the product of the differential flux times the total charged current cross section.

5 Numerical Results

The numerical results for the event rates using the Earth (Moon) as a detector are given in the first (second) subsection of this section.

5.1 Earth

This subsection presents the numerical results for the Earth. Earlier estimates [12, 16] have shown that one will need at least teraton scale targets in order to detect hadronic interactions of neutralino LSPs in top–down models. Therefore we calculate the event rates for future satellite experiments like EUSO [15] or OWL [14] which would be able to monitor enough of the Earth's surface in order to achieve such large targets. This kind of experiment detects the Cerenkov or fluorescence light caused by interactions of very energetic showers in the atmosphere. We get a effective target thickness of 10 to 20 m w.e. for neutralino LSPs when taking into account the atmosphere as well as the first meters of the Earth's surface layer. Then one gets a teraton target for the monitoring of a surface of $\mathcal{O}(10^5)$ km^2; EUSO would be able to detect such a surface area. OWL will even have the possibility to monitor $\mathcal{O}(10^6)$ km^2 simultaneously. One drawback of this approach is that observations of this kind are only feasible on clear, moonless nights, leading to a duty cycle ϵ_{DC} in Eq.(51) of only about 10%. In our numerical results we take a target mass of 10 teratons, $\epsilon_{DC} = 0.1$, and assume an observation time of one year. The result of 1000 Tkg·y can therefore be achieved through one year detection via EUSO (target volume of ≈ 10 teratons) or three years detection via OWL (target volume of ≈ 2.4 teratons).

As shown in [12], the expected neutralino LSP flux depends quite strongly on M_X as well as on the dominant X particle decay mode. Top–down models predict rather hard spectra, i.e. E^3 times the flux increases with energy. Fixing the (proton) flux at $E = 10^{20}$ eV therefore leads to smaller fluxes at $E < 10^{20}$ eV as M_X is increased. Moreover, if M_X is not far from its lower bound of $\sim 10^{12}$ GeV, much of the relevant neutralino flux is produced early in the parton cascade triggered by X decay, which is quite sensitive to the primary X decay mode. In contrast, if $M_X \gg 10^{12}$ GeV, in the relevant energy range most LSPs originate quite late in the cascade; in that case the LSP spectrum is largely determined by the dynamics of the cascade itself, which only depends on Standard Model interactions, and is not very sensitive to the primary X decay mode(s).

Following ref.[12] we therefore study scenarios with $M_X = 10^{12}$ and 10^{16} GeV, for four different primary X decay modes. In contrast to previous analyses [12, 16, 17] we calculate the event rates for both bino–like and higgsino–like neutralino LSPs. As already mentioned and explained in appendix B.1, the former interact with hadronic matter almost exclusively through $s-$channel scattering, while the latter dominantly interact through $t-$channel diagrams.

Finally, we present results for two different values of the minimal visible energy $E_{\rm min}$. Events with visible energy as "low" as 10^6 GeV might be observable via the Cerenkov light emitted by particles in the atmosphere with velocities exceeding the speed of light in air. On the other hand, the fluorescence signal (observed e.g. by the HiReS experiment [19]) can probably only be seen for energies $\gtrsim 10^9$ GeV. In all cases we require the event to come from an angle at least five degrees below the horizon. This reduces the neutrino–induced background, as explained below Eq. (50).

We present results for higgsino– and bino–like neutralino LSPs in Tables 2 and 4, respec-

Event rates for higgsino–like $\tilde{\chi}_1^0$

$E_{\rm vis} \geq 10^6$ GeV, $M_X = 10^{12}$ GeV	$N_{\tilde{\chi}_1^0}$	N_{ν_τ}
$q\bar{q}$	0.19	3.87
$q\tilde{q}$	0.58	7.04
$l\tilde{l}$	7.37	14.17
$5 \times q\tilde{q}$	4.97	45.00
$E_{\rm vis} \geq 10^9$ GeV, $M_X = 10^{12}$ GeV	$N_{\tilde{\chi}_1^0}$	N_{ν_τ}
$q\bar{q}$	0.0089	0.0001
$q\tilde{q}$	0.0608	0.0001
$l\tilde{l}$	2.5121	0.0003
$5 \times q\tilde{q}$	0.2624	0.0006
$E_{\rm vis} \geq 10^6$ GeV, $M_X = 10^{16}$ GeV	$N_{\tilde{\chi}_1^0}$	N_{ν_τ}
$q\bar{q}$	0.0105	0.4448
$q\tilde{q}$	0.0078	0.3079
$l\tilde{l}$	0.0063	0.2917
$5 \times q\tilde{q}$	0.0124	0.4940
$E_{\rm vis} \geq 10^9$ GeV, $M_X = 10^{16}$ GeV	$N_{\tilde{\chi}_1^0}$	N_{ν_τ}
$q\bar{q}$	0.000927	0.000007
$q\tilde{q}$	0.001258	0.000005
$l\tilde{l}$	0.001735	0.000005
$5 \times q\tilde{q}$	0.001807	0.000005

Tabelle 2: Predicted events rates per 10 teratons and year (with duty cycle $\epsilon_{DC} = 0.1$) for the scenario H2 of appendix B.2 where $\tilde{\chi}_1^0$ is higgsino–like, and for the ν_τ induced background. Both signal and background depend on the mass M_X of the progenitor particle, as well as on the primary X decay mode. We show results for X decays into a first generation quark antiquark pair ("$q\bar{q}$"), into a first generation quark squark pair ("$q\tilde{q}$"), into a first generation lepton slepton pair ("$l\tilde{l}$"), and into five quarks and five squarks ("$5 \times q\tilde{q}$"). We only include events that emerge from an angle at least five degrees below the horizon.

tively. We saw in our former work [13] that the cross section for neutralino–nucleon scattering depends only weakly on details of the sparticle spectrum if $\tilde{\chi}_1^0$ is higgsino–like. In Table 2 we therefore only show results for the scenario H2 of appendix B.2 with higgsino–like neutralino LSP. It has an LSP mass of 300 GeV, with the second neutralino $\tilde{\chi}_2^0$ and first chargino $\tilde{\chi}_1^\pm$, which are produced predominantly in NC and CC scattering respectively, having masses of 310 and 303 GeV, respectively; the near–degeneracy of these three states is a consequence of these states all being higgsino–like, which in turn follows if the LSP is a rather pure higgsino state, cf. appendix B.1.

As expected, we find much higher event rates for $M_X = 10^{12}$ GeV than for $M_X = 10^{16}$ GeV. In the former case we also see that the predicted event rate depends significantly on the primary X decay mode, again as expected. The decay into a lepton plus a slepton turns out to

Event rates for higgsino–like $\tilde{\chi}_1^0$		
$E_{\text{vis}} \geq 2 \cdot 10^7$ GeV, $M_X = 10^{12}$ GeV	$N_{\tilde{\chi}_1^0}$	N_{ν_τ}
$q\bar{q}$	0.10	0.18
$q\tilde{q}$	0.35	0.03
$l\tilde{l}$	5.41	0.67
$5 \times q\tilde{q}$	2.78	1.80

Tabelle 3: Predicted events rates per 10 teratons and year (with duty cycle $\epsilon_{DC} = 0.1$) for scenario H2 of appendix B.2, where $\tilde{\chi}_1^0$ is higgsino–like, and for the ν_τ induced background. Lower energy bound E_{vis} was incread to $2 \cdot 10^7$ GeV in comparison to Tab. 2. We show results for X decays into a first generation quark antiquark pair ("$q\bar{q}$"), into a first generation quark squark pair ("$q\tilde{q}$"), into a first generation lepton slepton pair ("$l\tilde{l}$"), and into five quarks and five squarks ("$5 \times q\tilde{q}$"). We only include events that emerge from an angle at least five degrees below the horizon.

be most favorable. The reason is that this decay mode leads to a rather small number of protons produced per X decay, or, put differently, to a large ratio of the LSP and proton fluxes [11]. Since we normalize to the proton flux, this then leads to a rather large LSP flux. This decay mode also leads to the hardest $\tilde{\chi}_1^0$ spectrum. Since the primary X decay only involves weakly interacting (s)particles, parton showering carries away a relatively small fraction of the energy of the original particles. The original slepton will then eventually decay into a very energetic neutralino. As a result, increasing the cut on E_{vis} by three orders of magnitude only reduces the predicted event rate by a factor of ~ 3 in this case.

The second most favorable primary X decay mode is the one into five quarks and five squarks. Since we produce ten strongly interacting (s)particles already in the very first step, each of which initiates an extended QCD shower, the final multiplicity is very large, but the fluxes are relatively soft. One then again needs a rather large normalization factor to reproduce the desired proton flux (48) at $E = 10^{11}$ GeV. Since the $\tilde{\chi}_1^0$ spectrum is quite soft, increasing E_{min} from 10^6 to 10^9 GeV now reduces the predicted signal by a factor of ~ 20.

The worst case is a X particle decay into SM quarks only. This gives a relatively hard proton spectrum. Moreover, superparticles are now only produced in the parton shower. This gives a small ratio of $\tilde{\chi}_1^0$ to proton fluxes, and a relatively soft $\tilde{\chi}_1^0$ spectrum. The fourth primary X decay we considered, into a quark and a squark, also leads to a relatively hard proton flux. However, since a superparticle is produced in the primary X decay, the $\tilde{\chi}_1^0$ flux is larger, and significantly harder, than for $X \to q\bar{q}$ decays.

But the ν_τ induced background of these four cases for $E_{\text{min}} = 10^6$ GeV is $\sim 2 - 20$ times larger than the neutralino LSP signal. Even for the most favorable decay mode the background is still a factor two larger than the signal. One possibility for the reduction of the background is a stronger angular cut because Fig. 12 shows that for $E_{\text{min}} = 10^6$ GeV an enhancement of this cut will not reduce the signal very much. This is in accord with the results of our former work [13], which show large neutralino propagation effects only for LSP energies well beyond 10^7 GeV in this case. Note, however, that typically $E_{\text{vis}} \lesssim 0.1 E_{\tilde{\chi}_1^0,\text{in}}$ for higgsino–like neutralino. A second possibility is the choice of a larger E_{min} because the neutralino LSP fluxes are much harder than the corresponding neutrino fluxes; this can be seen by comparison of the reduction of the event rates for neutralino LSPs and neutrinos when increasing $E_{\min}$ from 10^6 to 10^9 GeV. The latter event rates have a larger reduction of at least two orders of magnitude than the former ones. A comparison between Fig. 7 and Fig. 6 also shows that the neutrino fluxes are much softer than the neutralino LSP fluxes. As a result an increase of $E_{\min}$ from 10^6 to $2 \cdot 10^7$ GeV reduces the neutralino LSP event rates moderately, but the neutrino fluxes are decreased drastically, as shown by Tab. 3. The three most favorable cases have now a background being smaller than the signal. An increase of the angular cut to get the same signal to backround ratio as in Tab. 3 yields a higher reduction of the total size of the event rates than the above explained $E_{\min}$ cut.

We see that at least two of the four cases might lead to observable signals if M_X is near its lower bound, and if visible energies around $2 \cdot 10^7$ GeV can be detected. Of course, at that energy one expects a huge number of ordinary CR induced events, ~ 0.02 events per km^2 and second or (including the duty cycle) $\sim 6 \cdot 10^{10}$ events per year (1 y $\approx 3 \cdot 10^7$ s) in an experiment observing 10^6 km^2, as required for a 10 teraton–scale target mass [44]. One will therefore need an excellent discrimination against such down–going events in order to extract the signal of at best a handful events per year. To that end one may need to sharpen the angular cut somewhat.

On the other hand, only the most favorable scenario remains observable if $E_{\min}$ has to be increased to 10^9 GeV. On the positive side, the ν_τ induced background is now at least two orders of magnitude smaller than the signal, illustrating that the Earth can indeed be used as a filter. This is fortunate, since Fig. 12 shows that now the angular cut can be sharpened only at the cost of a significant reduction of the signal. However, in most cases one would need several tens of Tt·yr to see a convincing signal even for $M_X = 10^{12}$ GeV; for $M_X = 10^{16}$ GeV and $E_{\min} = 10^9$ GeV, one would need several Pt·yr of target mass times observation time! This would require monitoring virtually the entire surface of the Earth. The neutralino LSP flux from decays of such very heavy X particle would remain invisible to teraton scale detectors even for a threshold energy of 10^6 GeV. Note that in this case the predicted event rate is almost independent of the primary X decay mode. The reason is that now the entire relevant energy range satisfies $x \equiv 2E/M_X \ll 1$, where the spectrum is determined almost uniquely by the dynamics of the parton shower [11].

Table 4 shows event rates for bino–like neutralino. In this case the scattering cross section depends strongly on the squark mass [23, 16, 17]. We therefore show results for the three different scenarios of appendix B.2, with first generation squark masses near 370, 580 and 1,000 GeV, respectively. We see that the event rate remains below one event per year and ten teratons in all but one cases. This result seems much less promising than that of earlier studies [12, 16]. However, our rates are actually comparable to those of ref.[16], once the differences in treatment are taken into account. To begin with, we assume that the X particles are distributed like Dark Matter, i.e. clump in our galaxy. Assuming a uniform distribution throughout the Universe, as done in ref.[16], increases the neutralino LSP flux by about one order of magnitude [12]. The reason is that such a uniform distribution suppresses the proton flux due to the GZK effect. One therefore has to increase the normalization in order to match the observed flux. A more or less uniform distribution of X particles could be achieved only if they are bound to topological defects. However, scenarios with such defects, like cosmic strings, are nowadays quite tightly constrained by analyses of cosmic microwave background anisotropies [24]. Moreover, we quote events per year, whereas ref.[16] finds about five events per lifetime of the experiment, taken

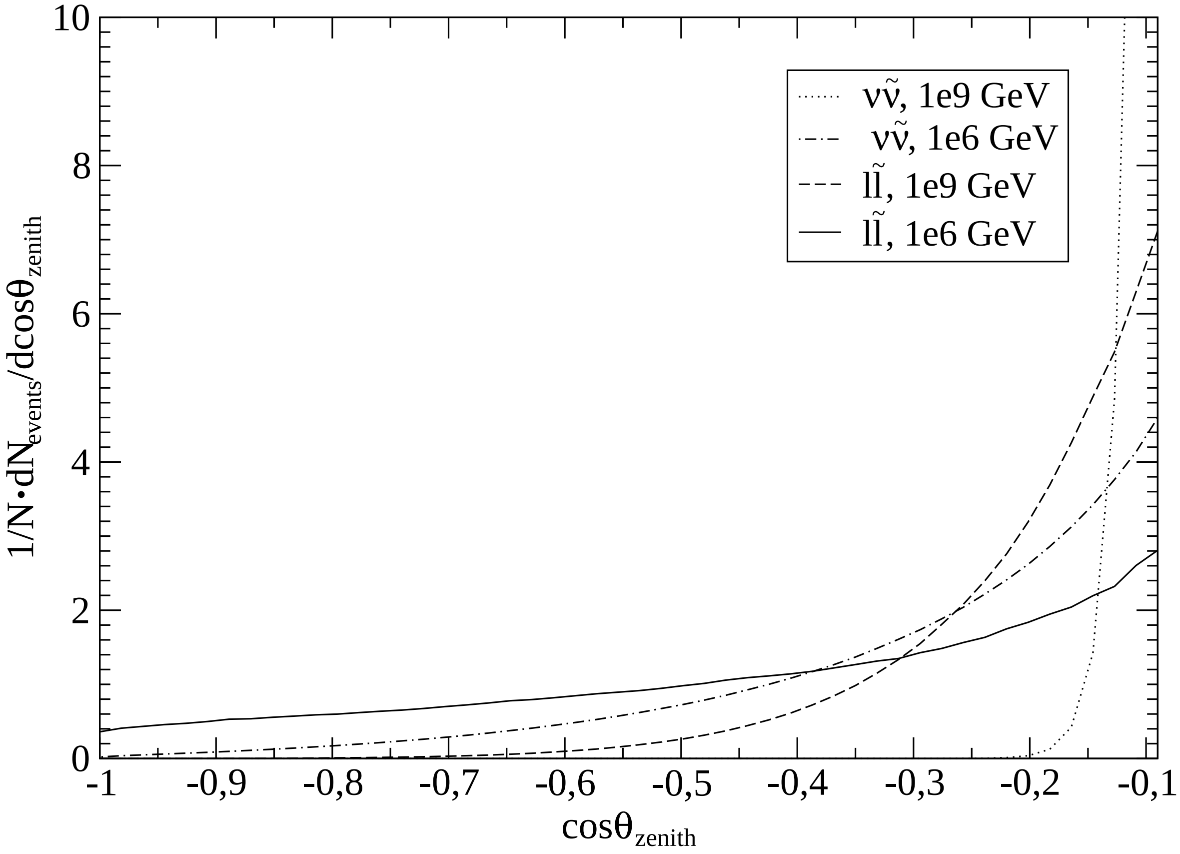

Abbildung 12: Angular dependence of the signal from higgsino–like neutralinos from primary $X \to l\tilde{l}$ decays, and of the ν_τ induced background, for two different values of the lower limit on the visible energy.

to be three years. Finally, ref.[16] applies a cut (of 10^9 GeV) on the total energy of the incident neutralino, whereas our cut is on the visible energy.

We note that for $E_{\rm min} = 10^6$ GeV, the ten body decay mode and $X \to l\tilde{l}$ decays now generally lead to similar event rates. The reason is that very energetic bino–like neutralinos lose energy considerably faster than higgsino–like neutralinos do: for rather light squarks the cross sections are comparable, but the energy loss per scattering is much larger for bino–like states, which produce a squark with $m_{\tilde{q}} \gg m_{\tilde{\chi}_1^0}$, than for higgsino–like states, which produce a heavier neutralino or chargino very close in mass to the LSP. The $5 \times q\tilde{q}$ decay mode has a larger flux of softer neutralinos, which suffers less from propagation effects; for bino–like neutralinos this largely compensates the reduction of the rate due to the fact that the cross section is smaller at smaller LSP energy. However, if $E_{\rm vis} > 10^9$ GeV is required, even the relatively softer LSPs

Event rates for bino–like $\tilde{\chi}_1^0$			
$E_{\rm vis} \geq 10^6$ GeV, $M_X = 10^{12}$ GeV	N_{D1}	N_{D2}	N_{D3}
$q\bar{q}$	0.055	0.039	0.017
$q\tilde{q}$	0.130	0.099	0.051
$l\tilde{l}$	0.805	0.796	0.586
$5 \times q\tilde{q}$	1.294	0.944	0.434
$E_{\rm vis} \geq 10^9$ GeV, $M_X = 10^{12}$ GeV	N_{D1}	N_{D2}	N_{D3}
$q\bar{q}$	0.0005	0.0034	0.0055
$q\tilde{q}$	0.0021	0.0142	0.0234
$l\tilde{l}$	0.0381	0.2551	0.4321
$5 \times q\tilde{q}$	0.0145	0.0992	0.1571
$E_{\rm vis} \geq 10^6$ GeV, $M_X = 10^{16}$ GeV	N_{D1}	N_{D2}	N_{D3}
$q\bar{q}$	0.0026	0.0020	0.0010
$q\tilde{q}$	0.0020	0.0015	0.0007
$l\tilde{l}$	0.0018	0.0018	0.0007
$5 \times q\tilde{q}$	0.0032	0.0024	0.0012
$E_{\rm vis} \geq 10^9$ GeV, $M_X = 10^{16}$ GeV	N_{D1}	N_{D2}	N_{D3}
$q\bar{q}$	0.00004	0.00026	0.00042
$q\tilde{q}$	0.00003	0.00020	0.00031
$l\tilde{l}$	0.00010	0.00056	0.00043
$5 \times q\tilde{q}$	0.00004	0.00030	0.00050

Tabelle 4: Predicted event rates for bino–like LSP, for the same combinations of $E_{\rm min}$, M_X and primary X decay mode as in Table 2. We show results for the three different mSUGRA scenarios of appendix B.2, with first generation squark masses of about 370 GeV (D1), 580 GeV (D2) and 1,000 GeV (D3). The background is essentially the same as in Table 2.

produced from the ten body decay mode will typically scatter several times before reaching the detector. $X \to l\tilde{l}$ decays are then again more favorable, due to its initially much larger flux of very energetic neutralinos.

There is always again a neutralino LSP in the final state in case of $s-$channel scattering as used for the derivation of corresponding transport equation (cf. section 3.1 and appendix A.1); this enhances the event rate compared to the numbers of ref.[16]. In that analysis all neutralinos were discarded that interact even once before reaching the detector. Fig. 13 shows that the regeneration of neutralino LSPs for the final states also leads to a much milder dependence of the final event rate on the cross section, and hence on the squark mass, than found in ref.[16]. Increasing the squark mass reduces the cross section, and hence the event rate for given flux. However, it also reduces the effect of neutralino propagation through the Earth, i.e. it increases the flux. These two effects obviously tend to cancel. As a result the event rate as function of $m_{\tilde{q}}$ shows a rather broad maximum, the location of which depends on the cut on $E_{\rm vis}$. A lower $E_{\rm vis}$ means that softer neutralinos can contribute. Since the cross section increases with neutralino energy, softer neutralinos can tolerate lighter squarks before suffering significant propagation losses. As a result, at smaller E_{min} the maximum rate occurs for smaller squark mass. This effect is less pronounced for primary $X \to l\tilde{l}$ decays, since in this case the incident neutralino spectrum is in any case rather hard, even if no cut on E_{vis} is applied.

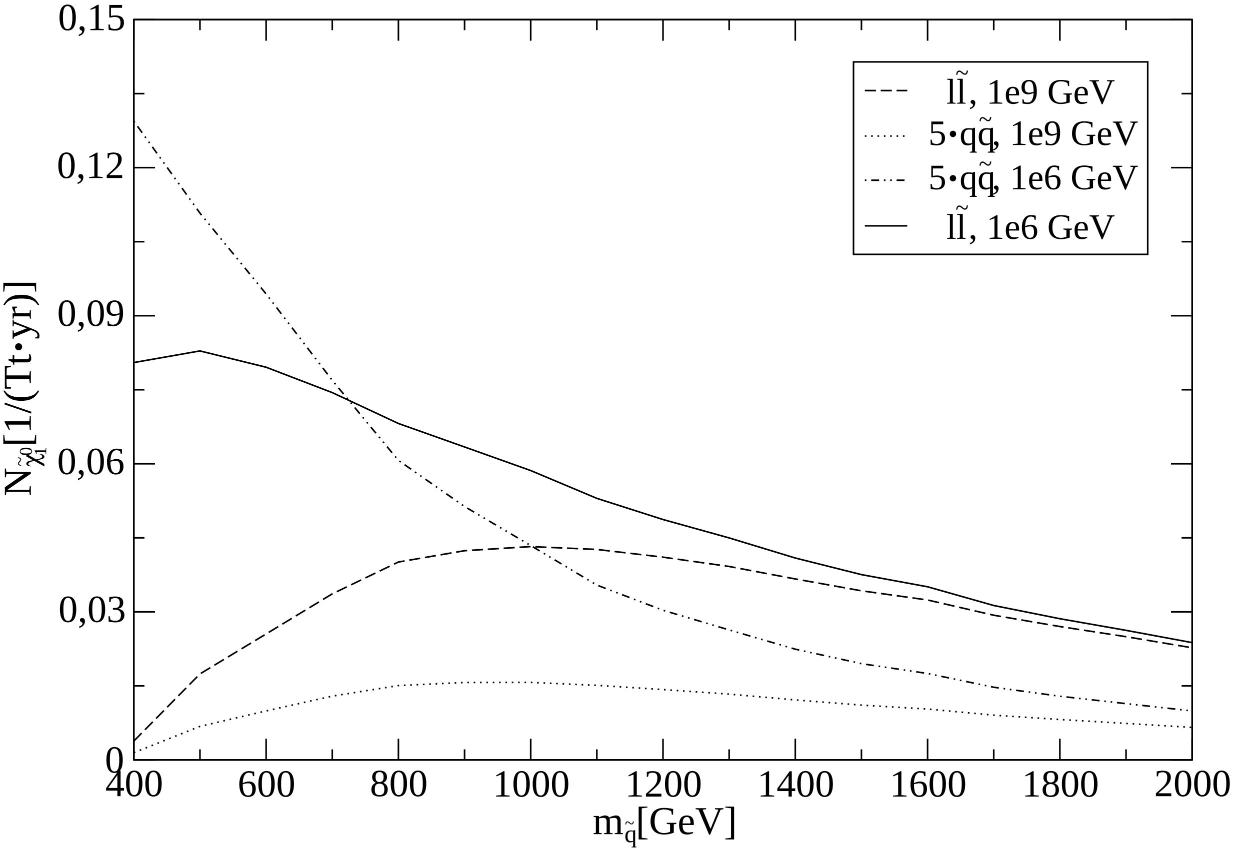

Abbildung 13: Expected event rate due to bino–like neutralino LSPs as a function of the first generation squark mass, for two different primary X decay modes and two choices of the minimal visible energy E_{min}. See the text for further details.

5.2 Moon

This subsection presents the numerical results for the event rates of neutralino LSP and neutrino fluxes using the Moon as a CR detector. We assume that an experiment for the detection of radio waves produced by Cerenkov radiation can cover one half of the Moon's surface. From this we deduce that one has an effective detector volume of about 320 teratons, if the Cerenkov light can leave the regolith up to depth of roughly 10 m. Furthermore, we expect that the Moon appears 40% of the time above the radio telescope and we assume a lower bound for the visible energy of 10^{10} GeV.

We again study the scenarios with $M_X = 10^{12}$ and $M_X = 10^{16}$ GeV for the four different X particle decay modes of the former subsection. The event rates are calculated for all three neutrino flavors and higgsino–like neutralino LSPs without any angle cut. The results are given in Tab. 5.

Event rates for ν and $\tilde{\chi}_1^0$				
$E_{\text{vis}} \geq 10^{10}$ GeV, $M_X = 10^{12}$ GeV	$N^{\nu}_{\mu,\tau}$	N^{ν}_{e}	N^{ν}_{total}	$N_{\tilde{\chi}_1^0}$
$q\bar{q}$	0.38	1.70	2.46	0.10
$q\tilde{q}$	0.72	2.81	4.25	1.10
$l\tilde{l}$	14.76	35.52	65.04	60.10
$5 \times q\tilde{q}$	1.66	7.97	11.29	1.22
$E_{\text{vis}} \geq 10^{10}$ GeV, $M_X = 10^{16}$ GeV	$N^{\nu}_{\mu,\tau}$	N^{ν}_{e}	N^{ν}_{total}	$N_{\tilde{\chi}_1^0}$
$q\bar{q}$	1.97	4.44	8.38	0.04
$q\tilde{q}$	1.27	2.98	5.52	0.05
$l\tilde{l}$	1.46	3.17	6.09	0.19
$5 \times q\tilde{q}$	1.13	2.71	4.97	0.07

Tabelle 5: Predicted event rates per 320 teratons and year (with duty cycle $\epsilon_{DC_m} = 0.4$) for the scenario H2 of appendix B.2 . The first two columns show the event rates for the tau and muon neutrino fluxes, respectively, and the electron neutrino flux. The third column shows the sum of the three neutrino fluxes, whereas the predicted neutralino event rate is given by the fourth column. We show results for X particle decays into a first generation quark antiquark pair ("$q\bar{q}$"), into a first generation quark squark pair ("$q\tilde{q}$"), into a first generation lepton slepton pair ("$l\tilde{l}$"), and into five quarks and five squarks ("$5 \times q\tilde{q}$").

As explained in subsection 4.2 the tau and muon neutrino fluxes have the same equations for the event rates $N^{\nu}_{\mu,\tau}$ due to their equal behaviour regarding the energy loss of their corresponding leptons produced by charged current interactions. Similarly, the different properties of electrons with respect to their energy loss in matter give rise to electron neutrino event rates N^{ν}_{e} being always higher than N^{ν}_{μ}. Remember that it is assumed for the derivation of Eq. (66) that electron neutrinos give 100% of their energy to the visible energy when they undergo a charged current interaction. We take the same initial spectrum for all three flavors of neutrinos since the total neutrino flux impinging on the Earth roughly split up to one third per each flavor due to near–maximal neutrino flavor mixing. In addition, the change of the initial spectra by reason of their interaction with Moon's matter, cf. Fig. 8, is equal for all three neutrino fluxes; the reason is that in our case the regeneration part of Eq. (42) for tau neutrinos gives no contribution because the lower bound for the visible energy is given by 10^{10} GeV; all tau neutrinos for the energy range between 10^{10} and 10^{12} and 10^{16} GeV, respectively, are shifted to a smaller energy than the above lower bound as a result of our ansatz (44) for the energy loss. In summary, we get the same results for the event rates in the case of tau and muon neutrinos and the two event rates $N^{\nu}_{\mu,\tau}$ are always less than the electron event N^{ν}_{e}, cf. first two columns of Tab. 5.

A noticeable result for the neutrino event rates of Tab. 5 is that they nearly always have the same order of magnitude for both $M_X = 10^{12}$ and $M_X = 10^{16}$ GeV; the event rates for $M_X = 10^{16}$ GeV and the first two decay modes are even larger than the corresponding results for $M_X = 10^{12}$ GeV. In comparison, the differences for the results of neutralino LSPs for both X particle masses are quite larger, at least a factor two and two orders of magnitude for the last three decay modes, respectively. The reason for the approximate equality of the neutrino event rates is again the lower bound of 10^{10} GeV for the visible energy, as we will see in the following. Tab. 6 shows the results for the integration of the initial $\tilde{\chi}_1^0$ and ν fluxes for the $l\tilde{l}$ and $5 \times q\tilde{q}$ primary decay modes as a function of the lower energy bound.

integrated fluxes for $\tilde{\chi}_1^0$ and ν

	$\int F_{\tilde{\chi}_1^0} dE$ [GeV^3]		$\int F_\nu dE$ [GeV^3]	
decay, E_{vis} [GeV]	$M_X = 10^{12}$ GeV	$M_X = 10^{16}$ GeV	$M_X = 10^{12}$ GeV	$M_X = 10^{16}$ GeV
$l\tilde{l}$, 10^6	$1.6 \cdot 10^{-69}$	$2.0 \cdot 10^{-72}$	$1.4 \cdot 10^{-67}$	$2.4 \cdot 10^{-69}$
$l\tilde{l}$, 10^9	$1.1 \cdot 10^{-69}$	$9.9 \cdot 10^{-73}$	$1.9 \cdot 10^{-69}$	$2.0 \cdot 10^{-70}$
$l\tilde{l}$, 10^{10}	$9.8 \cdot 10^{-70}$	$6.9 \cdot 10^{-73}$	$5.3 \cdot 10^{-70}$	$5.8 \cdot 10^{-71}$
$5 \times q\tilde{q}$, 10^6	$5.3 \cdot 10^{-69}$	$1.3 \cdot 10^{-71}$	$4.9 \cdot 10^{-67}$	$4.0 \cdot 10^{-69}$
$5 \times q\tilde{q}$, 10^9	$8.5 \cdot 10^{-70}$	$1.9 \cdot 10^{-72}$	$2.8 \cdot 10^{-69}$	$2.1 \cdot 10^{-70}$
$5 \times q\tilde{q}$, 10^{10}	$4.3 \cdot 10^{-70}$	$9.5 \cdot 10^{-73}$	$2.4 \cdot 10^{-70}$	$5.2 \cdot 10^{-71}$

Tabelle 6: Integrated initial fluxes for ν and $\tilde{\chi}_1^0$ of X particle decay into a first generation lepton slepton pair ("$l\tilde{l}$") and into five quarks and five squarks ("$5 \times q\tilde{q}$") for lower E_{vis} bounds of $10^6, 10^9$ and 10^{10} GeV. The first (last) two columns show the results for an upper integration limit of 10^{12} and 10^{16} GeV, respectively, in case of the $\tilde{\chi}_1^0$ (ν) fluxes.

In case of a neutrino flux the results for both X particle masses differ in only one order of magnitude for an lower bound of 10^{10} GeV. By contrast the differences in case of a neutralino LSP flux are always at least two order of magnitudes for all three choices of the lower energy bound. This is reflected in the results for the corresponding event rates as well. Indeed, the exact shape of the initial spectra for all fluxes are different and therefore the resulting spectra for all values of the column depth X are different as well. Nevertheless, the qualitative statement which is based on the results of the integrated fluxes remains; for example, in the case of a lower bound of 10^{10} GeV the integrated neutrino fluxes for both X particle masses in Tab. 6 differs by about a factor of ten for the $l\tilde{l}$ decay mode and a factor of four for the $5 \times q\tilde{q}$ decay mode. In Tab. 5 the difference between the corresponding neutrino event rates is given by roughly a factor ten and two, respectively.

We also see in Tab. 5 that in case of the neutrino fluxes all four decay modes, independent of the X particle mass, might lead to an observable signal. The neutralino LSP fluxes yield only detectable signals for $M_X = 10^{12}$ GeV and the last three decay modes, where the decay into a lepton plus a slepton is again the most favorable one. As explained in the former subsection 5.1 the event rates for the higher X particle mass are quite independent from the primary decay mode, whereas this correlation is still given for the results of the lower X particle mass.

For $M_X = 10^{12}$ GeV and both the second and third decay mode the total event rates might have the same order of magnitude with respect to the neutralino LSP and neutrino fluxes. This gives rise to the question how we can disentangle both signals; this question is again especially important for the discrimination between bottom–up and top–down models. Similarly to the former subsection, we consider the angular dependence of the signals, which is displayed in Fig. 14.

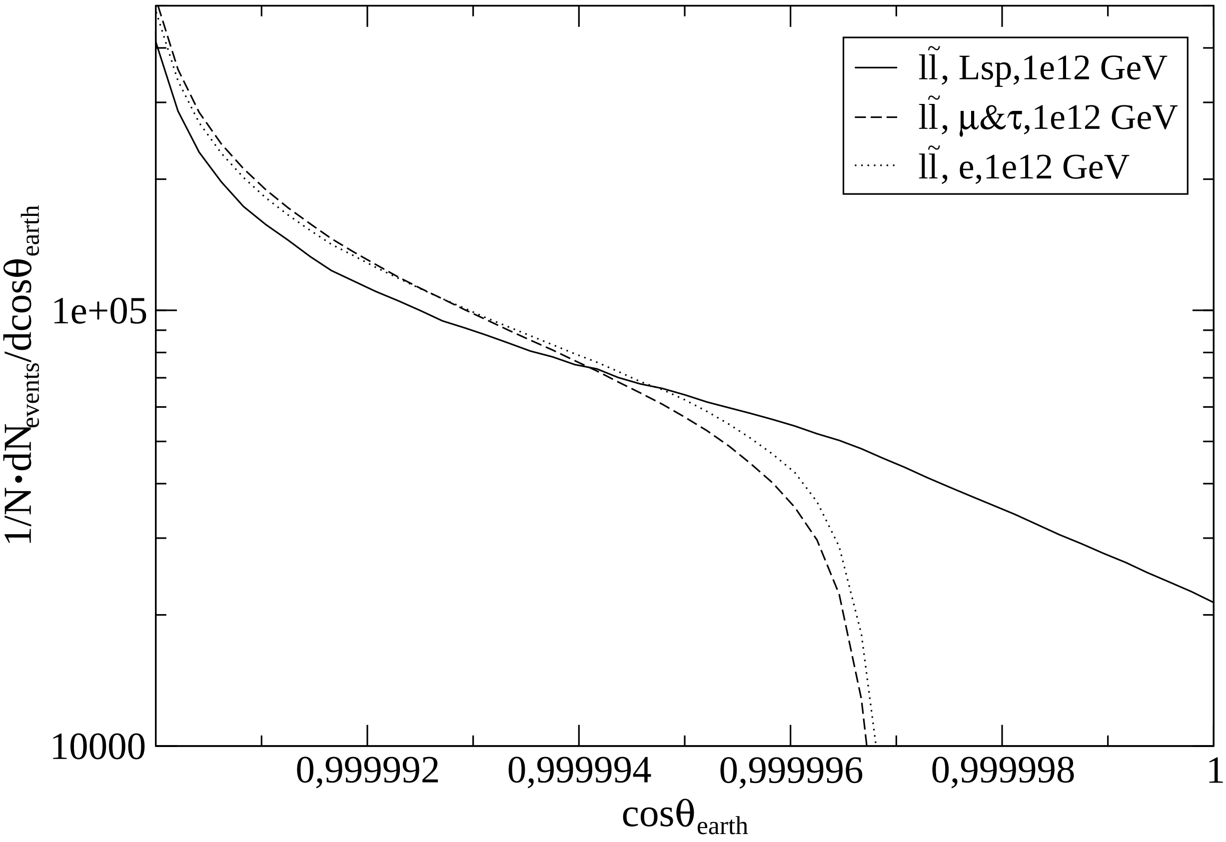

Abbildung 14: Angular dependence of the signals of neutrinos and higgsino–like neutralino LSPs from primary $X \rightarrow l\tilde{l}$ decays. The solid curve shows the differential event rate for the neutralino flux and the dotted and dashed curves show the differential event rate for the electron and tau/muon neutrino flux, respectively.

Here, the normalized differential event rate is plotted against the angle θ_{earth} given by the angle relative to the center of the Moon at Earth which describes the deviation from the connecting line between the Earth's and Moon's center, see Fig. 15. So the larger this angle the larger is the angle θ', cf. Fig. 15, and the distance from the connecting line of Earth–Moon, respectively. However, smaller values of θ' are equal to larger averaged travel distances for the UHE particles in the Moon's matter. Therefore, the attenuation of the neutrino fluxes is higher compared to the neutralino LSP fluxes for such angles. The former fluxes are negligible for $\theta_{earth} \geq 0.999997$ as shown by Fig. 14, what give rise to the requirement of an angle resolution of at least 0.14° for a radio wave antenna experiment if we want to discriminate between signals caused by neutralino LSPs and neutrinos.

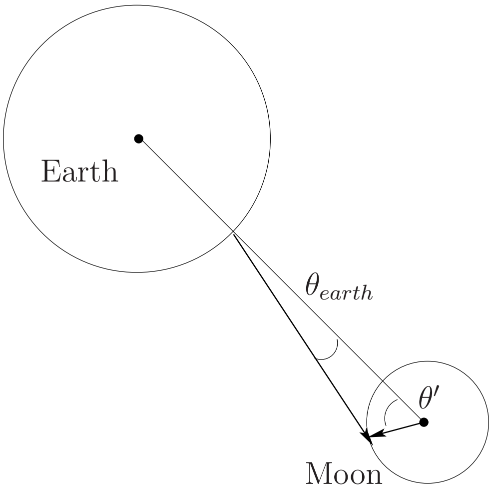

Abbildung 15: The angle θ_{earth} describes the deviation of a straight line from the connecting line Earth–Moon. The relation between the angle θ' of the spherical coordinates of the Moon, cf. Fig. 10, and θ_{earth} is roughly given by $\theta_{earth} = (r_M/d)\sin(\theta')$, where r is the distance between Moon and Earth.

Teil II

Collider Physics

6 Introduction Chapter II

The main part of the first chapter of my PhD thesis deals with the question if it is possible to detect UHE neutralino LSPs with the help of future satellite experiments. A successful verification of the existence of these particles would make the important distinction between bottom–up and top–down models as an explanation for the origin of UHE CRs possible. However, the confirmation of the existence of neutralinos itself would be of equal or even greater importance since it would provide us with a proof and very strong indication, respectively, for Supersymmetry and superparticles. Besides such efforts to find at least the lightest superparticle within the context of astroparticle physics, there are also efforts to detect supersymmetric particles at colliders. But until now it was only possible to derive bounds for masses of superparticles and the parameter space of supersymmetric models with the help of present colliders like the Tevatron at Fermilab [94]. The Tevatron has a center of mass energy of about $\sqrt{s} = 2$ TeV, whereas the LHC will have a initial center of mass energy of 14 TeV, which will allow to test the assumption of the existence of superparticles near the TeV scale. We expect that squark pair production will be one of the most important processes; the reason is that this production process can take place via leading order strong interactions and the corresponding cross section is of $\mathcal{O}(\alpha_s^2)$, where α_s is the strong coupling constant. Furthermore, we have many squark pair production processes, like $ud \to \tilde{u}\tilde{d}$, where the initial states are two valence quarks. As a result, even quite heavy squarks still have a reasonable cross section because the parton distribution functions (pdf's) of valence quarks have the slowest fall–off for large Bjorken$-x$, cf. Fig. 22 of subsection 8.1.

For example, first and second generation squarks with the same mass of $m_{\tilde{q}} \sim 1$TeV still have a leading order (LO) total QCD cross section $\sigma_{\rm LO}$ larger than 0.5 pn, which leads to more than

$$N_{\rm events} = \mathcal{L}\,\sigma_{\rm LO} = 5000 \tag{68}$$

events for a luminosity $\mathcal{L} = 10$ fb^{-1}. A relatively small reduction of the squark masses to 0.85 TeV already yields an increase of the cross section to about 1.7 pb and about 17000 events, respectively. Therefore, it should be possible to measure the production cross section for squark pairs with a statistical uncertainty of only a few percent. However, that means that we need accurate theoretical predictions for this cross section as well. An important step towards the attainment of this aim was the calculation of the next to leading order (NLO) QCD cross section for squark pair production at hadron colliders; it was carried out around 1995 [37], as continuation to the LO cross section calculation in the 1980s [36]. For example, it was shown in [37] that through the inclusion of NLO corrections the dependence on the renormalization/factorization scale of the cross section is strongly reduced. A second result was that the shape of the differential distributions in rapidity and transverse momentum of the final state squarks is hardly changed through these corrections. The remaining uncertainty from yet higher order QCD corrections should be at the ten percent level.

In this second chapter we compute the complete leading order electroweak (EW) contributions to squark pair production at the LHC; the reason is that these contributions can give rise to a change of the pure QCD cross section between a few and more than 50 percent depending on the considered final state squarks and Supersymmetry breaking scenarios. The most important new contributions are caused by the interference of a QCD amplitude with an electroweak amplitude leading to contributions of $\mathcal{O}(\alpha_S \alpha_W)$, where α_W is a weak gauge coupling. On the one hand, the electroweak contributions are marginal if at least one of the final state squarks is a $SU(2)$ singlet; they give rise to an increase of at most 5% in mSUGRA [38] scenarios [39]. On the other hand, the changes are much larger in case of two $SU(2)$ doublet squarks, here the increase can be up to 20% and even exceed 50% for scenarios without gaugino mass unification [40].

These new contributions peak at small transverse momentum of the produced squark, so it is not possible, in contrast to the NLO QCD contributions, to subsume them in a constant "$k-$factor".

The remaining part of this chapter is organized as follows. In the following section 7 we give explicit expressions for our calculation of the squared amplitudes for all processes with two quarks in the initial state and two squarks in the final state, where anti–particles are included. In section 8 we present our numerical results for the total cross section and perform a detailed discussion of these results including the $p_{T,\tilde{q}}$ distribution. The final section 9 is a closing summary and conclusion of the results of this PhD thesis.

7 Formalism

In this second section of chapter two we write down the results of our analytical calculation for the leading–order parton–level squared matrix elements; here, we consider two–to–tow scattering of initial state (anti–)quarks to final state (anti–)squarks. We start with the presentation of a general formula which considers the contributions of general $t-$, $u-$ and $s-$channel diagrams. The different classes of processes then give rise to contributions of these diagrams and the corresponding couplings. These couplings are given in appendix C.

7.1 General Formula

In this first subsection we present the squared matrix elements, which are averaged over the color and the spin. We do not take mixing between $SU(2)$ doublet and singlet squarks and quark mass effects, respectively, into account because we only consider final state squarks of the first two generations; in addition we do not calculate the contributions of gluon fusion. The different kinds of matrix elemtens give rise to the following five functions: Φ (χ) denotes the squared $t-$channel ($u-$channel) diagrams of gaugino exchanges; these first two functions denote the products of two different $t-$ or $u-$channel diagrams as well. Ψ denotes the product of two diagrams for the interference between a $t-$ channel and a $u-$channel diagram. The squared $s-$channel diagrams of gauge boson exchanges (including the product of two different $s-$channel diagrams again) are given by Υ, and Ω denotes the product of the interferences between a $s-$ and a $t-$channel diagram. These five function are given explicitly by:

$$\Phi(\tilde{q}_{i\alpha}, \tilde{q}'_{j\beta}, a) \quad = \quad \frac{1}{4} \sum_{l,k} c_a(l,k) \frac{1}{\hat{t} - m_l^2} \frac{1}{\hat{t} - m_k^2} \Big\{ A(l, k, \tilde{q}_{i\alpha}, \tilde{q}'_{j\beta})$$

$$\begin{aligned}
&\qquad \times(\hat{t}\hat{u} - m^2_{\tilde{q}_{i\alpha}} m^2_{\tilde{q}'_{j\beta}}) + B(l,k,\tilde{q}_{i\alpha},\tilde{q}'_{j\beta}) m_l m_k \hat{s}\Big\}\,, \\
\chi(\tilde{q}_{i\alpha},\tilde{q}'_{j\beta},a) &= \frac{1}{4}\sum_{l,k} c_a(l,k)\frac{1}{\hat{u}-M_l^2}\frac{1}{\hat{u}-M_k^2}\Big\{C(l,k,\tilde{q}_{i\alpha},\tilde{q}'_{j\beta}) \\
&\qquad \times(\hat{t}\hat{u} - m^2_{\tilde{q}_{i\alpha}} m^2_{\tilde{q}'_{j\beta}}) + D(l,k,\tilde{q}_{i\alpha},\tilde{q}'_{j\beta}) M_l M_k \hat{s}\Big\}\,, \\
\Psi(\tilde{q}_{i\alpha},\tilde{q}'_{j\beta},a) &= \frac{1}{4}\sum_{l,k} c_a(l,k)\frac{1}{\hat{t}-m_l^2}\frac{1}{\hat{u}-M_k^2} F(l,k,\tilde{q}_{i\alpha},\tilde{q}'_{j\beta}) m_l M_k \hat{s}\,,
\end{aligned}$$

$$\begin{aligned}
\Upsilon(q_g,q'_h,\tilde{q}_{i\alpha},\tilde{q}'_{j\beta},a) &= \frac{1}{4}\sum_{l,k} c_a(l,k)\frac{1}{\hat{s}-M_l^2}\frac{1}{\hat{s}-M_k^2} G(l,k,q_g,q'_h,\tilde{q}_{i\alpha},\tilde{q}'_{j\beta}) \\
&\quad \times\Big\{(m^2_{\tilde{q}'_{j\beta}} - m^2_{\tilde{q}_{i\alpha}} + \hat{t} - \hat{u})(m^2_{\tilde{q}'_{j\beta}} - m^2_{\tilde{q}_{i\alpha}} + \hat{u} - \hat{t}) \\
&\quad -\hat{s}(2m^2_{\tilde{q}_{i\alpha}} + 2m^2_{\tilde{q}'_{j\beta}} - \hat{s})\Big\}\,, \\
\Omega(q_g,q'_h,\tilde{q}_{i\alpha},\tilde{q}'_{j\beta},a) &= -\frac{1}{4}\sum_{l,k} c_a(l,k)\frac{1}{\hat{s}-M_l^2}\frac{1}{\hat{t}-m_k^2} H(l,k,q_g,q'_h,\tilde{q}_{i\alpha},\tilde{q}'_{j\beta}) \\
&\quad \times\Big\{(m^2_{\tilde{q}'_{j\beta}} - \hat{t})(m^2_{\tilde{q}_{i\alpha}} - m^2_{\tilde{q}'_{j\beta}} + \hat{u} - \hat{t}) \qquad\qquad (69) \\
&\quad -\hat{s}(\hat{s} - 3m^2_{\tilde{q}'_{j\beta}} - m^2_{\tilde{q}_{i\alpha}}) + (m^2_{\tilde{q}'_{j\beta}} - \hat{u})(m^2_{\tilde{q}_{i\alpha}} - m^2_{\tilde{q}'_{j\beta}} + \hat{t} - \hat{u})\Big\}\,.
\end{aligned}$$

$\hat{t}$, $\hat{u}$ and $\hat{s}$ denote the partonic Mandelstam variables. $m_{l,k}$, $M_{l,k}$ and $m_{\tilde{q}_{i\alpha,j\beta}}$ are the masses of the propagating particles and the final states squarks, respectively; we use capital letters for the masses of particles exchanged in the $u-$ or $s-$channel, and lower case letters for masses in $t-$channel propagators. The electrically neutral gauge bosons, all of which can contribute to the same processes, are labeled through the indices $l,k = 1,2,3$ for γ, Z and gluon, respectively; W-boson exchange can only occur in different reactions than the exchange of the neutral gauge bosons. Similarly, the four neutralinos and the gluino, which can contribute to the same process, are labeled by $l,k = 1,2,3,4,5$; alternatively, the two charginos are represented by $l,k = 1,2$. The flavour of the quarks and squarks is given by $q, q' = u, d$. $g,h,i,j = 1,2$ are generation indices. $\alpha,\beta = 1,2$ label $SU(2)$ doublet ($L-$type) and singlet ($R-$type) squarks, respectively. $c_a(l,k)$ are the colour factors for the different contributions, where a labels the various exchange topologies; note that unlike l and k, a is not summed. Finally, the functions A,B,C,D,F,G and H are products of the various coupling constants appearing in the matrix elements for the different processes. Their general structure is given by

$$\begin{aligned}
A(l,k,\tilde{q}_{i\alpha},\tilde{q}'_{j\beta}) &= a(l,\tilde{q}_{i\alpha})a(k,\tilde{q}_{i\alpha})b'(l,\tilde{q}'_{j\beta})b'(k,\tilde{q}'_{j\beta}) \\
&+ b(l,\tilde{q}_{i\alpha})b(k,\tilde{q}_{i\alpha})a'(l,\tilde{q}'_{j\beta})a'(k,\tilde{q}'_{j\beta})\,, \\
B(l,k,\tilde{q}_{i\alpha},\tilde{q}'_{j\beta}) &= a(l,\tilde{q}_{i\alpha})a(k,\tilde{q}_{i\alpha})a'(l,\tilde{q}'_{j\beta})a'(k,\tilde{q}'_{j\beta}) \\
&+ b(l,\tilde{q}_{i\alpha})b(k,\tilde{q}_{i\alpha})b'(l,\tilde{q}'_{j\beta})b'(k,\tilde{q}'_{j\beta})\,, \\
C(l,k,\tilde{q}_{i\alpha},\tilde{q}'_{j\beta}) &= c(l,\tilde{q}_{j\beta})c(k,\tilde{q}_{j\beta})d'(l,\tilde{q}'_{i\alpha})d'(k,\tilde{q}'_{i\alpha}) \\
&+ d(l,\tilde{q}_{j\beta})d(k,\tilde{q}_{j\beta})c'(l,\tilde{q}'_{i\alpha})c'(k,\tilde{q}'_{i\alpha})\,, \\
D(l,k,\tilde{q}_{i\alpha},\tilde{q}'_{j\beta}) &= c(l,\tilde{q}_{j\beta})c(k,\tilde{q}_{j\beta})c'(l,\tilde{q}'_{i\alpha})c'(k,\tilde{q}'_{i\alpha}) \\
&+ d(l,\tilde{q}_{j\beta})d(k,\tilde{q}_{j\beta})d'(l,\tilde{q}'_{i\alpha})d'(k,\tilde{q}'_{i\alpha})\,,
\end{aligned}$$

$$\begin{aligned}
F(l,k,\tilde{q}_{i\alpha},\tilde{q}'_{j\beta}) &= a(l,\tilde{q}_{i\alpha})c(k,\tilde{q}_{j\beta})a'(l,\tilde{q}'_{j\beta})c'(k,\tilde{q}'_{i\alpha}) \\
&+ b(l,\tilde{q}_{i\alpha})d(k,\tilde{q}_{j\beta})b'(l,\tilde{q}'_{j\beta})d'(k,\tilde{q}'_{i\alpha})\,, \\
G(l,k,q_g,q'_h,\tilde{q}_{i\alpha},\tilde{q}'_{j\beta}) &= c(l,\tilde{q}_{i\alpha},\tilde{q}'_{j\beta})c(k,\tilde{q}_{i\alpha},\tilde{q}'_{j\beta}) \\
&\times \{e(l,q_g,q'_h)e(k,q_g,q'_h) + f(l,q_g,q'_h)f(k,q_g,q'_h)\}\,, \\
H(l,k,q_g,q'_h,\tilde{q}_{i\alpha},\tilde{q}'_{j\beta}) &= c(l,\tilde{q}_{i\alpha},\tilde{q}'_{j\beta})\{e(l,q_g,q'_h)b'(k,\tilde{q}'_{j\beta})a(k,\tilde{q}_{i\alpha}) \\
&\qquad + f(l,q_g,q'_h)a'(k,\tilde{q}'_{j\beta})b(k,\tilde{q}_{i\alpha})\}\,. \qquad (70)
\end{aligned}$$

Here l and k again label the exchanged (s)particles. $a\,,b\,,c\,,d\,,a'\,,b'\,,c'$ and d' denote couplings of the relevant gaugino–quark–squark vertices; $a\,,c\,,a'$ and c' denote left–handed couplings, i.e. the corresponding vertex factors are multiplied with the left–chiral projector $P_L = (1-\gamma_5)/2$, while $b\,,d\,,b'$ and d' denote right–handed couplings. Similarly, e and f are left– and right–handed gauge boson–quark–anti-quark couplings, respectively, and c is a gauge boson–squark–anti-squark coupling.

After introducing the five functions, describing the contributions from the various kinds of matrixelements, and the corresponding products of couplings, we specify two classes of processes with four and six subclasses, respectively, in the following. Here each subclass gives rise to its own combination of contributing diagrams, color factors, and couplings; the expressions of the couplings are given explicitly in appendix C.

7.2 $qq' \to \tilde{q}\tilde{q}'$

The first class consists of all processes with two quarks (anti–quarks) in the initial state and two squarks (anti–squarks) in the final state. Since this class does not include mixed states with a particle and a anti–particle, there are no $s-$channel contributions. We assume that there is no CKM mixing[1] for charged currents (quark–squark–chargino couplings only occur within one generation); moreover, we require that the squark–quark–gluino and squark–quark–neutralino couplings are flavor–diagonal. As result of both assumptions there are no flavor changing processes in the first class.

7.2.1 $u_i u_j \to \tilde{u}_{i\alpha}\tilde{u}_{j\beta}$

These processes proceed through the exchange of a neutralino or gluino in the $t-$ or $u-$channel, as shown in Fig. 16.

In the notation of Eq.(70) the squared spin– and color–averaged matrix element is given by

$$\overline{|M|}^2 = \Phi(\tilde{u}_{i\alpha},\tilde{u}_{j\beta},1) + \chi(\tilde{u}_{i\alpha},\tilde{u}_{i\beta},1)\delta_{ij} + \Psi(\tilde{u}_{i\alpha},\tilde{u}_{i\beta},2)\delta_{ij}. \qquad (71)$$

If the final state squarks are identical, a statistics factor of $\frac{1}{2}$ must be included. The colour factors of the $t-$ and the $u-$channel are given by $c_1(l,k)$, while the factors for the interference

---

[1] Cabibbo-Kobayashi-Maskawa mixing; with respect to the SM see, e. g., [101]

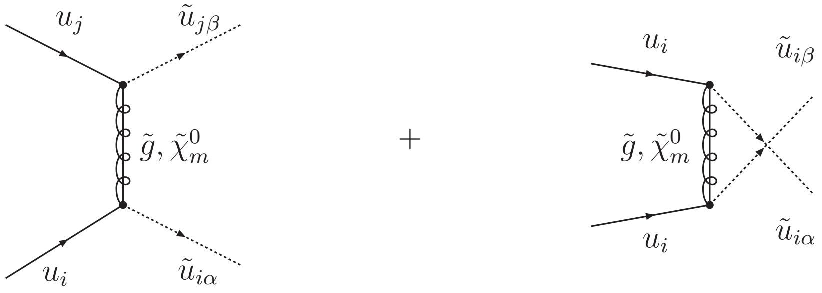

Abbildung 16: Feynman diagrams contributing to $u_i u_j \to \tilde{u}_{i\alpha}\tilde{u}_{j\beta}$. Here i and j are flavor indices, while α and β label the 'chirality' of the squarks, with 1 (2) standing for $L-$type ($R-$type) squarks. The index $m \in \{1,2,3,4\}$ labels the exchanged neutralino. The second, $u-$channel, diagram only exists for $i = j$.

term are given by $c_2(l,k)$. Explicitly,

$$c_1(l,k) = \begin{pmatrix} 1 & 1 & 1 & 1 & 0 \\ 1 & 1 & 1 & 1 & 0 \\ 1 & 1 & 1 & 1 & 0 \\ 1 & 1 & 1 & 1 & 0 \\ 0 & 0 & 0 & 0 & 2/9 \end{pmatrix}, \quad c_2(l,k) = \begin{pmatrix} 1 & 1 & 1 & 1 & 4/9 \\ 1 & 1 & 1 & 1 & 4/9 \\ 1 & 1 & 1 & 1 & 4/9 \\ 1 & 1 & 1 & 1 & 4/9 \\ 4/9 & 4/9 & 4/9 & 4/9 & -2/27 \end{pmatrix}. \tag{72}$$

The relevant neutralino–squark–quark and gluino–squark–quark-couplings to be inserted in Eqs.(70) are

$$\begin{aligned} a(l,\tilde{u}_{i\alpha}) &= a_{\tilde{\chi}^0_l/\tilde{g}}(\tilde{u}_{i\alpha}), & b(l,\tilde{u}_{i\alpha}) &= b_{\tilde{\chi}^0_l/\tilde{g}}(\tilde{u}_{i\alpha}), \\ a'(l,\tilde{u}_{j\beta}) &= a_{\tilde{\chi}^0_l/\tilde{g}}(\tilde{u}_{j\beta}), & b'(l,\tilde{u}_{j\beta}) &= b_{\tilde{\chi}^0_l/\tilde{g}}(\tilde{u}_{j\beta}), \\ c(l,\tilde{u}_{i\beta}) &= a_{\tilde{\chi}^0_l/\tilde{g}}(\tilde{u}_{i\beta}), & d(l,\tilde{u}_{i\beta}) &= b_{\tilde{\chi}^0_l/\tilde{g}}(\tilde{u}_{i\beta}), \\ c'(l,\tilde{u}_{i\alpha}) &= a_{\tilde{\chi}^0_l/\tilde{g}}(\tilde{u}_{i\alpha}), & d'(l,\tilde{u}_{i\alpha}) &= b_{\tilde{\chi}^0_l/\tilde{g}}(\tilde{u}_{i\alpha}). \end{aligned} \tag{73}$$

As indicated earlier, $l \in \{1,2,3,4\}$ refers to the $l-$th neutralino, while $l = 5$ refers to the gluino. Explicit expressions for the neutralino and gluino couplings appearing in Eq.(73) can be found in appendix C, Eqs.(124) and (125).

Eqs.(71) and (72) also hold for the charge conjugate process. However, we have to use the appropriate anti–(s)quark couplings in Eqs.(70), which are given by

$$a_{\tilde{\chi}^0_l/\tilde{g}}(\bar{\tilde{u}}_{i\alpha}) = \left[b_{\tilde{\chi}^0_l/\tilde{g}}(\tilde{u}_{i\alpha})\right]^*, \quad b_{\tilde{\chi}^0_l/\tilde{g}}(\bar{\tilde{u}}_{i\alpha}) = \left[a_{\tilde{\chi}^0_l/\tilde{g}}(\tilde{u}_{i\alpha})\right]^*, \tag{74}$$

where $\bar{\tilde{q}}$ denotes an anti–squark and the stars stand for complex conjugation. Note that even in a CP–conserving scenario some neutralino couplings have to be complex (more exactly, purely imaginary) if we insist on using positive neutralino masses in all propagators [43]. If CP is violated, all chargino, neutralino and gluino couplings may be complex. Finally, recall that a right–handed anti–quark is an $SU(2)$ doublet; its couplings are therefore related to those of left–handed quarks, and vice versa.

7.2.2 $d_i d_j \to \tilde{d}_{i\alpha} \tilde{d}_{j\beta}$

The process $d_i d_j \to \tilde{d}_{i\alpha} \tilde{d}_{j\beta}$ and its charge–conjugated process are given by Eqs.(71) to (74), with the obvious replacement $\tilde{u} \to \tilde{d}$ everywhere.

7.2.3 $u_i d_j \to \tilde{u}_{i\alpha} \tilde{d}_{j\beta}$

This process receives contributions from the $t-$channel exchange of a neutralino or gluino; if both (s)quarks are from the same generation, $i = j$, there is also a $u-$channel chargino exchange contribution. The corresponding Feynman diagrams are shown in Fig. 17.

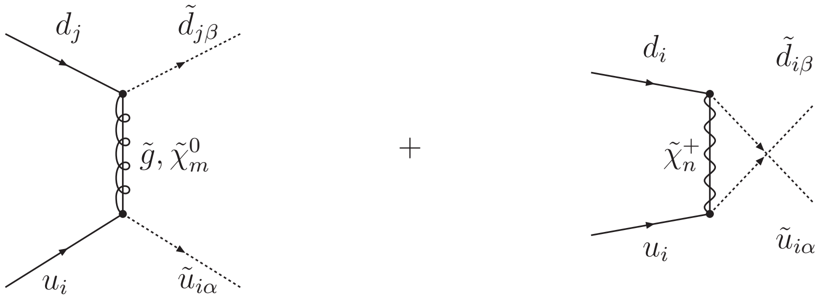

Abbildung 17: Feynman diagrams contributing to $u_i d_j \to \tilde{u}_{i\alpha} \tilde{d}_{j\beta}$. The notation in the $t-$channel diagram is as in Fig. 16. In the second, $u-$channel, diagram, which only exists of $i = j$, the chargino index n runs from 1 to 2.

The squared spin– and color–averaged matrix element is given by

$$\overline{|M|}^2 = \Phi(\tilde{u}_{i\alpha}, \tilde{d}_{j\beta}, 1) + \chi(\tilde{u}_{i\alpha}, \tilde{d}_{i\beta}, 2)\delta_{ij} + \Psi(\tilde{u}_{i\alpha}, \tilde{d}_{i\beta}, 3)\delta_{ij} \,. \tag{75}$$

The color factors for the squared $t-$channel neutralino and gluino contributions, squared $u-$channel chargino contributions and of the interference terms are given by

$$c_1(l,k) = \begin{pmatrix} 1 & 1 & 1 & 1 & 0 \\ 1 & 1 & 1 & 1 & 0 \\ 1 & 1 & 1 & 1 & 0 \\ 1 & 1 & 1 & 1 & 0 \\ 0 & 0 & 0 & 0 & 2/9 \end{pmatrix}, \quad c_2(l,k) = \begin{pmatrix} 1 & 1 \\ 1 & 1 \end{pmatrix}, \quad c_3(l,k) = \begin{pmatrix} 1 & 1 \\ 1 & 1 \\ 1 & 1 \\ 1 & 1 \\ 4/9 & 4/9 \end{pmatrix}. \tag{76}$$

In the squared $t-$channel diagrams the indices l, k labeling the exchanged particles run from 1 to 5 for the four neutralinos and gluino, whereas in the squared $u-$channel chargino–exchange contribution the indices run from 1 to 2. In the interference contribution the index l labeling the particle exchanged in the $t-$channel again runs from 1 to 5, while k takes the values 1 or 2. The couplings to be inserted in Eqs.(70) are given by

$$\begin{array}{rclrcl} a(l,\tilde{u}_{i\alpha}) & = & a_{\tilde{\chi}^0_l/\tilde{g}}(\tilde{u}_{i\alpha}), & b(l,\tilde{u}_{i\alpha}) & = & b_{\tilde{\chi}^0_l/\tilde{g}}(\tilde{u}_{i\alpha})\,, \\ a'(l,\tilde{d}_{j\beta}) & = & a_{\tilde{\chi}^0_l/\tilde{g}}(\tilde{d}_{j\beta}), & b'(l,\tilde{d}_{j\beta}) & = & b_{\tilde{\chi}^0_l/\tilde{g}}(l,\tilde{d}_{j\beta})\,, \\ c(l,\tilde{d}_{i\beta}) & = & a_{\tilde{\chi}^+_l}(\tilde{d}_{i\beta}), & d(l,\tilde{d}_{i\beta}) & = & b_{\tilde{\chi}^+_l}(\tilde{d}_{i\beta})\,, \\ c'(l,\tilde{u}_{i\alpha}) & = & a_{\tilde{\chi}^+_l}(\tilde{u}_{i\alpha}), & d'(l,\tilde{u}_{i\alpha}) & = & b_{\tilde{\chi}^+_l}(\tilde{u}_{i\alpha}) \end{array} \quad . \qquad (77)$$

The explicit expressions for the couplings appearing in Eqs.(77) can be found in Eqs.(124), (125) and (126) in appendix C.

The cross section for the charge–conjugated process can again be obtained by using the appropriate couplings for anti–(s)quarks in Eqs.(70):

$$\begin{array}{rclrcl} a_{\tilde{\chi}^0_l/\tilde{g}/\tilde{\chi}^+_l}(\bar{\tilde{d}}_{i\alpha}) & = & \left[b_{\tilde{\chi}^0_l/\tilde{g}/\tilde{\chi}^+_l}(\tilde{d}_{i\alpha})\right]^*, & b_{\tilde{\chi}^0_l/\tilde{g}/\tilde{\chi}^+_l}(\bar{\tilde{d}}_{i\alpha}) & = & \left[a_{\tilde{\chi}^0_l/\tilde{g}/\tilde{\chi}^+_l}(\tilde{d}_{i\alpha})\right]^*, \\ a_{\tilde{\chi}^0_l/\tilde{g}/\tilde{\chi}^+_l}(\bar{\tilde{u}}_{i\alpha}) & = & \left[b_{\tilde{\chi}^0_l,/\tilde{g}/\tilde{\chi}^+_l}(\tilde{u}_{i\alpha})\right]^*, & b_{\tilde{\chi}^0_l/\tilde{g}/\tilde{\chi}^+_l}(\bar{\tilde{u}}_{i\alpha}) & = & \left[a_{\tilde{\chi}^0_l/\tilde{g}/\tilde{\chi}^+_l}(\tilde{u}_{i\alpha})\right]^* \end{array} \quad . \qquad (78)$$

7.2.4 $u_i d_j \to \tilde{d}_{i\alpha}\tilde{u}_{j\beta}, \quad i \neq j$

This process differs from the one considered in the previous subsection only if the two (s)quarks are from *different* generation, with the $d-$type squark in the final state being from the same generation as the initial $u-$type quark. In this case only the chargino exchange diagram shown in Fig. 18 contributes. We label the momenta such that this is a $t-$channel diagram.

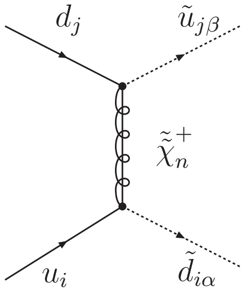

Abbildung 18: Feynman diagram contributing to $u_i d_j \to \tilde{u}_{j\alpha}\tilde{d}_{i\beta}$ with $i \neq j$. The notation is as in the chargino exchange diagram of Fig. 17.

The squared spin– and color–averaged matrix element is given by

$$\overline{|M|}^2 = \Phi(\tilde{d}_{i\alpha}, \tilde{u}_{j\beta}, 1)\,. \tag{79}$$

The colour factor is trivial,

$$c_1 = \begin{pmatrix} 1 & 1 \\ 1 & 1 \end{pmatrix}\,. \tag{80}$$

The couplings to be inserted in Eqs.(70) are,

$$\begin{array}{rclrcl} a(l,\tilde{d}_{i\alpha}) & = & a_{\tilde{\chi}^+_l}(\tilde{d}_{i\alpha})\,, & b(l,\tilde{d}_{i\alpha}) & = & b_{\tilde{\chi}^+_l}(\tilde{d}_{i\alpha})\,, \\ a'(l,\tilde{u}_{j\beta}) & = & a_{\tilde{\chi}^+_l}(\tilde{u}_{j\beta}), & b'(l,\tilde{u}_{j\beta}) & = & b_{\tilde{\chi}^+_l}(\tilde{u}_{j\beta}) \end{array}\,. \tag{81}$$

The cross section for the charge conjugated process can be obtained by using the appropriate anti–(s)quark couplings, which have already been given in Eqs.(78).

7.3 $q\bar{q}' \to \tilde{q}\bar{\tilde{q}}$

The second class contains all processes with one quark and one anti–quark in the initial state as well as one squark and one anti–squark in the final state; thus, in contrast to the first class, there are $s-$channel contributions (both the final state and initial state have vanishing baryon charge).

7.3.1 $u_i\bar{u}_j \to \tilde{u}_{i\alpha}\bar{\tilde{u}}_{j\beta}$

This process receives contributions from the exchange of a gluino or neutralino in the $t-$channel; if $i = j$, there are also $s-$channel gluon, photon and Z exchange contributions. The corresponding Feynman diagrams are shown in Fig. 19.

The squared spin– and color–averaged matrix element is given by

$$\overline{|M|}^2 = \Phi(\tilde{u}_{i\alpha}, \bar{\tilde{u}}_{j\beta}, 1) + \Upsilon(u_i, \bar{u}_i, \tilde{u}_{i\alpha}, \bar{\tilde{u}}_{i\alpha}, 2)\delta_{ij}\delta_{\alpha\beta} + \Omega(u_i, \bar{u}_i, \tilde{u}_{i\alpha}, \bar{\tilde{u}}_{i\alpha}, 3)\delta_{ij}\delta_{\alpha\beta}\,. \tag{82}$$

The color factors of the pure $t-$channel neutralino and gluino contributions, the $s-$channel γ, Z, gluon contributions and the interference terms are given by

$$\begin{array}{rcl} c_1(l,k) & = & \begin{pmatrix} 1 & 1 & 1 & 1 & 0 \\ 1 & 1 & 1 & 1 & 0 \\ 1 & 1 & 1 & 1 & 0 \\ 1 & 1 & 1 & 1 & 0 \\ 0 & 0 & 0 & 0 & 2/9 \end{pmatrix}, \qquad c_2(l,k) = \begin{pmatrix} 1 & 1 & 0 \\ 1 & 1 & 0 \\ 0 & 0 & 2/9 \end{pmatrix}, \\ c_3(l,k) & = & \begin{pmatrix} 1 & 1 & 1 & 1 & 4/9 \\ 1 & 1 & 1 & 1 & 4/9 \\ 4/9 & 4/9 & 4/9 & 4/9 & -2/27 \end{pmatrix}\,. \end{array} \tag{83}$$

The couplings to be inserted in Eqs.(70) are given by:

$$\begin{array}{rclrcl} a(l,\tilde{u}_{i\alpha}) & = & a_{\tilde{\chi}^0_l/\tilde{g}}(\tilde{u}_{i\alpha})\,, & b(l,\tilde{u}_{i\alpha}) & = & b_{\tilde{\chi}^0_l/\tilde{g}}(\tilde{u}_{i\alpha})\,, \\ a'(l,\bar{\tilde{u}}_{j\beta}) & = & \left[b_{\tilde{\chi}^0_l/\tilde{g}}(\tilde{u}_{j\beta})\right]^*\,, & b'(l,\bar{\tilde{u}}_{j\beta}) & = & \left[a_{\tilde{\chi}^0_l/\tilde{g}}(\tilde{u}_{j\beta})\right]^*\,, \\ e(l,u_i,\bar{u}_i) & = & e_{\gamma/Z/g}(u_i,\bar{u}_i)\,, & f(l,u_i,\bar{u}_i) & = & q_{\gamma/Z/g}(u_i,\bar{u}_i)\,, \\ c(l,\tilde{u}_{i\alpha},\bar{\tilde{u}}_{i\alpha}) & = & c_{\gamma/Z/g}(\tilde{u}_{i\alpha},\bar{\tilde{u}}_{i\alpha})\,. & & & \end{array} \tag{84}$$

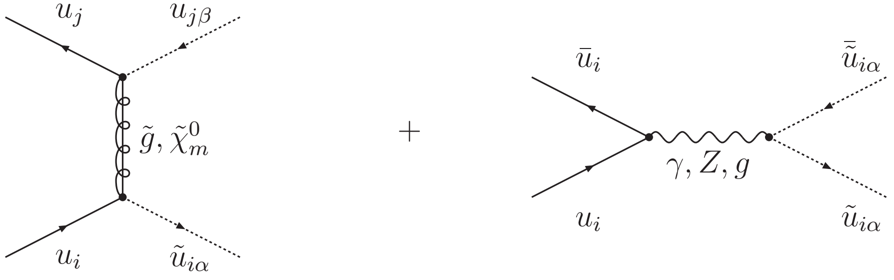

Abbildung 19: Feynman diagrams contributing to $u_i\bar{u}_j \rightarrow \tilde{u}_{i\alpha}\bar{\tilde{u}}_{j\beta}$. The notation for the $t-$channel diagram is as in Fig.16. The gauge boson exchanged in the second, $s-$channel, diagram, which only exists if $i = j$, can be a gluon, a photon or a Z boson.

Recall that in $s-$channel diagrams $l = 1$ stands for a photon, $l = 2$ for a $Z-$boson, and $l = 3$ for a gluon. The explicit expressions for the couplings of these gauge bosons can be found in Eqs.(127) and (128) in appendix C.

7.3.2 $u_i\bar{u}_i \rightarrow \tilde{q}_{j\alpha}\bar{\tilde{q}}_{j\alpha}, \quad i \neq j$

Since the flavor in the initial and final state is different, only the $s-$channel diagrams of Fig.19 contribute. The squared spin– and color–averaged matrix element is thus simply given by

$$\overline{|M|}^2 = \Upsilon(u_i, \bar{u}_i, \tilde{q}_{i\alpha}, \bar{\tilde{q}}_{i\alpha}, 1)\,. \tag{85}$$

The colour factors are

$$c_1(l,k) = \begin{pmatrix} 1 & 1 & 0 \\ 1 & 1 & 0 \\ 0 & 0 & 2/9 \end{pmatrix}\,. \tag{86}$$

The couplings to be inserted in Eqs.(70) can be read off from Eqs.(84).

7.3.3 $u_i\bar{u}_j \rightarrow \tilde{d}_{i\alpha}\bar{\tilde{d}}_{j\beta}$

This process receives contributions from chargino exchange in the $t-$channel; if $i = j$, there are also $s-$channel contributions with gluon, photon and $Z-$exchange. The corresponding Feynman diagrams are shown in Fig. 20.

The squared spin– and color–averaged matrix element is given by

$$\overline{|M|}^2 = \Phi(\tilde{d}_{i\alpha}, \bar{\tilde{d}}_{j\beta}, 1) + \Upsilon(u_i, \bar{u}_i, \tilde{d}_{i\alpha}, \bar{\tilde{d}}_{i\alpha}, 2)\delta_{ij}\delta_{\alpha\beta} + \Omega(u_i, \bar{u}_i, \tilde{d}_{i\alpha}, \bar{\tilde{d}}_{i\alpha}, 3)\delta_{ij}\delta_{\alpha\beta}\,. \tag{87}$$

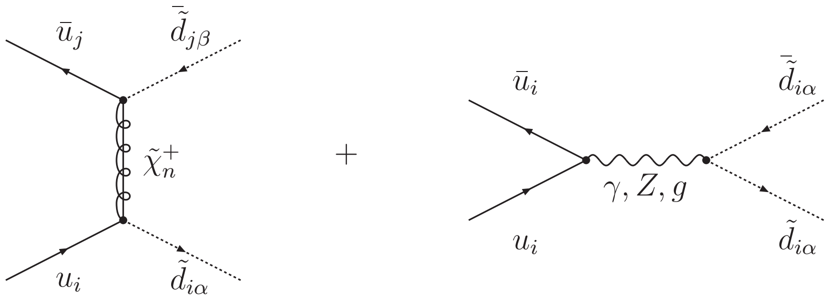

(0,0)

Abbildung 20: Feynman diagrams contributing to $u_i\bar{u}_j \to \tilde{d}_{i\alpha}\bar{\tilde{d}}_{j\beta}$. The notation for the $t-$channel diagram is as in Fig.18. The notation for the second, $s-$channel, diagram, which only exists if $i = j$, is as in Fig. 19.

The respective colour factors for the squared $t-$channel, squared $s-$channel and the interference terms are given by

$$c_1 = \begin{pmatrix} 1 & 1 \\ 1 & 1 \end{pmatrix}, \quad c_2(l,k) = \begin{pmatrix} 1 & 1 & 0 \\ 1 & 1 & 0 \\ 0 & 0 & 2/9 \end{pmatrix}, \quad c_3(l,k) = \begin{pmatrix} 1 & 1 \\ 1 & 1 \\ 4/9 & 4/9 \end{pmatrix}. \tag{88}$$

The couplings to be inserted in Eqs.(70) are given by

$$\begin{aligned}
a(l,\tilde{d}_{i\alpha}) &= a_{\tilde{\chi}^+_l}(\tilde{d}_{i\alpha}), & a'(l,\bar{\tilde{d}}_{j\beta}) &= \left[b_{\chi^+_l}(\tilde{d}_{j\beta})\right]^*, \\
b(l,\tilde{d}_{i\alpha}) &= b_{\tilde{\chi}^+_l}(\tilde{d}_{i\alpha}), & b'(l,\bar{\tilde{d}}_{j\beta}) &= \left[a_{\chi^+_l}(\tilde{d}_{j\beta})\right]^*, \\
e(l,u_i,\bar{u}_i) &= e_{\gamma/Z/g}(u_i,\bar{u}_i), & f(l,u_i,\bar{u}_i) &= q_{\gamma/Z/g}(u_i,\bar{u}_i), \\
c(l,\tilde{d}_{i\alpha},\bar{\tilde{d}}_{i\alpha}) &= c_{\gamma/Z/g}(\tilde{d}_{i\alpha},\tilde{d}_{i\alpha}).
\end{aligned} \tag{89}$$

7.3.4 $d_i\bar{d}_j \to \tilde{q}\bar{\tilde{q}}$

Each of the last three processes has an analogue where all $u-$type (s)quarks are replaced by $d-$type (s)quarks and vice versa. The cross sections for these reactions can be described by simply replacing $u \to d$ and $d \to u$ everywhere.

7.3.5 $d_i\bar{u}_j \to \tilde{d}_{i\alpha}\bar{\tilde{u}}_{j\beta}$

This process receives contributions from the exchange of a gluino or neutralino in the $t-$channel; if $i = j$, there is also an $s-$channel W exchange contribution. The corresponding Feynman diagrams are shown in Fig. 21.

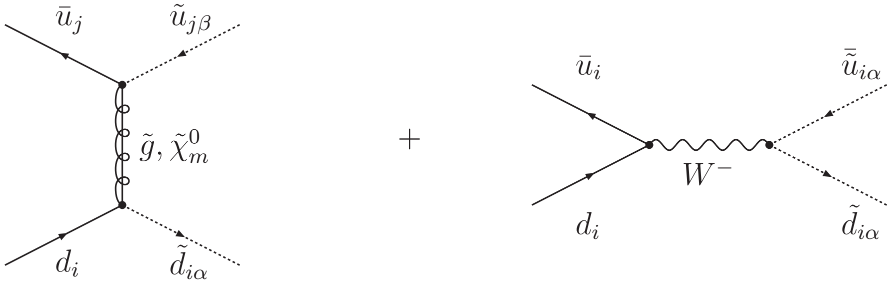

Abbildung 21: Feynman diagrams contributing to $d_i\bar{u}_j \rightarrow \tilde{d}_{i\alpha}\bar{\tilde{u}}_{j\beta}$. The notation for the $t-$channel diagram is as in Fig.18. The second, $s-$channel, diagram, which only exists if $i = j$, proceeds via the exchange of a charged W boson.

The squared spin– and color–averaged matrix element is given by

$$\overline{|M|}^2 = \Phi(\tilde{d}_{i\alpha}, \bar{\tilde{u}}_{j\beta}, 1) + \Upsilon(d_i, \bar{u}_i, \tilde{d}_{i\alpha}, \bar{\tilde{u}}_{i\alpha}, 2)\delta_{ij}\delta_{\alpha\beta} + \Omega(d_i, \bar{u}_i, \tilde{d}_{i\alpha}, \bar{\tilde{u}}_{i\alpha}, 3)\delta_{ij}\delta_{\alpha\beta}\,. \tag{90}$$

The color factors for the pure $t-$channel, pure $s-$channel and interference terms are

$$c_1(l,k) = \begin{pmatrix} 1 & 1 & 1 & 1 & 0 \\ 1 & 1 & 1 & 1 & 0 \\ 1 & 1 & 1 & 1 & 0 \\ 1 & 1 & 1 & 1 & 0 \\ 0 & 0 & 0 & 0 & 2/9 \end{pmatrix}, \quad c_2 = 1\,, \quad c_3 = \begin{pmatrix} 1 & 1 & 1 & 1 & 4/9 \end{pmatrix}. \tag{91}$$

The couplings to be inserted in Eqs.(70) are

$$\begin{array}{rclrcl} a(l,\tilde{d}_{i\alpha}) & = & a_{\tilde{\chi}^0_l/\tilde{g}}(\tilde{d}_{i\alpha})\,, & a'(l,\bar{\tilde{u}}_{j\beta}) & = & \left[b_{\tilde{\chi}^0_l/\tilde{g}}(\tilde{u}_{j\beta})\right]^*, \\ b(l,\tilde{d}_{i\alpha}) & = & b_{\tilde{\chi}^0_l/\tilde{g}}(\tilde{d}_{i\alpha})\,, & b'(l,\bar{\tilde{u}}_{j\beta}) & = & \left[a_{\tilde{\chi}^0_l/\tilde{g}}(\tilde{u}_{j\beta})\right]^*, \\ e(d_i,\bar{u}_i) & = & e_W(d_i,\bar{u}_i)\,, & f(d_i,\bar{u}_i) & = & f_W(l,d_i,\bar{u}_i)\,, \\ c(l,\tilde{d}_{i\alpha},\bar{\tilde{u}}_{i\alpha}) & = & c_W(\tilde{d}_{i\alpha},\bar{\tilde{u}}_{i\alpha}) & & & \end{array} . \tag{92}$$

Explicit expressions for the couplings of the W boson can be found in Eqs.(129) and (130) in appendix C.

Unlike for the processes discussed so far in this subsection, charge conjugation here leads to a physically different reaction. The cross section for this process can be obtained from Eqs.(90)–(92) by replacing (s)quark couplings with anti–(s)quark couplings and vice versa. The new couplings appearing in the $t-$channel diagrams can e.g. be read off from Eqs.(78), whereas the couplings in the $s-$channel diagram remain unchanged.

7.3.6 $d_i\bar{u}_i \to \tilde{d}_{j\alpha}\bar{\tilde{u}}_{j\beta}\,, \quad i \neq j$

This process can only proceed through the exchange of a charged W boson in the $s-$channel. The corresponding Feynman diagram has already been shown in Fig. 21. The squared spin– and color–averaged matrix element is simply given by

$$\overline{|M|}^2 = \Upsilon(d_i, \bar{u}_i, \tilde{d}_{j\alpha}, \bar{\tilde{u}}_{j\beta}, 1)\,. \tag{93}$$

The color factor is trivial, $c_1 = 1$. The couplings to be inserted in Eqs.(70) are

$$\begin{aligned} e(l, d_i, \bar{u}_i) &= e_W(d_i, \bar{u}_i)\,, \qquad f(l, d_i, \bar{u}_i) = f_W(l, d_i, \bar{u}_i)\,, \\ c(l, \tilde{d}_{j\alpha}, \bar{\tilde{u}}_{j\beta}) &= c_W(\tilde{d}_{j\alpha}, \bar{\tilde{u}}_{j\beta})\,. \end{aligned} \tag{94}$$

The squared matrix element for the charge conjugated process is identical.

8 Numerical Results

In this section we present and discuss our results. The first subsection presents the numerical results for the change of the total squark pair production cross section after the addition of electroweak processes and a first rough discussion of these results. The second and third subsections prepare for a further and thorough discussion in the last three subsections of this chapter with respect to the transverse momentum and the mass of the squarks as well as the gaugino masses .

8.1 Parameter Choice and Total Cross Section

We calculated the electroweak contributions to the total squark pair production cross section for pp collisions at the LHC operating at a center of mass energy $\sqrt{s} = 14$ TeV. Results for Tevatron are not be given due to the fact that in most predictive models of supersymmetry breaking [26] the existing bounds [44] on the masses of sleptons and charginos imply that first and second generation squarks are too heavy to be produced here. We do not consider third generation squarks since they are produced dominantly through pure $s-$channel diagrams or gluon fusion without mentionable electroweak contributions to the cross sections of these processes. A distinction of these squarks from first and second generation squarks is possible through the detection of b or t quarks in the final state. Therefore, our results are given for first and second generation squarks, where the mixing between $SU(2)$ singlets and doublets is negligible.

Fig. 7 shows our numerical results for the total squark pair production cross section and the production of two final state $SU(2)$ doublet squarks, respectively, at the LHC.

The change of the cross section because of the electroweak contributions was calculated for six different mSUGRA benchmark scenarios [39]. We do not consider gluon fusion contribution in the initial state because there are no electroweak contributions in leading order and the QCD contribution gets only a subdominant enhancement of 14 (6.7, 1.4)% for SPS 1a (1b, 2). By reason of our leading order calculation in QCD, we use CTEQ5L structure functions [45], cf. Fig. 22 , as well as the one–loop expression for the running QCD coupling α_s, with five active flavors and $\Lambda_{\text{QCD}} = 142$ MeV.

				QCD		QCD + EW		ratio	
Scenario	m_0	$m_{1/2}$	$m_{\tilde{q}}$	Total	LL	Total	LL	Total	LL
SPS 1a	100	250	560	12.11	3.09	12.55	3.50	1.036	1.133
SPS 1b	200	400	865	1.57	0.42	1.66	0.499	1.055	1.186
SPS 2	1450	300	1590	0.0553	0.0132	0.0567	0.0144	1.025	1.091
SPS 3	90	400	845	1.74	0.464	1.83	0.551	1.055	1.188
SPS 4	400	300	760	3.10	0.813	3.22	0.927	1.040	1.141
SPS 5	150	300	670	5.42	1.41	5.66	1.62	1.042	1.152

Tabelle 7: Total cross sections at the LHC for combined first and second generation squark pair production from quark initial states in six mSUGRA benchmark scenarios. It was summed over all squarks and anti–squarks of the first and second generation. All masses are in GeV, m_0 and $m_{1/2}$ being the common soft breaking scalar and gaugino masses, respectively, at the scale of Grand Unification, and $m_{\tilde{q}}$ giving the average mass of first generation $SU(2)$ doublet squarks. All cross sections are in pb. The last two columns show the ratio (QCD + EW) / QCD. We show results for the sum over all squark pairs ("total"), as well as for the sum over all combinations of two $SU(2)$ doublet squarks ("LL"); in both cases we include squarks and anti–squarks. The cross sections have been calculated in leading order, using the CTEQ5L parton distribution functions [45].

The electroweak gauge couplings, as well as the relevant superparticle masses, are taken from the output of the program package SoftSUSY [46]. The couplings are $\overline{\text{MS}}$ couplings at a scale near the squark masses, whereas the squark and gluino masses are on–shell (pole) masses.

Moreover, we take equal factorization and renormalization scales, $\mu_F = \mu_R = m_{\tilde{q}}/2$; this choice leads to quite small next to leading order corrections to the pure QCD contribution [37], see Fig. 23.

Fig. 23 also shows that an increase of these scales reduces the prediction for the pure QCD contribution, whereas a reduction of them increases this prediction. In the former (latter) case the relative importance of the electroweak contributions is enhanced (diminished).

One result of Tab. 7 is that the total squark pair production cross section decreases quickly for higher squark masses. We can give two main reasons for this. First, under the assumptions that the ratios of sparticle masses are kept fixed and the running of α_s is ignored, the partonic cross sections scale like

$$\sigma_{\text{partonic}} \propto \frac{1}{m_{\tilde{q}}^2} \,. \tag{95}$$

Second, increasing squark masses lead to, on average, larger values of Bjorken$-x$ where the parton distribution functions decrease quickly, cf. 22. The total cross section QCD + EW is not changed very much, the increase ranges between 2.5 and 5.5%. So the QCD contributions still dominate after taking the electroweak diagrams into account. Apparently, these diagrams are much more important for processes with two outgoing $SU(2)$ doublet squarks. In this case the increase lies between 9.1 and 18.6%. One reason is that all other combinations of squarks only receive electroweak contributions due to hypercharge interactions, and the squared $SU(2)$ gauge coupling exceeds the squared $U(1)_Y$ coupling by a factor $\cot^2\theta_W \simeq 3.3$.

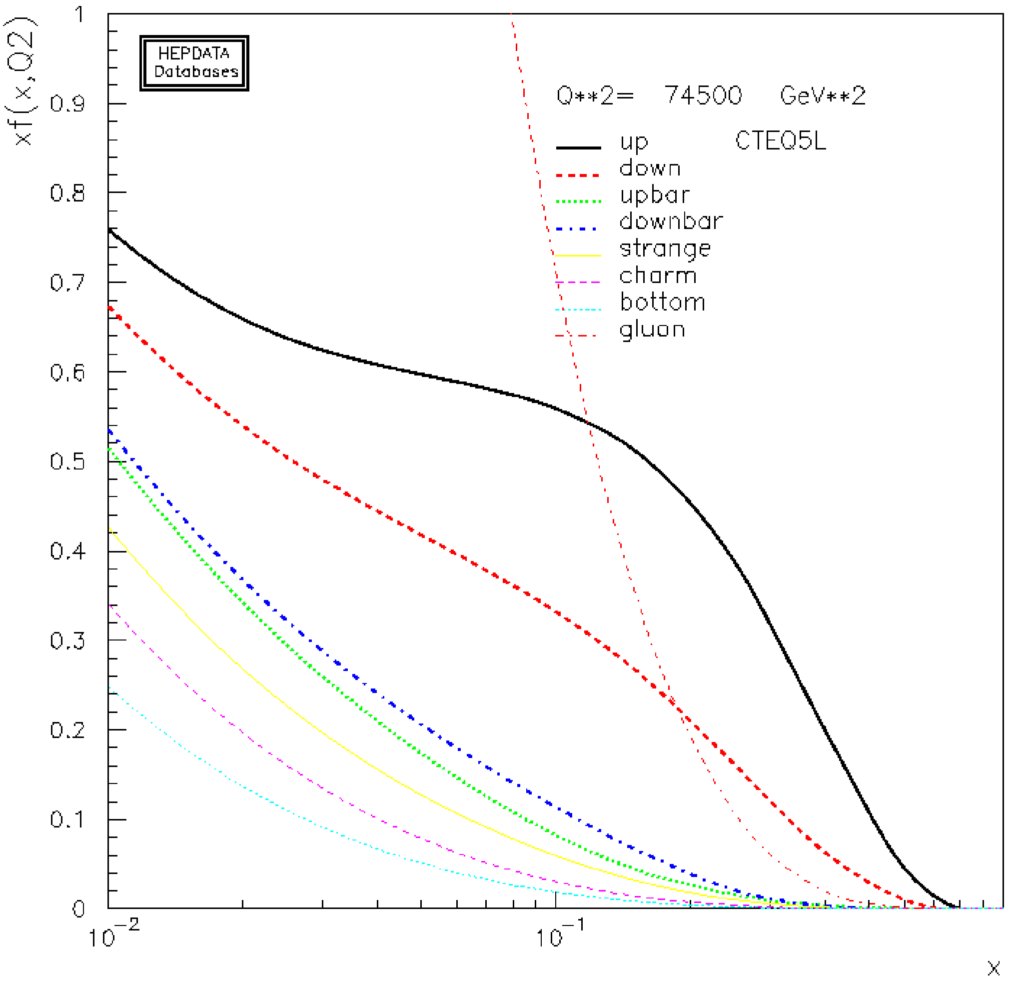

Abbildung 22: CTEQ5L parton distribution functions for five quark flavors and the gluon. The factorization scale Q was chosen as $m_{\tilde{q}}/2$ of the scenario SPS 1a. This figure was generated with help of the Durnham University On–line Plotting and Calculation page [http://durpdg.dur.ac.uk/hepdata/pdf3.html].

Since the electroweak contributions are most important for two $SU(2)$ doublet squarks, all following figures show the ratio of QCD+EW to pure QCD predictions for the production of two $SU(2)$ doublet (anti–)squarks as a function of some selected parameter. For $m_{\tilde{g}} \gtrsim m_{\tilde{q}} > |M_2|, |M_1|$ it should be possible to distinguish between final states with at least one $SU(2)$ singlet squark and two $SU(2)$ doublet squarks. The former one prefers to decay into the neutralino with the largest bino component [49], which is usually the $\tilde{\chi}_1^0$ in mSUGRA; whereas the latter prefer to decay into charginos and neutralinos dominated by $SU(2)$ gaugino components [49], which are typically the $\tilde{\chi}_2^0$ and $\tilde{\chi}_1^\pm$ in mSUGRA. So, $SU(2)$ singlet squarks have shorter decay chains than $SU(2)$ doublet squarks, and the contribution of doublet squarks can be enhanced experimentally by requiring the presence of energetic, isolated charged leptons (electrons or muons), in addition to $\geq$ 2 jets and missing transverse momentum [50]. If $m_{\tilde{g}} < m_{\tilde{q}}$ this distinction becomes more difficult, because in this case most squarks decay into a gluino and

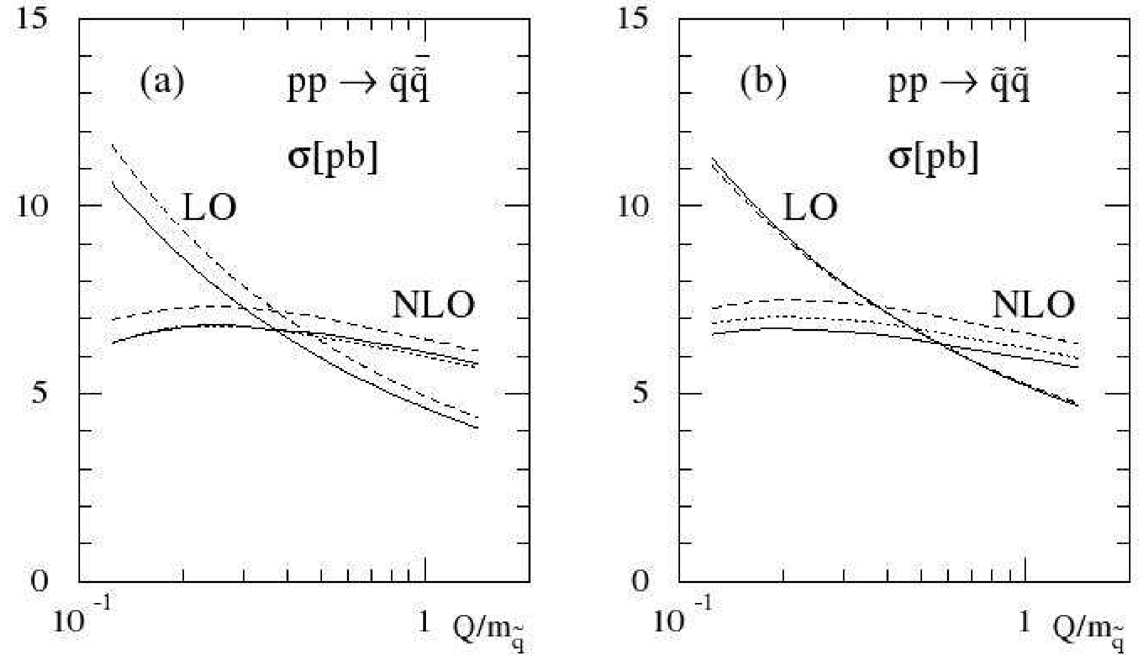

Abbildung 23: The dependence on the factorization/renormalization scale Q of the leading order (LO) and next to leading order (NLO) cross section for anti–squark squark (left hand side) and squark squark (right hand side) production. Squark mass $m_{\tilde{q}}$ is given by 600GeV. This figure was taken from the second reference of [37].

a quark; nevertheless, the branching ratio for $SU(2)$ doublet squark decays into charginos and neutralinos remains sizable even in such a case. Similarly, in models with explicit violation of $R-$parity, $SU(2)$ doublet squarks may have very different decay channels than singlets [51].

8.2 Helicity Flip and Threshold Behaviour

For the following further discussion of our numerical results it is important to distinguish between reactions with two final states squarks with equal ‘chirality’ in the final state, e.g. $\tilde{u}_L\tilde{u}_L$ production, and non–equal ‘chirality’ like $\tilde{u}_L\tilde{u}_R$ production. In the former case both quarks in the initial state have to be left–handed because the quark–squark–gaugino gauge couplings couple $L-$type squarks only to left–handed quarks. Therefore the amplitudes $\mathcal{M}_{HF}$ of these processes are proportional to the mass of the exchanged gaugino $M_{\tilde{V}}$,

$$\mathcal{M}_{HF} \propto M_{\tilde{V}} \, , \tag{96}$$

and the exchanged gaugino has a helicity flip, respectively. Due to the two left–or right–handed quarks in the initial state the total momentum J is equal to zero, see Fig.24, so the final state squarks are in a so–called “$S-$wave” with respect to the partial–wave expansion [105] of this two–to–two process. For this reason, the total cross section is proportional to a single power of the squark center–of–mass [cms] velocity β,

$$\sigma_{\text{total}} \propto \beta\,, \tag{97}$$

which is given by

$$\beta = \sqrt{1 - \frac{4m_{\tilde{q}}^2}{\hat{s}}} \tag{98}$$

for the assumption of equal squark masses $m_{\tilde{q}}$; here, $\sqrt{\hat{s}}$ is the cms energy of the partonic system.

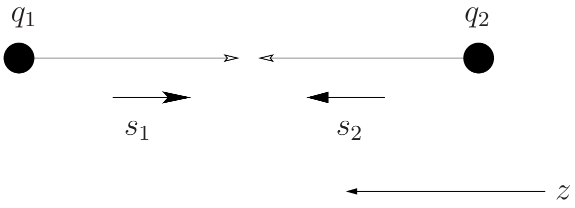

Abbildung 24: Addition of the quark spins to total momentum $J = 0$. The positive z direction of the beams goes from right to left.

In the second case, processes like $\tilde{u}_L\tilde{u}_R$, the initial quarks have opposite helicities, therefore the corresponding amplitudes are not proportional to the mass of the exchanged gaugino and have no helicity flip, respectively. Now the total momentum J is equal to 1 because of the addition of the spins of a left– and right–handed quark, see Fig.25. Thus the total cross section is proportional to the third power of β,

$$\sigma_{\text{total}} \propto \beta^3\,; \tag{99}$$

the produced squarks are in a so–called “p−wave”.

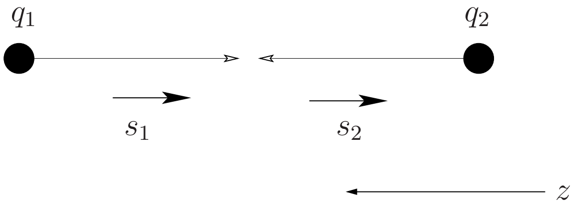

Abbildung 25: Addition of the quark spins to total momentum $J = 1$. The positive z direction of the beams goes from right to left.

8.3 Different Squark Pair Production Processes

The total cross section is a sum of 24 different processes with respect to the initial and final states if we consider only (s)quarks and anti–(s)quarks of the first generation. We divide these processes in three different categories and discuss the important features of each category in the next three subsections. With help of this discussion we make a note regarding the final states involving at least one $SU(2)$ singlet in the last subsubsection of this subsection. The numerical results are for SPS 1a, but we find similar patterns in all other mSUGRA scenarios of Tab. 7.

8.3.1 Category one Processes

The first category consists of seven reactions which show interference between $t-$ and $u-$channel diagrams, where in all but the last case there are both strong and electroweak contributions from both $t-$ and $u-$channel diagrams. The interference terms between QCD and EW diagrams of almost all reactions, except of $dd \to \tilde{d}_L\tilde{d}_R$, have a positive overall sign; therefore the new contributions due to the electroweak processes increase the cross section. All reactions producing two $SU(2)$ doublet squarks, hence the processes with the biggest relative electroweak contributions, require a helicity flip, on that account the threshold behaviour of the cross section is proportional to β. In case of $dd \to \tilde{d}_L\tilde{d}_R$ the interference term is negative but the electroweak contributions are very small because of the size of the involved hypercharges. On this account, we consider in the further discussion all electroweak contributions of this first class as positive; note that all category one processes have two valence quarks in the initial state, therefore all the cross sections are sizable.

A few last remarks regarding the size of the electroweak contributions for some of these first seven processes: despite of two final state $SU(2)$ singlets, the electroweak contribution to the $\tilde{u}_R\tilde{u}_R$ final state is not that small because of the large hypercharges of this state, cf. Tab. 1. The process $ud \to \tilde{u}_L\tilde{d}_L$ has the biggest electroweak contributions because there is an interference between a gluino $t-$channel and a chargino $u-$channel; the equation–blocks (124) and (126) of appendix C shows that, in the limit where one of the charginos is a pure charged wino, the following holds: the coupling of this chargino to a squark and a quark is by a factor $\sqrt{2}$ larger than that of the corresponding neutralino. Therefore one would expect that the electroweak contributions to $\tilde{u}_L\tilde{d}_L$ are about two times more important than those to $\tilde{u}_L\tilde{u}_L$ and $\tilde{d}_L\tilde{d}_L$; however, the results of Tab. 8 show that the enhancement of the latter processes is slightly larger (in comparison to the former process) than expected. The reason is that $\tilde{u}_L\tilde{u}_L$ and $\tilde{d}_L\tilde{d}_L$ have an interference between a $t-$channel QCD and a $u-$channel QCD diagram which is destructive; so the relative importance of the electroweak contributions to these processes is enhanced.

Finally, a listing of the reasons which give rise to the different absolute sizes of the total cross sections for the seven processes of this first category: two identical final state squarks lead to a statistics factor of 1/2 which leads to a suppression of the corresponding five cross sections; however, the remaining two processes $\tilde{u}_L\tilde{u}_R$ and $\tilde{d}_L\tilde{d}_R$ are subject to a suppression as well because their cross sections are proportional to β^3 due to the non–required helicity flip. The cross sections of initial states with two $d-$quarks are smaller than these of initial states with two $u-$quarks; it is caused by the fact that the flux of valence $d-$quarks is very roughly only half of that of valence $u-$quarks. The last reason is that in mSUGRA $SU(2)$ gaugino loop contributions enhance the mass of the $SU(2)$ doublet squarks slightly in comparison to $SU(2)$

		diagrams		helicity	thre–	cross section [pb]		
No.	Process	QCD	EW	flip?	shold	QCD	QCD + EW	ratio
1	$uu \to \tilde{u}_L\tilde{u}_L$	t, u	t, u	yes	β	0.683	0.794	1.162
2	$uu \to \tilde{u}_R\tilde{u}_R$	t, u	t, u	yes	β	0.761	0.796	1.045
3	$uu \to \tilde{u}_L\tilde{u}_R$	t, u	t, u	no	β^3	0.929	0.931	1.002
4	$dd \to \tilde{d}_L\tilde{d}_L$	t, u	t, u	yes	β	0.198	0.232	1.171
5	$dd \to \tilde{d}_R\tilde{d}_R$	t, u	t, u	yes	β	0.234	0.237	1.012
6	$dd \to \tilde{d}_L\tilde{d}_R$	t, u	t, u	no	β^3	0.243	0.243	1.000
7	$ud \to \tilde{u}_L\tilde{d}_L$	t	t, u	yes	β	0.969	1.22	1.261

Tabelle 8: The seven squark pair production processes of category one involving first generation (s)quarks only; charge conjugate reactions are included in the cross section if they differ from the listed ones. The letters s, t, u stand for the existence of $s-$, $t-$ and $u-$channel diagrams, respectively; this is listed separately for strong and electroweak interactions. We also list whether the exchange of a fermion in the $t-$ and/or $u-$channel requires a helicity flip. The fifth column describes the threshold behavior of the cross section, in terms of the squark velocity β in the center–of–mass frame; a behavior $\propto \beta$ (β^3) indicates an $S-$ ($P-$)wave cross section. The values of the cross sections are for scenario SPS 1a (see Table 1). The last column shows the relative size of the electroweak contributions.

singlet squarks; so the pure QCD cross section for the latter ones is a little larger than that for the former ones, cf. Eq.(95).

8.3.2 Category two Processes

The second class allowing interference between $s-$ and $t-$channel diagrams has seven processes again. In the first four cases there are both QCD and electroweak contributions to both the $t-$ and $s-$channel, while in the last three cases only one QCD diagram contributes. The interference between QCD $s-$channel and electroweak $t-$channel diagrams, and that between QCD $t-$channel and electroweak $s-$channel diagrams is *destructive* for all processes of this class because they have a negative overall sign. As a result, nearly all processes have a reduction of the total cross section. The exception are the processes $u\bar{u} \to \tilde{d}_L\bar{\tilde{d}}_L$ and $d\bar{d} \to \tilde{u}_L\bar{\tilde{u}}_L$. These processes only have $s-$channel diagrams for QCD, however, there are $t-$channel diagrams of the chargino exchange. As a consequence of this, the pure QCD, pure electroweak and interference contributions are of roughly equal absolute size; the pure QCD and interference contributions are quite small by reason of the absence of QCD $t-$channel diagrams; the factor $\sqrt{2}$ in each chargino coupling relative to the $SU(2)$ neutralino coupling enhances the pure electroweak $t-$channel contribution. But the absolute change of the total cross section is only marginal due to the strong cancellation between the negative interference and positive, pure electroweak contributions.

Moreover, all processes of the second category have no helicity flip because a $R-$type anti–squark acts like an $L-$type squark, because it couples to a left–handed particle [$\overline{q_R} = (\bar{q})_L$] and a $L-$type anti–squark acts like a $R-$type squark. Therefore the total cross section is proportional to β^3. The total cross sections of these processes are quite small due to the anti–quark in the

		diagrams		helicity	thre–	cross section [pb]		
No.	Process	QCD	EW	flip?	shold	QCD	QCD + EW	ratio
8	$u\bar{u} \to \tilde{u}_L\bar{\tilde{u}}_L$	s, t	s, t	no	β^3	0.165	0.140	0.848
9	$u\bar{u} \to \tilde{u}_R\bar{\tilde{u}}_R$	s, t	s, t	no	β^3	0.187	0.170	0.909
10	$d\bar{d} \to \tilde{d}_L\bar{\tilde{d}}_L$	s, t	s, t	no	β^3	0.0925	0.0784	0.847
11	$d\bar{d} \to \tilde{d}_R\bar{\tilde{d}}_R$	s, t	s, t	no	β^3	0.109	0.106	0.972
12	$u\bar{u} \to \tilde{d}_L\bar{\tilde{d}}_L$	s	s, t	no	β^3	0.0341	0.0353	1.035
13	$d\bar{d} \to \tilde{u}_L\bar{\tilde{u}}_L$	s	s, t	no	β^3	0.0207	0.0219	1.057
14	$u\bar{d} \to \tilde{u}_L\bar{\tilde{d}}_L$	t	s, t	no	β^3	0.178	0.162	0.910

Tabelle 9: The seven squark pair production processes of category two. Labeling as in Tab.8.

initial state which gives rise to a suppression by the corresponding pdf's.

Again, a few last remarks regarding the size of the electroweak contributions for some of the processes of this second category: as expected, the reduction of the cross section is most considerable for $q\bar{q} \to \tilde{q}_L\bar{\tilde{q}}_L$ $(q = u, d)$ because of the two $SU(2)$ doublet squarks. In case of $u\bar{u} \to \tilde{u}_R\bar{\tilde{u}}_R$ the relative size of the reduction of the total cross section is comparable to that of final states with two $SU(2)$ doublet squarks; Tab. 1 shows that the hypercharge of the right–handed u–quark and its superpartner is larger than the factor $1/2$ which the $SU(2)$ neutralino couplings gets from weak isospin. Moreover, since the processes of this second category do not require a helicity flip, the $t-$channel diagrams are not proportional to the mass of the exchanged fermion; therefore the lightest exchanged fermion results in the largest contribution of the $t-$channel propagator. This enhances the electroweak contributions relative to the QCD contributions and the $U(1)$ contribution relative to the contribution because of $SU(2)$ interactions. Finally, the process $u\bar{d} \to \tilde{u}_L\bar{\tilde{d}}_L$ has the smallest relative decrease of the cross section of all final states with two $SU(2)$ doublet squarks; the reason is that this process only has a $t-$channel QCD diagram and no, in contrast to all the other processes of the second category, $s-$channel diagram. This reduces the number of possible interference terms, which lead to negative contributions, but does not give rise to a sizable change of the pure QCD contributions because the $s-$channel diagrams are subdominant.

8.3.3 Category three Processes

For the third class of ten processes, no interference between electroweak and strong contributions is possible; two of these processes only proceed via $s-$channel diagrams, whereas the remaining eight are pure $t-$channel reactions. The electroweak contributions are obviously always positive, but very small. The main reason for this is that all these reactions involve at least one $SU(2)$ singlet in the final state, so that only $U(1)_Y$ interactions give rise to a contribution. On the other hand, the cross sections for the first eight ($t-$channel) processes are sizable; $\tilde{u}_R\tilde{d}_R$ production is even one of the most important channels also for heavy squarks because it can proceed from two valence quarks in the initial state, thus there is no suppression by reason of pdf's. In addition, this production channel allows a $S-$wave in the final state, therefore we have no β^3 suppression due to the threshold factor.

No.	Process	diagrams QCD	EW	helicity flip?	thre–shold	cross section [pb] QCD	QCD + EW	ratio
15	$ud \to \tilde{u}_L\tilde{d}_R$	t	t	no	β^3	0.484	0.485	1.001
16	$ud \to \tilde{u}_R\tilde{d}_L$	t	t	no	β^3	0.477	0.479	1.002
17	$ud \to \tilde{u}_R\tilde{d}_R$	t	t	yes	β	1.113	1.114	1.001
18	$u\bar{u} \to \tilde{u}_L\bar{\tilde{u}}_R$	t	t	yes	β	0.569	0.569	1.000
19	$d\bar{d} \to \tilde{d}_L\bar{\tilde{d}}_R$	t	t	yes	β	0.331	0.331	1.000
20	$u\bar{d} \to \tilde{u}_L\bar{\tilde{d}}_R$	t	t	yes	β	0.491	0.491	1.000
21	$u\bar{d} \to \tilde{u}_R\bar{\tilde{d}}_L$	t	t	yes	β	0.480	0.480	1.000
22	$u\bar{d} \to \tilde{u}_R\bar{\tilde{d}}_R$	t	t	no	β^3	0.202	0.203	1.004
23	$u\bar{u} \to \tilde{d}_R\bar{\tilde{d}}_R$	s	s	–	β^3	0.0420	0.0421	1.002
24	$d\bar{d} \to \tilde{u}_R\bar{\tilde{u}}_R$	s	s	–	β^3	0.0240	0.0240	1.000

Tabelle 10: The ten squark pair production processes of category three. Labeling as in Tab.8.

8.3.4 Final States involving $SU(2)$ Singlet States

The alert reader will have noticed that my explanation for the small size of electroweak contributions to final states involving at least one $SU(2)$ singlet (anti–)squark in subsection 8.1 was not complete; I argued that the squared $SU(2)$ gauge coupling exceeds the squared $U(1)_Y$ coupling by a factor $\cot^2\theta_W \simeq 3.3$, however, a closer look at Tab. 7 shows that this argument is not sufficient: for example, we can infer from the fourth line that in scenario SPS 3, electroweak contributions increase the cross section for the production of two $L-$type squarks by 0.087 pb, whereas they only contribute 0.003 pb to all other squark pair production channels combined. The results of the three last subsubsections enable a complete explanation: the final states of category one with at least one $SU(2)$ singlet squark have a small, positive increase of the cross section due to electroweak contributions. In contrast, the negative electroweak corrections of category two due to hypercharge interactions lead to a (relatively) larger decrease of the cross section; however, the size of the cross sections of the second category is smaller than that of the third category, therefore the total contribution from $U(1)_Y$ interactions is still positive. The larger number of processes which have only very small changes of the cross section due to electroweak contributions (by reason of the absence of interference with QCD diagrams and/or because of the small hypercharge of the involved quarks and squarks) further reduces the relative importance of the contribution from $U(1)_Y$ interactions.

8.4 Dependence on p_T

With help of the above collected features of the three categories, we can carry on with the discussion about the numerical results of Tab. 7. Fig. 26 displays the ratio of the tree–level differential cross section with and without electroweak contributions as a function of the transverse momentum p_T of the produced squarks. As already mentioned in subsection 8.1, we concentrate on final states with two $SU(2)$ doublet (anti–)squarks, where the electroweak contributions are largest. Except for the SPS 2 scenario all curves show a steep increase for small values of p_T.

Moreover, the electroweak contributions even decrease the differential cross section in three cases for large values of p_T. These observations can be understood from the interplay of several effects.

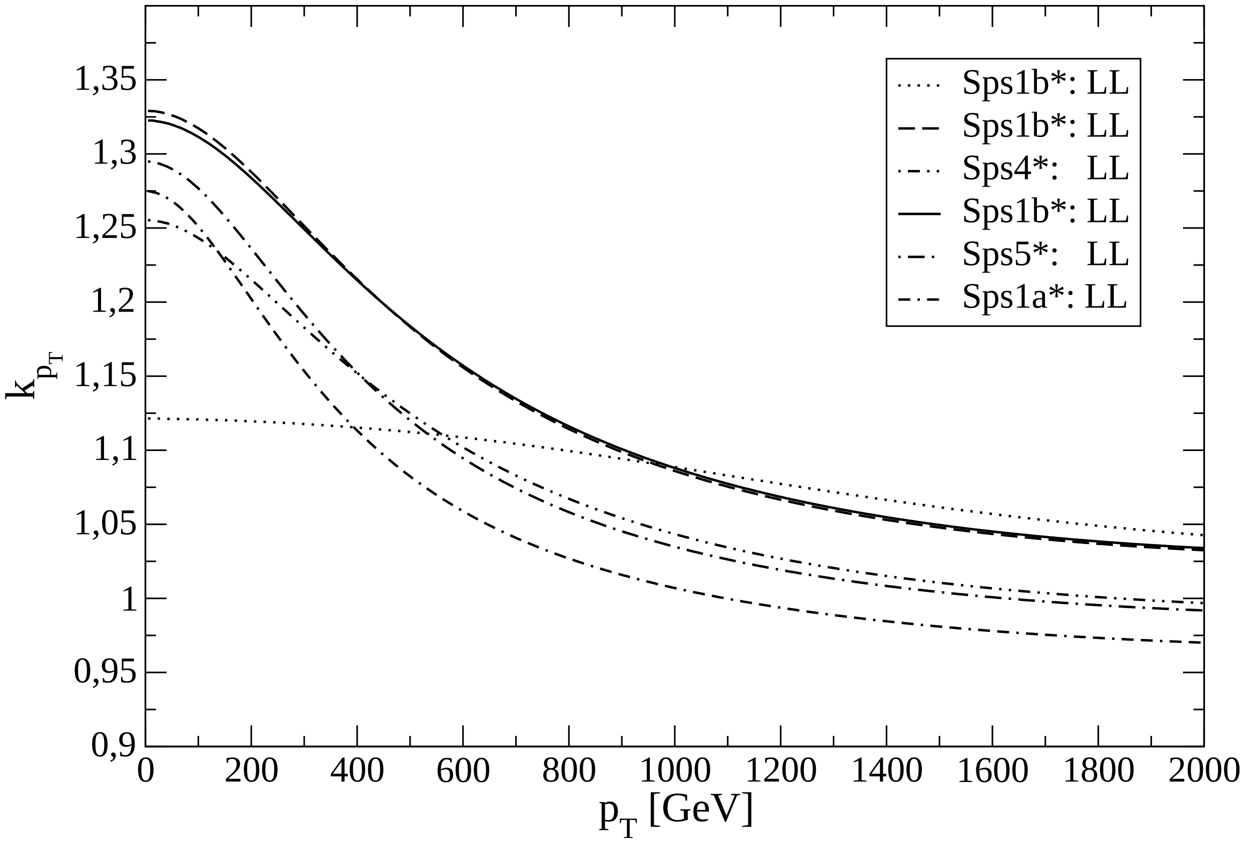

Abbildung 26: The ratio of QCD+EW to pure QCD predictions for the production of two $SU(2)$ doublet (anti–)squarks at the LHC as a function of the squark transverse momentum. We use the same mSUGRA scenarios as in Table 7, but we assume the same averaged mass for all squarks, what is denoted by the star.

First, the relation between the partonic cms energy and squark transverse momentum can be written as

$$\hat{s} = 4\left(m_{\tilde{q}}^2 + \frac{p_T^2}{\sin^2\theta}\right) , \tag{100}$$

for equal squark masses, where θ is the cms scattering angle. The parton flux in the initial state is largest for smallest $\hat{s}$, since this implies small values of Bjorken$-x$. Eq.(100) then shows that configurations where $\sin^2\theta$ is maximal, i.e. where $\cos\theta$ is small, are preferred if p_T is sizable.

On the other hand, the denominators of the $t-$channel propagators can be written as

$$\hat{t} - M_{\tilde{V}}^2 = m_{\tilde{q}}^2 - \frac{\hat{s}}{2}(1 - \beta \cos\theta) - M_{\tilde{V}}^2 \,, \tag{101}$$

where $M_{\tilde{V}}$ is the mass of the exchanged gaugino; the expression for $u-$channel propagators can be obtained by the replacement $\cos\theta \to -\cos\theta$. Therefore these propagators prefer large $\beta|\cos\theta|$; however, $t-$ and $u-$channel propagators prefer different signs of $\cos\theta$. Our discussion in subsection 8.3 showed that the dominant electroweak contributions are due to the interference between $t-$ and $u-$channel diagrams (cf. subsubsection 8.3.1 and Tab. 8, respectively). These cross sections are proportional to a single power of the threshold factor β. The steeply falling pdf's imply that these processes therefore prefer rather small values of β even for small p_T. As a first approximation we can therefore ignore terms $\propto \beta\cos\theta$ in the propagators. The ratio of EW and QCD $t-$ or $u-$channel propagators then becomes

$$\frac{\text{EW}}{\text{QCD}} = \frac{\hat{s}/2 - m_{\tilde{q}}^2 + M_{\tilde{g}}^2}{\hat{s}/2 - m_{\tilde{q}}^2 + M_{\widetilde{W}}^2} \simeq \frac{2p_T^2 + m_{\tilde{q}}^2 + M_{\tilde{g}}^2}{2p_T^2 + m_{\tilde{q}}^2 + M_{\widetilde{W}}^2} \,, \tag{102}$$

where $M_{\widetilde{W}}$ is the mass of the relevant chargino or neutralino. With respect to the propagators Eq.(102) shows just the difference between the pure QCD contributions and the interference terms between electroweak and QCD diagrams. In the case of $m_{\tilde{q}}^2 \sim M_{\tilde{g}}^2 \gg M_{\widetilde{W}}^2$ Eq.(102) shows that there will be an enhancement by a factor of ~ 2 at small p_T. However, there is no enhancement for $m_{\tilde{q}}^2 \gg M_{\tilde{g}}^2$. The latter case is given by the choice of SPS 2, whereas the former case is given by use of all the other mSUGRA scenarios of Fig. 26. This explains the run of the curves for small values of p_T. The observation that the propagator enhancement of Eq.(102) also disappears for $2p_T^2 \gg m_{\tilde{q}}^2$ explains the run of the curves approximately for large values of p_T. But it gives no precise explanation for the three cases of decrease (k_{p_T}) of the differential cross section for large p_T. For this purpose we have to pay attention to two further effects:

On the one hand, all final states of category one with two $SU(2)$ doublet squarks have a helicity flip, leading to amplitudes which are proportional to the mass of the exchanged gaugino. Dimensional arguments then imply that the resulting product of two gaugino masses in these cross sections has to be compensated by an extra factor of p_T^{-2} for large p_T, relative to the processes without helicity flip. But just the processes of the second category with destructive interference terms have no helicity flip and therefore no suppression by means of an extra factor of p_T^{-2} (indeed, these processes are the only ones which requires no helicity flip and have two final state $SU(2)$ doublet squarks). If we would only take into account this argument, all the curves would be less than one for large p_T. One the other hand, all processes of category two have an anti–quark in the initial state; Eq. (100) shows that larger p_T yields larger $\hat{s}$, this again leads to a faster fall of the corresponding parton fluxes in comparison to the case of initial states with two quarks.

So, we have two competing suppression factors for large values of p_T: on the one hand, there is a suppression of electroweak contributions enhancing the cross section – category one processes – due to an extra factor of p_T^{-2}. On the other hand, there is a suppression of category two processes because of more quickly falling pdf's. The latter suppression will be more relevant for larger squark masses, cf. Eq.(100), and indeed, at large p_T we observe the largest (or the least negative) electroweak contributions for scenarios with the heaviest squarks. Thus the scenario

SPS 2 with the heaviest squarks has still an enhancement of $\sim 4\%$ at large p_T. But even for the scenario with smallest squark masses, SPS 1a, electroweak contributions only suppress the cross section by $\sim 3\%$ at large p_T; category two processes do contribute significantly here, but do not really dominate.

8.5 Dependence on the Squark Mass Scale

A closer look at Tab. 7 shows that the electroweak contributions become more important for heavier squarks. Scenario SPS 2 is a special case due to its different $m_0/m_{1/2}$ ratio, but the explanation for this will be the topic of the next subsection. Eq. (98) shows that heavier squarks give rise, on average, to smaller values of β due to the reduction of the phase space. Likewise, the flux of anti–quarks suffers a higher suppression than the quark flux since larger Bjorken–x are required for heavier squarks. All processes where electroweak contributions decrease the total cross section are members of the category two. Here, we have an anti–quark in the initial states as well as a threshold behaviour of $\propto \beta^3$ for the cross section. In contrast, the four processes of category one receiving large positive electroweak contributions have both two quarks as initial states and a cross section which has a threshold behaviour of $\propto \beta$. So higher squark masses increase the importance of the latter processes and decrease the importance of the former processes; this is tantamount to a higher weighting of the processes which lead to an increase of the total cross section after inclusion of the electroweak contributions. Moreover, have a closer look at category three: seven of the ten processes have a suppression due to one initial anti–quark, five of the ten suffers suppression because of their threshold behaviour and three of the ten even have both suppression factors. The cross sections of category three do not receive large positive corrections due to the electroweak contributions but the first eight processes give a sizable contribution to the total cross section. Therefore a relative reduction of the importance of these processes in comparison to the above mentioned category one processes again yields a higher weighting of the positive contributions.

At first glance, Fig. 27 only confirms the observation that electroweak contributions become more important for heavier squarks; it shows the ratio of the total cross section for the production of $SU(2)$ doublet squarks with and without electroweak contributions as function of the average doublet squark mass. These curves have been generated by keeping the ratios of the dimensionful mSUGRA input parameters m_0, $m_{1/2}$ and A_0 fixed, but varying the overall mass scale; this corresponds to the "benchmark slopes" of ref.[39]. Both curves show, as expected, an increase for higher squark masses; but in addition, we can make two further observations: depending on the ratio $m_0/m_{1/2}$, the increase of the cross section can be much different for a fixed squark mass value. In a scenario with relatively large gaugino masses, as in SPS 1a (upper, solid curve), the electroweak contribution can increase the cross section by more than 30% for $m_{\tilde{q}} = 2$ TeV. A scenario with $m_0 = -A_0 = 4.5 m_{1/2}$ (lower, dashed curve) shows the same trend; however, the total electroweak contribution is much smaller in this case, only reaching 13% for $m_{\tilde{q}} = 2$ TeV. The last mentioned curve includes a scenario very similar to SPS 2, however, one cannot generate small squark masses via the corresponding benchmark slope (given in [39]) of SPS 2. The reasons for the different increases of both curves at a fixed squark mass are the same ones which lead to the special position (see note at the beginning of this subsection) of the SPS 2 scenario. So the explanation for the different size of the increase will be given in the next subsection.

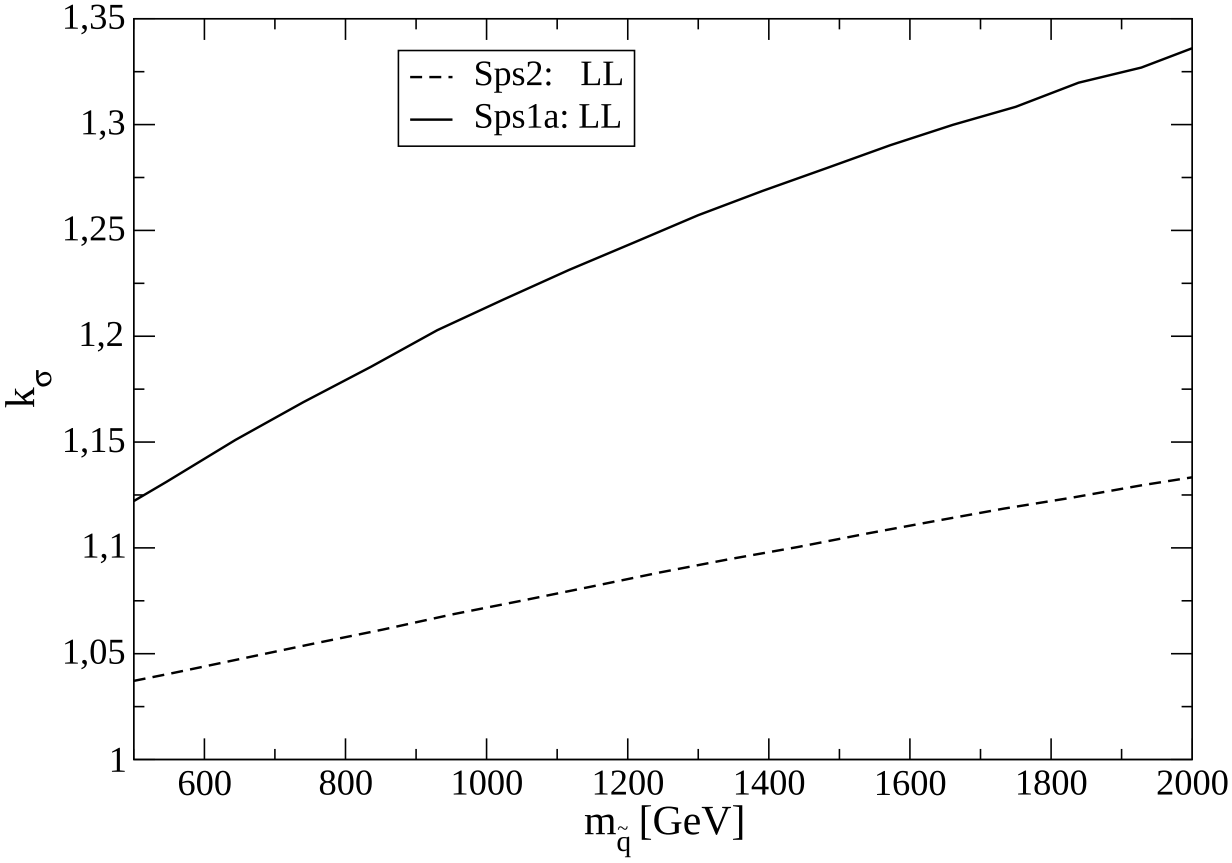

Abbildung 27: The ratio of QCD+EW to pure QCD predictions for the production of two $SU(2)$ doublet (anti–)squarks at the LHC as a function of the squark mass. The upper (lower) curve is for $m_0 = 0.4 m_{1/2}$ ($m_0 = 4.5 m_{1/2}$), with the overall scale of these soft breaking parameters being varied.

The second observation is that the maximal relative size of the electroweak contribution in Fig. 27 exceeds that of the most favorable single process in Table 8 and category one, respectively. Therefore, this cannot only be a result of the above explained different weighting of processes within the three categories for a variation of the squark mass. The crucial point is that for smaller squark masses and larger values of β, respectively, the weighting of processes with squared $t-$ and $u-$channel propagators is higher than that of mixed products of a $t-$ and a $u-$channel propagator in some part of the phase space. Eq.(101) shows that for large $\beta|\cos\theta|$ the $t-$ and $u-$channel propagators give the highest contributions, however, they have different signs with respect to $\cos\theta$. Thus, the part of the phase space with large $|\cos\theta|$ enhances the importance of contributions with squared $t-$ and $u-$channel; the largest contributions of processes with non–mixed propagator–products to the total cross section are just given by pure QCD processes. Higher squark masses and lower values of β, respectively, then lead to an increase of the relative importance of the interference terms having a product of $t-$ and $u-$channel propagator in comparison to contributions with products of the same kind of propagator. This reduces the pure QCD contributions due to both reduction of the positive contributions of squared $t-/u-$channel propagators and enlargement of pure QCD interference terms; the last–mentioned terms are always negative because of the negative color factor, see e.g. Eq.(72). However, the most important positive electroweak contributions of category one are due to interference terms which always have a positive overall sign; therefore the importance of electroweak contributions increases as a whole.

With help of the results of this subsection, we can give two last remarks with respect to our discussion regarding the different absolute sizes of the category one cross sections at the end of subsubsection 8.3.1: first, heavier squarks lead to a higher suppression of the two processes $\tilde{u}_L\tilde{u}_R$ and $\tilde{d}_L\tilde{d}_R$ in comparison to the five processes with equal final squarks because they are proportional to β^3; second, heavier squarks also lead to a higher suppression of initial states with two $d-$quarks because the ratio of $u-$quark pdf to $d-$quark pdf increases for larger values of Bjorken–x, cf. Fig. 22.

8.6 Dependence on the Gaugino Masses

The first part of this subsection gives the explanation for the special position of the SPS 2 scenario within our numerical results. The reason for the, at first glance, to small increase of the total cross section of two final state $SU(2)$ doublet squarks due to electroweak contributions is that the SPS 2 scenario has the smallest gaugino to squark mass ratio. It is about 0.2 whereas all the other scenarios of Tab. 7 do not have a ratio smaller than 0.4. As already several times mentioned, the processes of category one with two $SU(2)$ doublet squarks being responsible for the largest positive new contributions to the total cross sections have interference terms between $t-$ and $u-$channel amplitudes which require a helicity flip. Therefore these amplitudes are proportional to the gaugino mass and the above mentioned contributions are sensitive to the gaugino to squark mass ratio. This explains the different increase of the cross section for the two scenarios of Fig. 27 at fixed squark mass values, too, since the upper curve has larger gaugino masses than the lower curve.

Since all the scenario of Tab. 7 are generated with mSUGRA boundary conditions, we want to say a few more words to the implications of mSUGRA scenarios to our results. The first point is that the relative importance of the electroweak contributions becomes largely insensitive to $m_{1/2}$ (for fixed squark mass) once $m_{1/2} \gtrsim m_0$. The physical squark masses are then essentially independent of m_0, i.e. $m_{\tilde{q}} \propto m_{1/2}$, so that the ratios of gaugino and squark masses become independent of $m_{1/2}$. The second point is that the ratios of the gaugino masses are about $M_1 : M_2 : M_3 \sim 1 : 2 : 7$ at the weak scale. M_1 and M_2 are not one–to–one identical to physical mass eigenstates due to the mixing between electroweak gauginos and higgsinos, however, they are still close to some of the neutralino and chargino masses in many cases. Therefore we expect that the electroweak contributions become larger relative to the total cross section for scenarios without gaugino mass unification; remember that the largest dominant electroweak contributions of category one are proportional to the product of electroweak gaugino mass and gluino mass. The expected dependence of these contributions on the ratio of the gaugino masses is confirmed by Fig. 28, where we show our results as a function of the $SU(2)$ gaugino mass M_2 at the weak scale, normalized to the squark mass, keeping all other parameters fixed.

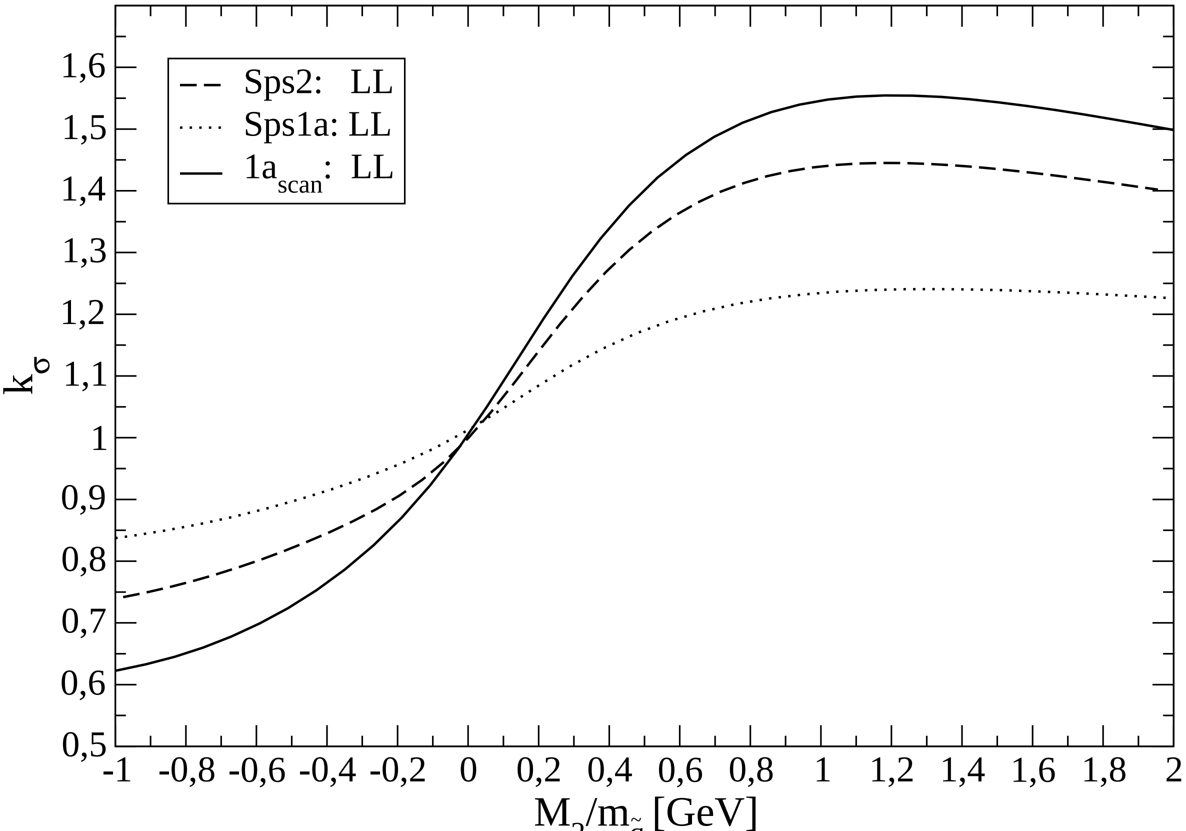

Abbildung 28: The ratio of QCD+EW to pure QCD predictions for the production of two $SU(2)$ doublet (anti–)squarks at the LHC as a function of the ratio of the $SU(2)$ gaugino mass parameter M_2 and the squark mass. The solid and dotted curves are both based on scenario SPS 1a of Table 1, but for the solid curve all soft breaking masses have been scaled up to achieve a squark mass of 2 TeV. The dashed curve is for scenario SPS 2. In all cases M_2 has been varied directly at the weak scale using SPheno [47], leaving all other weak–scale soft breaking parameters unchanged.

This figure shows that the electroweak contributions have a maximum for $M_2 \simeq m_{\tilde{q}}$. The reason for this is that this choice maximizes $M_2/|\hat{t} - M_2^2|$, see Eq.(101). In a scenario with $m_{\tilde{g}} \simeq m_{\tilde{q}}$ and large squark mass (denoted by "1a$_{\text{scan}}$" and solid curve, respectively), this can lead to electroweak contributions in excess of 55%. In scenario SPS 2 (dashed curve) the contributions remain somewhat smaller, partly because of the reduced squark mass, and partly because the lower gluino mass reduces the importance of the interference terms. Not surprisingly, taking $m_{\tilde{g}} \simeq m_{\tilde{q}}$ also maximizes the size of those pure QCD contributions that require a helicity flip. Finally, in scenario SPS 1a with its relatively light squarks (dotted curve) the electroweak contribution never goes much beyond 20%. We saw in Table 9 that in this case the processes of category two still contribute significantly, which have negative electroweak contributions. Since these processes do not require a helicity flip, the absolute size of the electroweak contributions increases monotonically with increasing $|M_2|$. As a result, the dotted curve reaches its maximum for somewhat larger values of M_2; moreover, the maximum is less pronounced.

Fig. 28 shows that the total cross section can also be reduced in comparison to the pure QCD cross section if we choose a negative $SU(2)$ gaugino mass. The reason for this is that the interference terms between $t-$ and $u-$ channel of category one requiring a helicity flip will change their overall sign if one keeps the gluino mass sign positive. The reduction of the cross sections grows with increasing negative M_2 identical to the increase of the cross section for increasing positive M_2. However, the reduction is not that strong as the increase. This is due to the still positive contributions of $U(1)_Y$ gauginos which have kept the sign of their mass. Altogether, we see that the total cross section for the production of two $SU(2)$ (anti–)squarks can change by up to a factor 2.5 as M_2 is varied between $-m_{\tilde{q}}$ and $m_{\tilde{q}}$, if squarks are quite heavy and $m_{\tilde{g}} \simeq m_{\tilde{q}}$.

9 Summary

This Phd thesis deals with supersymmetric particles within the context of astroparticle and collider physics under the topic of the detection of superparticles beyond the SM. The first section motivates why one believes strongly that there is a supersymmetric extension of the SM at the TeV scale. For this purpose, the hierarchy problem and its possible solution within a supersymmetric theory is described in the second part of the introduction. Moreover, the last part of the first section gives a short introduction to Supersymmetry with the aim to familiarize the reader with superparticles, especially with neutralinos and charginos. Sections two to five deal with the detection of UHE particles within the context of astroparticle physics; it based on the use of the matter of Earth and Moon as detector volume, where in the case of UHE neutralino LSPs the Earth acts in addition as a filter against the background of UHE neutrinos. Section two provides an introduction into the mystery of the origin of UHE particles; it can be solved by postulating the existence of X–particles, and the idea of the usage of Moon's matter as detector volume due to the radiation of radio waves because of UHE particle interactions in matter. Since the final intention of chapter one is the calculation of event rates, we present the solutions of the transport equations regarding UHE neutralino LSP and neutrino fluxes in the third section. These solutions are given for processes where the total cross section is dominated by $t-$channel scattering, in case of the neutralino LSP fluxes as well for $s-$channel scattering. The results of this section were published partly in our work [13]. The forth section provides the final formulas for the calculation of event rates with respect to the Earth, including the background of UHE neutrinos, and the Moon. Here, we are taking, as already in the case of the corresponding transport equation, into account the energy loss of tau leptons in matter, before they decay back into neutrinos, after charged current interactions of tau neutrinos. Section five presents our numerical results for the event rates and the dependence of the signals on the angle, which are summarized shortly in the following:

with respect to the use of the Earth as detector volume, we improve on existing analyses [12, 16, 17] in several ways: we use neutralino spectra impinging on Earth calculated with the most complete code for X particle decays [11]; we also carefully include the effects of neutralino propagation through the Earth and for the first time treat the case of higgsino–like neutralino LSPs. We conservatively assume that the progenitor "X particles" are distributed like Dark Matter, in which case most sources are "local", i.e. effects of propagation through the interstellar or intergalactic medium are negligible. We then find detectable event rates in experiments of several teratons scale, like a future satellite experiment as EUSO or OWL, with a duty cycle of $\sim 10\%$ (due to cloudiness) only if the following conditions are satisfied: the lightest neutralino must be a higgsino, rather than a bino; the X particle must decay via a mode which results in a large ratio of neutralino LSP and proton fluxes, like a lepton slepton pair; the X particle mass M_X must be rather close to its lower bound of $\sim 10^{12}$ GeV; the experiment must be able to detect up-going events with visible energy not much above $2 \cdot 10^7$ GeV, so must be able to detect Cerenkov light; if the last condition is not satisfied, most X particles must undergo two–body decays involving at least one slepton and no strongly interacting (s)particle like the most favorable lepton slepton decay of our considered four decay modes. The Cerenkov light detection also allows an upper bound of about 10^6 GeV for the visible energy with corresponding higher event rates for the neutralino LSP fluxes; however, the neutrino induced background is at least two times larger for this lower bound. If M_X is near 10^{16} GeV and the neutralino LSP is higgsino–like one will already need several 1000 teratons·yr to collect an observable event rate, even a monitoring of the *entire* surface of the Earth "only" leads to a detector volume of about 5000 teratons. If M_X is near 10^{12} GeV, the neutralino LSP is bino–like and the threshold of the visible energy is near 10^6 GeV, one will need at least several 100 teratons·yr to collect a respectable event rate. In the worst case, with a bino–like LSP, $M_X \sim 10^{16}$ GeV and a threshold of the visible energy near 10^9 GeV, one would observe less than one event per year even if one monitored the entire surface of the Earth. These numbers improve by about one order of magnitude if X particles are distributed more or less uniformly throughout the Universe; this might be expected if they are confined to cosmic strings or similar topological defects. Recall, however, that scenarios with cosmic strings are constrained by observations of cosmic microwave anisotropies. Therefore next generation experiments, with effective target masses in the several teratons range, would have to be lucky to observe a signal from neutralinos of "top–down" origin. Experiments with a relatively low energy threshold due to the detection of Cerenkov light would stand a much better chance than those with high threshold. Unfortunately, there are many reasonable X particle decay scenarios, especially for bino–like neutralino LSPS, where the neutralino LSP flux will remain invisible to such experiments. The goal of finding an experimentum crucis for top–down models may therefore remain elusive.

Interactions of UHE particles in the Moon's matter give rise to radio waves which might be detected at Earth; an experiment for the detection of Cerenkov light with a duty cycle of $\sim 40\%$, a lower energy threshold of 10^{10} GeV and the ability to cover one half of the Moon's surface was considered. A measurement period of one year already leads to detectable event rates of UHE neutrinos for both X particle masses, 10^{12} and 10^{16} GeV, and all four primary decay modes; the best signal is again given by the primary decay mode into a first generation lepton slepton pair. A measurement period of one year leads in the case of UHE neutralino LSPs to a measureable signal if the X particles have masses close to their lower bound of $\sim 10^{12}$ GeV and decay mainly via the last three primary decay modes and modes with a large ratio of neutralino LSP and proton fluxes, respectively. In case of X particles with mass 10^{16} GeV one would need at least ten years of detection, even for the most favorable scenario, to collect a observable event rate. The event rates for UHE neutralino LSPs and neutrinos have the same order of magnitude for two of the considered primary decay modes for X particles masses of 10^{12} GeV; the disentanglement between the neutralino LSP and neutrino signal is only possible for a radio wave antenna experiment having a angle resolution of at least 0.14°. Parts of our numerical results regarding the first chapter were published in our work [96].

Sections six to eight deal with electroweak contributions, being the result of neutralinos and chargino exchange in the $t-$ and/or $u-$channel as well as electroweak gauge bosons in the $s-$channel, to squark pair production at the LHC. Section six gives reasons for the expectation that squark pair production will play an important role within the processes of two–to–two scattering with supersymmetric final state particles if Supersymmetry exists; one expects to measure the corresponding total cross section with a uncertainty of a few percent; therefore corrections due to NLO QCD corrections are important and electroweak contributions also give rise to sizable changes of the cross section for final states with two $SU(2)$ doublet squarks. Section seven presents our analytical results for the leading–order parton–level squared matrix elements; here, we first give a general formula in terms $s-$, $t-$ and $u-$channel diagrams without specification of the exact initial and final states. This specification and the diagrams and couplings of the different processes, respectively, follows in the remaining part of section seven. Next, section eight presents our numerical results, where we first give our results for the change of the total cross section; then we provide a split–up of the final state processes into three categories in order to enable a more thoroughly discussion of our results, which are again summarized shortly in the following:

The reason for the partly sizable electroweak contributions is the interference between electroweak and QCD interactions. These contributions are most important for two final state $SU(2)$ doublet ($L-$type) squarks; if one has at least one $SU(2)$ singlet ($R-$type) squark, the change of the total cross sections decreases to only a few percent. $SU(2)$ doublet squarks often lead to different final states than singlet squarks which allows to distinguish between these modes experimentally. There are two important classes of processes, especially with respect to the production of two $SU(2)$ doublet squarks, on which we have focused in our results: processes with interference between $t-$ and $u-$channel diagrams which give rise to the dominant new contributions due to participation of electroweak exchange particles. On the other hand, processes with interference between EW $t-$ and QCD $s-$ channel diagrams (or vice versa) which is usually negative. The resulting sign of the electroweak and QCD gaugino mass parameters plays an important role in the case of the former class; if one has equal (opposite) signs of the mass parameters, the corresponding interference is positive (negative). However, the interference of the latter class is independent of the sign of the gaugino mass parameters. This leads to a new, independent handle on the gaugino mass parameters with respect to their relative *signs*. For example, in anomaly–mediated supersymmetry breaking [52] the products of electroweak and QCD gaugino masses are negative. In order to realize this potential, both the experimental and the theoretical uncertainties should be reduced to the 10% level. This is certainly challenging, but should eventually be possible if squarks are not too heavy. Higher squark masses give rise to higher relative electroweak contributions and a larger change of the total cross section, respectively. In case of two produced $SU(2)$ doublet squarks this change can be a increase or reduction of the cross section by more than 50% if we consider: heavy squarks with masses of about 2 TeV, a scenario without gaugino mass unification and a absolute value of the $SU(2)$ gaugino soft breaking mass near $m_{\tilde{q}}$. Electroweak contributions can change the cross section for the production of two $SU(2)$ doublet squarks by more than 30% in the case of scenarios with gaugino mass unification, if the squark masses are again near 2 TeV; about 2 TeV is the upper bound for a sufficiently large cross section for the detection at the LHC. Furthermore, the electroweak contributions peak at small transverse momentum of the produced squark, so it is not possible to subsume them in a constant "$k-$factor".

In case of a two–to–two scattering with an electroweak exchange particle there is no color connection between the two final states because an electroweak particle is a color singlet with respect to $SU(3)_c$, c.g. Tab.1; so all pure electroweak contributions to squark pair production give rise to such final states without color connection. In contrast, the leading order QCD diagrams for squark pair production (gluons and gluinos as exchange particles) always yield squark pairs which are color connected to each other. Therefore the final state squark pairs without color connection can, in principle, lead to a rapidity [102] region being free from QCD radiation and particle activity, respectively. Such a gap with respect to particle activity is called rapidity gap", see, e. g., 2.6 of ref. [102] for a more detailed definition; this is analogous to the predicted rapidity gaps caused by the electroweak exchange particles of the SM like in the case of non–supersymmetric two–jet events produced at hadron colliders [53]. The numerical results of the second chapter were published in our work [97].

To conclude, the LHC will enable the verification of the assumption of new physics beyond the Standard Model at the TeV scale in the near future; the attention of this PhD thesis was focused on a hypothetical supersymmetric extension of the standard model, which would give rise to the existence of superparticles. If these particles exist, the results of this thesis make a contribution to the exciting investigation of the rich new phenomenology caused by Supersymmetry.

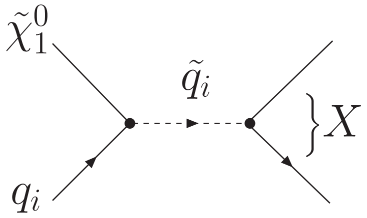

Abbildung 29: $s-$channel Feynman diagram for $\tilde{\chi}_1^0 q_i$ scattering, where $\tilde{q}_i$ is a virtual squark and the symbol X stands for all allowed final states. The arrows indicate the flow of baryon number. An analogous diagram exists for $\tilde{\chi}_1^0 \bar{q}_i$ scattering, with reversed arrows.

A Total and Differential Cross Section for $\tilde{\chi}_1^0$ Scattering

The first part of chapter one shows how to solve the transport equations for the propagation of UHE neutralino through matter. For this purpose we need the total and differential cross section for the scattering of ultra–relativistic neutralinos $\tilde{\chi}_1^0$ on nuclei. Therefore we give a short derivation for the $s-$ and $t-$channel total and differential cross section in the following.

A.1 $s-$channel Cross Section

The $s-$channel contribution to neutralino–quark scattering, $\tilde{\chi}_1^0 q_i \to X$, is described by the Feynman diagram shown in Fig. 29. The total partonic cross section can be written as follows:

$$\hat{\sigma}(\hat{s}) = \pi \frac{1}{|\vec{P}_1^*|^2} \frac{\hat{s}}{(\hat{s} - m_{\tilde{q}_i}^2)^2 + m_{\tilde{q}_i}^2 \Gamma_{\tilde{q}_i}^2} \Gamma(\tilde{q}_i \to q_i + \tilde{\chi}_1^0) \Gamma_{\tilde{q}_i} \, , \tag{103}$$

where $\hat{s}$ is the partonic center–of–mass (c.m.) energy, $m_{\tilde{q}_i}$ is the squark mass, $\vec{P}_1^* = (\hat{s} - m_{\tilde{\chi}_1^0}^2)/(2\sqrt{\hat{s}})$ is the c.m. 3–momentum of the incoming particles, $\Gamma_{\tilde{q}_i}$ is the total decay width of the squark and $\Gamma(\tilde{q}_i \to q_i + \tilde{\chi}_1^0)$ is the partial $\tilde{q}_i \to q_i + \tilde{\chi}_1^0$ decay width. The same expression also holds for $\tilde{\chi}_1^0 \bar{q}_i$ scattering.

The $s-$channel contribution to the total $\tilde{\chi}_1^0-$nucleon scattering cross section can be evaluated from Eq.(103) by convoluting with the appropriate (anti–)quark distribution function and summing over flavors. We use the narrow width approximation,

$$\frac{1}{\left(\hat{s} - m^2\right)^2 + m^2 \Gamma^2} \xrightarrow{\Gamma \to 0} \frac{\pi}{m\Gamma} \delta(\hat{s} - m^2) \, . \tag{104}$$

The convolutions then collapse to simple products [16]:

$$\sigma_s^{\mathrm{tot}} = \frac{\pi}{4} \sum_q \left(|a_{q_L}|^2 + |a_{q_R}|^2 \right) \frac{1}{m_{\tilde{q}}^2} x q(x, Q^2) \, , \tag{105}$$

with

$$x = \frac{m_{\tilde{q}}^2 - m_{\tilde{\chi}_1^0}^2}{2 m_N E_{\rm in}}\,, \tag{106}$$

where $E_{\rm in}$ is the energy of the incident neutralino in the rest frame of the nucleon, and $m_N = (m_p + m_n)/2$ is the nucleon mass. For simplicity we assume equal masses $m_{\tilde{q}}$ for the L and R squarks of a given flavor. In this case left– and right–handed couplings contribute symmetrically, as shown in Eq.(105).[2] This simplified treatment is sufficient as long as squark masses remain free parameters; note also that most SUSY models predict small mass splittings between squarks, at least for the first two generations [57]. Finally, the couplings appearing in Eq.(105) are given by:

$$\begin{aligned} a_{q_L} &= \sqrt{2} g_2 \left(T_{3,q} N_{12} + \frac{\tan\theta_W}{6} N_{11} \right) \quad \text{for } q = u, d, s, c\,; \\ a_{q_R} &= \sqrt{2} g_2 \tan\theta_W Q_q N_{11} \quad \text{for } q = u, d, s, c\,; \\ a_{b_{L,R}} &= a_{d_{L,R}} + \frac{g_2 m_b}{\sqrt{2} m_W \cos\beta} N_{13}\,. \end{aligned} \tag{107}$$

Here, N_{ij} are the entries of the neutralino mixing matrix in the notation of ref.[59], g_2 is the $SU(2)$ coupling constant, θ_W is the weak mixing angle, $T_{3,u} = -T_{3,d} = 1/2$ is the weak isospin, Q_q is the electric charge of quark q in units of the proton charge, m_W is the mass of the $W^\pm$ boson, $\tan\beta$ is the ratio of the Higgs vacuum expectation values, and m_b is the mass of the bottom quark. We ignore the masses of quarks of the first and second generation in these couplings, i.e. we use identical couplings for up and charm quarks, as well as for down and strange quarks. We do include contributions $\propto m_b$ to the couplings of the bottom quark [59].

Note that we do not include the contribution from top (s)quarks in Eq.(105). Since the top quark may not be much lighter than their superpartners, it is more appropriate to treat $\tilde{t}$ production through the $2 \to 2$ scattering reactions

$$\tilde{\chi}_1^0 g \to \tilde{t}\bar{t},\ \bar{\tilde{t}}t\,. \tag{108}$$

We evaluated the corresponding cross section, but found it to be subdominant in all scenarios we considered; this is not very surprising, since it is of higher order in the strong coupling than the cross section (105).

Over most of the parameter space of mSUGRA the lightest neutralino is bino dominated [57, 58]. Since the bino coupling to a sfermion is proportional to the hypercharge of that sfermion, a bino–like $\tilde{\chi}_1^0$ couples predominantly to $SU(2)$ singlet, "right–handed" squarks, whose hypercharges are two (for $\tilde{d}_R$) or four (for $\tilde{u}_R$) times larger than that of the $SU(2)$ doublet squarks; see Eqs.(107). The total $s-$channel cross section is therefore dominated by the production of $SU(2)$ singlet squarks. Since these squarks do not couple to $SU(2)$ gauginos, they will decay directly into $q + \tilde{\chi}_1^0$, if the gluino is heavier than these squarks [49]; in mSUGRA this corresponds to $m_0 \lesssim m_{1/2}$. In this case we can approximate the total $s-$channel contribution as production of on–shell squarks which decay back into $q + \tilde{\chi}_1^0$ final states.

This greatly simplifies the calculation of the cross section differential in the scaling variable $y \equiv 1 - \frac{E_{\rm out}}{E_{\rm in}}$, where $E_{\rm in}$ and $E_{\rm out}$ are the incoming and outgoing $\tilde{\chi}_1^0$ energy in the nucleon rest

---

[2] In general a_{q_L} only contribute to $\tilde{q}_L$ exchange, while a_{q_R} contribute to $\tilde{q}_R$ exchange.

frame. The crucial observation is that squark decays are isotropic in the squark rest frame, which implies

$$\frac{d\sigma_s}{d\cos\theta^*} = \frac{\sigma_s^{\rm tot}}{2}\,, \tag{109}$$

where θ^* is the angle between the ingoing and outgoing $\tilde{\chi}_1^0$ in this frame. In order to get the final expression for the y distribution, we have to boost from the c.m. system into the rest frame of the nucleon. This yields a flat distribution,

$$\frac{d\sigma_s}{dy} = \frac{\sigma_s^{\rm tot}}{y_{\rm max}}\,, \tag{110}$$

where

$$\begin{aligned} y_{\rm max} &= 1 - \frac{m_{\tilde{\chi}_1^0}^2}{m_{\tilde{q}}^2}\,; \\ y_{\rm min} &= 0\,. \end{aligned} \tag{111}$$

In the first Eq.(111) we have used $\hat{s} = m_{\tilde{q}}^2$ for on–shell squark production. Forward scattering in the squark rest frame leads to $E_{\rm out} = E_{\rm in}$, independent of the details of the kinematics; the lower limit for y is therefore always zero. On the other hand, $y = 1$, which requires $E_{\rm out} = 0$, is possible only for $m_{\tilde{\chi}_1^0} \to 0$. Since in mSUGRA $m_{\tilde{\chi}_1^0}^2 \ll m_{\tilde{q}}^2$, $y_{\rm max}$ is indeed quite close to unity. An LSP will then lose on average about half its energy if it undergoes $s-$channel scattering on a nucleon.

A.2 $t-$channel Cross Section

We now turn to the calculation of the $t-$channel contribution to the LSP nucleon scattering cross section. As shown in Fig. 30, there are both W (charged current) and Z exchange (neutral current) diagrams; the former produce an outgoing chargino, while the latter have one of the four neutralinos in the final state. There are additional diagrams with antiquarks in both initial and final state, as well as charged current diagrams producing a negative chargino from scattering off a d or $\bar{u}$ quark. Table 11 shows all possible initial and final states, where we again include five active flavors of quarks in the nucleon.

The partonic total cross section can be obtained by integrating over the scattering angle θ^* in the center–of–mass frame; convolution with the relevant quark distribution functions then yields the $t-$channel contribution to the $\tilde{\chi}_1^0-$nucleon scattering cross section:

$$\sigma_t^{\rm tot}(s) = \sum_q \int_{x_{\rm min}}^1 dx \int_{-1}^{\cos\theta^*_{\rm max}} d\cos\theta^* \frac{1}{32\pi} q(x,Q^2) \frac{|\mathcal{M}|^2 |\vec{P}_2^*(\hat{s})|}{\hat{s}|\vec{P}_1^*(\hat{s})|}\,, \tag{112}$$

where $\hat{s} = 2xE_{\rm in}m_N + m_{\tilde{\chi}_1^0}^2$, and $\vec{P}_1^*$ and $\vec{P}_2^*$ are the three–momenta of the incoming and outgoing particles in the c.m. system, respectively. As usually done in deep–inelastic scattering, We identify the scale Q^2 in the quark distribution functions with the absolute value of the four–momentum $\hat{t}$ exchanged between the participating partons. This causes a minor difficulty: forward scattering ($\cos\theta^* = +1$) leads to $Q^2 = \hat{t} = 0$, where the parton distribution functions

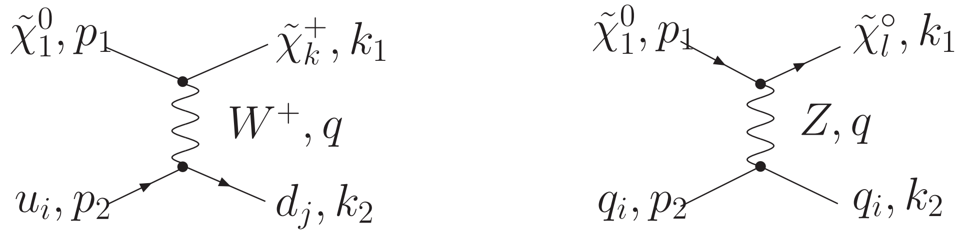

Abbildung 30: Feynman diagrams for $t-$channel neutralino–nucleon scattering. The arrows indicate the flow of baryon number, and $p_{1,2}$, $k_{1,2}$ and q refer to the four–momenta of the initial, final and exchanged particles, respectively.

are not defined. Demanding $Q^2 > Q^2_{\rm min}$ therefore leads to a restriction on the phase space integration:

$$\cos\theta^*_{\rm max} = 1 - \frac{2\hat{s}Q^2_{\rm min}}{\left(\hat{s} - m^2_{\tilde\chi_1^0}\right)\left(\hat{s} - m^2_{\tilde\chi_{\rm out}}\right)}\,, \tag{113}$$

where $\tilde\chi_{\rm out}$ stands for the chargino or neutralino in the final state. This in turn affects the lower bound on the momentum fraction x:

$$x_{\rm min} \;=\; \frac{\frac{1}{2}\left(Q^2_{\rm min} + m^2_{\tilde\chi_{\rm out}} - m^2_{\tilde\chi_1^0}\right) + \sqrt{\frac{1}{4}\left(Q^2_{\rm min} + m^2_{\tilde\chi_{\rm out}} + m^2_{\tilde\chi_1^0}\right)^2 - m^2_{\tilde\chi_{\rm out}} m^2_{\tilde\chi_1^0}}}{2E_{\rm in}m_N}\,, \tag{114}$$

where $E_{\rm in}$ is again the energy of the incoming neutralino in the nucleon rest frame.

The squared matrix elements $|\mathcal{M}|^2$ for the charged current reactions are given by

$$\begin{aligned}\frac{1}{4}\sum_{\rm spins}|\mathcal{M}|^2 \;&=\; \frac{g_2^4}{\left(\hat{t} - M_W^2\right)^2}\Big[2|C^L_{1k}|^2 p_1\!\cdot\! p_2\, k_1\!\cdot\! k_2 + 2|C^R_{1k}|^2 p_1\!\cdot\! k_2\, p_2\!\cdot\! k_1 \\ &\qquad - \left(C^{L*}_{1k}C^R_{1k} + C^L_{1k}C^{R*}_{1k}\right) p_2\!\cdot\! k_2 m_{\tilde\chi_k^\pm} m_{\tilde\chi_l^0}\big]\,,\end{aligned} \tag{115}$$

for the first four cases of Table 11, and

$$\begin{aligned}\frac{1}{4}\sum_{\rm spins}|\mathcal{M}|^2 \;&=\; \frac{g_2^4}{\left(\hat{t} - M_W^2\right)^2}[2|C^L_{1k}|^2 p_1\!\cdot\! k_2\, p_2\!\cdot\! k_1 + 2|C^R_{1k}|^2 p_1\!\cdot\! p_2\, k_1\!\cdot\! k_2 \\ &\qquad - \left(C^{L*}_{1k}C^R_{1k} + C^L_{1k}C^{R*}_{1k}\right) p_2\!\cdot\! k_2 m_{\tilde\chi_k^\pm} m_{\tilde\chi_l^0}]\,,\end{aligned} \tag{116}$$

for the last six cases of Table 11; note that the results (115) and (116) differ by the exchange of the left– and right–handed $W^\pm\tilde\chi_1^0\tilde\chi_k^\mp$ couplings. These couplings are given by [59]

$$\begin{aligned} C^L_{1k} \;&=\; N_{12}\mathcal{V}^*_{k1} - \frac{1}{\sqrt{2}}N_{14}\mathcal{V}^*_{k2}\,, \\ C^R_{1k} \;&=\; N^*_{12}\mathcal{U}_{k1} + \frac{1}{\sqrt{2}}N^*_{13}\mathcal{U}_{k2}\,. \end{aligned} \tag{117}$$

$W^\pm$ exchange		**Z exchange**	
Process	#	Process	#
$\begin{matrix}\tilde{\chi}_1^0\\ u\end{matrix} \longrightarrow \begin{matrix}\tilde{\chi}_k^+\\ d\end{matrix}$	2	$\begin{matrix}\tilde{\chi}_1^0\\ u\end{matrix} \longrightarrow \begin{matrix}\tilde{\chi}_l^\circ\\ u\end{matrix}$	4
$\begin{matrix}\tilde{\chi}_1^0\\ c\end{matrix} \longrightarrow \begin{matrix}\tilde{\chi}_k^+\\ s\end{matrix}$	2	$\begin{matrix}\tilde{\chi}_1^0\\ c\end{matrix} \longrightarrow \begin{matrix}\tilde{\chi}_l^\circ\\ c\end{matrix}$	4
$\begin{matrix}\tilde{\chi}_1^0\\ \bar{u}\end{matrix} \longrightarrow \begin{matrix}\tilde{\chi}_k^-\\ \bar{d}\end{matrix}$	2	$\begin{matrix}\tilde{\chi}_1^0\\ \bar{u}\end{matrix} \longrightarrow \begin{matrix}\tilde{\chi}_l^\circ\\ \bar{u}\end{matrix}$	4
$\begin{matrix}\tilde{\chi}_1^0\\ \bar{c}\end{matrix} \longrightarrow \begin{matrix}\tilde{\chi}_k^-\\ \bar{s}\end{matrix}$	2	$\begin{matrix}\tilde{\chi}_1^0\\ \bar{c}\end{matrix} \longrightarrow \begin{matrix}\tilde{\chi}_l^\circ\\ \bar{c}\end{matrix}$	4
$\begin{matrix}\tilde{\chi}_1^0\\ \bar{d}\end{matrix} \longrightarrow \begin{matrix}\tilde{\chi}_k^+\\ \bar{u}\end{matrix}$	2	$\begin{matrix}\tilde{\chi}_1^0\\ \bar{d}\end{matrix} \longrightarrow \begin{matrix}\tilde{\chi}_l^\circ\\ \bar{d}\end{matrix}$	4
$\begin{matrix}\tilde{\chi}_1^0\\ \bar{s}\end{matrix} \longrightarrow \begin{matrix}\tilde{\chi}_k^+\\ \bar{c}\end{matrix}$	2	$\begin{matrix}\tilde{\chi}_1^0\\ \bar{s}\end{matrix} \longrightarrow \begin{matrix}\tilde{\chi}_l^\circ\\ \bar{s}\end{matrix}$	4
$\begin{matrix}\tilde{\chi}_1^0\\ \bar{b}\end{matrix} \longrightarrow \begin{matrix}\tilde{\chi}_k^+\\ \bar{t}\end{matrix}$	2	$\begin{matrix}\tilde{\chi}_1^0\\ \bar{b}\end{matrix} \longrightarrow \begin{matrix}\tilde{\chi}_l^\circ\\ \bar{b}\end{matrix}$	4
$\begin{matrix}\tilde{\chi}_1^0\\ d\end{matrix} \longrightarrow \begin{matrix}\tilde{\chi}_k^-\\ u\end{matrix}$	2	$\begin{matrix}\tilde{\chi}_1^0\\ d\end{matrix} \longrightarrow \begin{matrix}\tilde{\chi}_l^\circ\\ d\end{matrix}$	4
$\begin{matrix}\tilde{\chi}_1^0\\ s\end{matrix} \longrightarrow \begin{matrix}\tilde{\chi}_k^-\\ c\end{matrix}$	2	$\begin{matrix}\tilde{\chi}_1^0\\ s\end{matrix} \longrightarrow \begin{matrix}\tilde{\chi}_l^\circ\\ s\end{matrix}$	4
$\begin{matrix}\tilde{\chi}_1^0\\ b\end{matrix} \longrightarrow \begin{matrix}\tilde{\chi}_k^-\\ t\end{matrix}$	2	$\begin{matrix}\tilde{\chi}_1^0\\ b\end{matrix} \longrightarrow \begin{matrix}\tilde{\chi}_l^\circ\\ b\end{matrix}$	4
$\sum$	20	$\sum$	40

Tabelle 11: List of processes contributing to $\tilde{\chi}_1^0$−nucleon scattering through the exchange of an electroweak gauge boson in the t−channel, together with the number of different final states. The chargino index k runs from 1 to 2 and the neutralino index l from 1 to 4.

Here, the index k runs from 1 to 2, $\mathcal{U}$ and $\mathcal{V}$ denote the chargino mixing matrices, $m_{\tilde{\chi}_k^\pm}$ is the mass of the outgoing chargino, and $\hat{t} = Q^2 = (k_1 - p_1)^2$; the four–momenta have been defined in Fig. 30. In Eqs.(115) and (116) We have ignored quark flavor mixing, i.e. we replaced the quark mixing matrix by the unit matrix.

Due to the Majorana nature of the neutralinos, neutral current reactions on a quark and antiquark are described by the same matrix element:

$$\begin{aligned}\frac{1}{4}\sum_{\text{spins}} |\mathcal{M}|^2 &= \frac{2}{c_W^4}\frac{g_2^4\left(|g_L^q|^2 + |g_R^q|^2\right)}{\left(t - M_W^2\right)^2}\Big[\left(\left(|N_{l1}^L|^2 + |N_{l1}^R|^2\right)(p_1\cdot p_2\, k_1\cdot k_2 + p_1\cdot k_2\, p_2\cdot k_1)\right.\\ &\qquad \left. - \left(N_{l1}^L N_{l1}^{R*} + N_{l1}^R N_{l1}^{L*}\right) p_2\cdot k_2 m_{\tilde{\chi}_1^0} m_{\tilde{\chi}_l^0}\Big]\right., \qquad (118)\end{aligned}$$

with

$$\begin{aligned} c_W &= \cos\theta_W\,, \\ N_{l1}^L &= \frac{1}{2}\left(-N_{l3}N_{13}^* + N_{l4}N_{14}^*\right)\,, \end{aligned}$$

$$\begin{aligned} N_{l1}^R &= -\left(N_{l1}^L\right)^* , \\ g_L^q &= T_{3,q} - Q_q \sin^2\theta_W , \\ g_R^q &= Q_q \sin^2\theta_W . \end{aligned} \tag{119}$$

The index l in Eqs.(118) and (119) runs from 1 to 4, and Q_q and $T_{3,q}$ have been introduced in Eqs.(107).

We now turn to a discussion of the $y-$distribution of the $t-$channel contribution. The scaling variable y is related to the scattering angle via

$$y = (1 - \cos\theta^*)\,\frac{\hat{s} - m^2_{\tilde{\chi}_{\rm out}}}{2\hat{s}} . \tag{120}$$

The cross section differential in y can therefore be calculated from Eq.(112) by a substitution of variables, and inverting the order of integration:

$$\frac{d\sigma_t}{dy} = \sum_q \int_{x_-}^1 dx q\Big(x, Q^2\Big)\,\frac{|\mathcal{M}|^2}{16\pi(\hat{s} - m^2_{\tilde{\chi}_1^0})} . \tag{121}$$

Eqs.(120) and (113) imply that for given x,

$$y \in \left[\frac{Q^2_{\rm min}}{2xE_{\rm in}m_N},\ 1 - \frac{m^2_{\tilde{\chi}_{\rm out}}}{\hat{s}}\right] . \tag{122}$$

Using $\hat{s} = m^2_{\tilde{\chi}_1^0} + 2xE_{\rm in}m_N$, this gives for the lower bound on the $x-$integration in Eq.(121):

$$x_- = \frac{1}{2E_{\rm in}m_N}\,\min\left(\frac{Q^2_{\rm min}}{y},\ \frac{m^2_{\tilde{\chi}_{\rm out}}}{1-y} - m^2_{\tilde{\chi}_1^0}\right) . \tag{123}$$

Since $Q^2_{\rm min} = 1\ {\rm GeV}^2 \ll m^2_{\tilde{\chi}_1^0}$, for most values of y the lower bound on x is determined from the second term in Eq.(123); the restriction on Q^2 determines x_- only for very small values of y.

Up to this point we have not considered the interference between the $s-$ and $t-$channel contributions. This is suppressed by the following effect: The interference between the $t-$channel gauge boson and $s-$channel squark propagators vanishes at $\hat{s} = m^2_{\tilde{q}}$, where the latter is largest in absolute size, but purely imaginary. Interference can thus only occur for off–shell squark exchange, and is hence of higher order in perturbation theory. These interference contributions can therefore safely be neglected.

B Bino– and Higgsino–like Neutralinos $\tilde{\chi}_1^0$

We derive the solutions of the transport equations and the event rate formulas for scenarios with bino– and higgsino–like neutralino $\tilde{\chi}_1^0$. On this account, we give a short summary of the implications regarding the cross section and four scenarios in the following subsections. We refer to [13] for a more detailed discussion.

B.1 Implications for the Cross Section

Eqs.(117) and (119) show that bino–dominated $\tilde{\chi}_1^0$ states, which have $|N_{12}|$, $|N_{13}|$, $|N_{14}| \ll 1$, have suppressed couplings to gauge bosons. Therefore the $t-$channel contributions are sub-dominant for scenarios with bino–like $\tilde{\chi}_1^0$ and the cross section is dominated by $s-$channel contributinos, repectively. The $t-$channel contribution dominates only at low energies, below the threshold for squark production; however, there the cross section is in any case very small, and any possible signal from UHE LSPs will be masked by the much larger neutrino signal.

In contrast, Eqs.(107) show that a higgsino–dominated $\tilde{\chi}_1^0$ states, with $|N_{11}|$, $|N_{12}| \ll 1$, has very small couplings to light quarks, which suppresses the $s-$channel contribution, whereas $|N_{13}|$, $|N_{14}|$ are sizable and lead to unsuppressed couplings to gauge bosons. Therefore the $t-$channel contributions dominate the total $\tilde{\chi}_1^0-$nucleon scattering cross section for higgsino–like $\tilde{\chi}_1^0$. Scenarios with higgsino–like $\tilde{\chi}_1^0$ have higgsino mass parameter $|\mu|$ significantly smaller than the $SU(2)_L$ and $U(1)_Y$ gaugino mass parameters $|M_2|$ and $|M_1|$. As a result, the second neutralino $\tilde{\chi}_2^0$ and lighter chargino $\tilde{\chi}_1^\pm$ will also be higgsino–like, but $\tilde{\chi}_3^0$, $\tilde{\chi}_4^0$ and $\tilde{\chi}_2^\pm$ will be gaugino–like. Since gauge bosons can only couple to two higgsinos (or, in case of $W^\pm$, to two $SU(2)_L$ gauginos), the production of these heavier neutralino and chargino states is strongly suppressed. The neutral current reaction with $\tilde{\chi}_1^0$ in the final state is also suppressed. This is due to the fact that $|N_{13}| \simeq |N_{14}|$ for higgsino–like LSP, leading to a strong cancellation of the $Z\tilde{\chi}_1^0\tilde{\chi}_1^0$ couplings in Eqs.(119). The total neutral and charged current contributions are therefore dominated by $\tilde{\chi}_2^0$ and $\tilde{\chi}_1^\pm$ production, respectively.

B.2 Scenarios

Table 12.shows three representative mSUGRA scenarios yielding a bino–like state as LSP. We used the public code Softsusy [46] for the calculation of the particle spectra. For simplicity we fix the trilinear interaction parameter $A_0 = 0$ and $\tan\beta = 2$. We choose rather small or moderate values of the scalar and gaugino mass parameters; larger masses yield smaller cross sections, and hence smaller effects from propagation through Earth. Whereas Table 13 shows scenarios with a higgsino–like state as LSP for a non–mSUGRA scenario.

mSUGRA scenarios for Bino–Like $\tilde{\chi}_1^0$				
Scenario	m_0	$m_{1/2}$	$m_{\tilde{\chi}_1^0}$	$m_{\tilde{d}_L}$
D1	80	150	63	365
D2	150	250	104	582
D3	250	450	189	992

Tabelle 12: mSUGRA scenarios for $\tan\beta = 2$, higgsino mass parameter $\mu < 0$ and $A_0 = 0$. m_0 and $m_{1/2}$ are the universal scalar and gaugino mass parameters, respectively. $m_{\tilde{d}_L}$ is the mass of the $SU(2)$ doublet down squark, but all other squark masses have quite similar values. All masses are in GeV.

Scenario for Higgsino–Like $\tilde\chi_1^0\ \tilde\chi_1^0$							
Scenario	$m_{\tilde\chi_1^0}$	$m_{\tilde\chi_2^0}$	$m_{\tilde\chi_3^0}$	$m_{\tilde\chi_4^0}$	$m_{\tilde\chi_1^+}$	$m_{\tilde\chi_2^+}$	GF [%]
H2	300	310	940	970	303	970	1.1

Tabelle 13: Neutralino and chargino masses (in GeV) as well as the gaugino fraction $GF = |N_{11}|^2 + |N_{12}|^2$ for a scenario with higgsino–like $\tilde\chi_1^0$; note that the higgsino fraction is $100\% - GF$.

C Couplings for Squark Pair Production

This appendix gives the explicit expressions for all the couplings appearing in Sec. 7 of Chapter II, using the notation of [43]. We only list couplings of squarks. The corresponding couplings of anti–squarks can be obtained using relations (74) and (78).

C.1 Neutralino and Gluino Couplings

Since gluino and neutralino exchange always occur together, We labeled them with the subscript l, with $l \in \{1,2,3,4\}$ denoting the $l-$th neutralino mass eigenstate and $l = 5$ denoting the gluino. Here we need the left– and right–handed quark–squark–gaugino couplings, generically denoted by a and b, respectively. The relevant **neutralino couplings** are:

$$\begin{aligned}
a_{\tilde\chi_l^0}(\tilde d_{i\alpha}) &= -\delta_{1\alpha}\sqrt{2}g\left(\frac{1}{2}N_{l2}^* - \frac{1}{6}\tan\theta_W N_{l1}^*\right)\,, \\
b_{\tilde\chi_l^0}(\tilde d_{i\alpha}) &= \delta_{2\alpha}\frac{\sqrt{2}}{3}g\tan\theta_W N_{l1}\,, \\
a_{\tilde\chi_l^0}(\tilde u_{i\alpha}) &= \delta_{1\alpha}\sqrt{2}g\left(\frac{1}{2}N_{l2}^* + \frac{1}{6}\tan\theta_W N_{l1}^*\right)\,, \\
b_{\tilde\chi_l^0}(\tilde u_{i\alpha}) &= -\delta_{2\alpha}\frac{2\sqrt{2}}{3}g\tan\theta_W N_{l1}\,. \qquad (124)
\end{aligned}$$

Here $\alpha = 1$ (2) stands for an $L-$ ($R-$)type squark, and N_{l1} and N_{l2} stand for the $U(1)_Y$ (bino) and $SU(2)$ (neutral wino) components of $\tilde\chi_l^0$, respectively. Recall that we ignore quark mass effects, and hence also Yukawa contributions to the neutralino couplings. Finally, g is the $SU(2)$ gauge coupling, and θ_W is the weak mixing angle.

The corresponding **gluino couplings** are:

$$\begin{aligned}
a_{\tilde g}(\tilde d_{i\alpha}) &= -\delta_{1\alpha}g_s\sqrt{2}\,, \\
b_{\tilde g}(\tilde d_{i\alpha}) &= \delta_{2\alpha}g_s\sqrt{2}\,, \\
a_{\tilde g}(\tilde u_{i\alpha}) &= -\delta_{1\alpha}g_s\sqrt{2}\,, \\
b_{\tilde g}(\tilde u_{i\alpha}) &= \delta_{2\alpha}g_s\sqrt{2}\,, \qquad (125)
\end{aligned}$$

where g_s is the $SU(3)$ gauge coupling.

C.2 Chargino Couplings

For a given process, charginos cannot be exchanged in diagrams of the same topology as neutralinos and gluinos. Here the subscript l labeling the exchanged particle therefore only runs from 1 to 2, corresponding to the two chargino mass eigenstates in the MSSM. Their relevant couplings are:

$$\begin{aligned} a_{\chi_l^+}(\tilde{d}_{i\alpha}) &= -gU_{l1}\delta_{1\alpha}\,, \\ b_{\chi_l^+}(\tilde{d}_{i\alpha}) &= 0\,, \\ a_{\chi_l^+}(\tilde{u}_{i\alpha}) &= -gV_{l1}\delta_{1\alpha}\,, \\ b_{\chi_l^+}(\tilde{u}_{i\alpha}) &= 0\,. \end{aligned} \tag{126}$$

The vanishing of the right–handed, $b-$type couplings is again due to our neglect of Yukawa couplings.

C.3 Gauge Boson Couplings

Here ($s-$channel) diagrams with photon, Z boson and gluon exchange always occur together. We therefore labeled these particles with subscript l, $l = 1, 2, 3$ standing for the γ, Z boson and gluon, respectively. e and f represent the left– and right–handed gauge boson–quark–anti-quark couplings,

$$\begin{aligned} e_\gamma(d_i,\bar{d}_i) &= f_\gamma(d_i,\bar{d}_i) = \frac{1}{3} g\sin\theta_W\,, \\ e_\gamma(u_i,\bar{u}_i) &= f_\gamma(u_i,\bar{u}_i) = -\frac{2}{3} g\sin\theta_W\,, \\ e_Z(d_i,\bar{d}_i) &= \frac{g}{\cos\theta_W}\frac{1}{2}\left(1-\frac{2}{3}\sin^2\theta_W\right)\,, \\ f_Z(d_i,\bar{d}_i) &= -\frac{g}{\cos\theta_W}\frac{1}{3}\sin^2\theta_W\,, \\ e_Z(u_i,\bar{u}_i) &= -\frac{g}{\cos\theta_W}\frac{1}{2}\left(1-\frac{4}{3}\sin^2\theta_W\right)\,, \\ f_Z(u_i,\bar{u}_i) &= \frac{g}{\cos\theta_W}\frac{2}{3}\sin^2\theta_W\,, \\ e_g(d_i,\bar{d}_i) &= f_g(d_i,\bar{d}_i) = e_g(u_i,\bar{u}_i) = f_g(u_i,\bar{u}_i) = -g_s\,. \end{aligned} \tag{127}$$

Their couplings to a squark and an anti–squark, generically denoted by c, are:

$$\begin{aligned} c_\gamma(\tilde{d}_{i\alpha},\bar{\tilde{d}}_{i\alpha}) &= \frac{1}{3} g\sin\theta_W\,, \\ c_\gamma(\tilde{u}_{i\alpha},\bar{\tilde{u}}_{i\alpha}) &= -\frac{2}{3}\sin\theta_W\,, \\ c_Z(\tilde{d}_{i\alpha},\bar{\tilde{d}}_{i\alpha}) &= \frac{g}{\cos\theta_W}\frac{1}{2}\left(\delta_{1\alpha}-\frac{2}{3}\sin^2\theta_W\right)\,, \\ c_Z(\tilde{u}_{i\alpha},\bar{\tilde{u}}_{i\alpha}) &= \frac{g}{\cos\theta_W}\frac{1}{2}\left(-\delta_{1\alpha}+\frac{4}{3}\sin^2\theta_W\right)\,, \\ c_g(\tilde{d}_{i\alpha},\bar{\tilde{d}}_{i\alpha}) &= c_g(\tilde{u}_{i\alpha},\bar{\tilde{u}}_{i\alpha}) = -g_s\,. \end{aligned} \tag{128}$$

Note that in the absence of $L-R$ mixing, the couplings listed in Eq.(128) are nonzero only if both the squark and the anti–squark are $SU(2)$ doublets ($\alpha = 1$), or both are singlets ($\alpha = 2$).

Finally, in some cases there are $s-$channel diagrams in which a $W-$boson is exchanged. Its couplings to the initial state are given by

$$\begin{aligned} e_W(d_i, \bar{u}_i) &= e_W(u_i, \bar{d}_i) = -\frac{g}{\sqrt{2}}\,, \\ f_W(d_i, \bar{u}_i) &= f_W(u_i, \bar{d}_i) = 0\,, \end{aligned} \tag{129}$$

and the relevant final state couplings are

$$c_W(\tilde{d}_{i\alpha}, \bar{\tilde{u}}_{i\alpha}) = c_W(\tilde{u}_{i\alpha}, \bar{\tilde{d}}_{i\alpha}) = -\frac{g}{\sqrt{2}}\delta_{1\alpha}\,. \tag{130}$$

Literatur

[1] For reviews, see P. Bhattacharjee and G. Sigl, Phys. Rep. **327**, 109 (2000), astro–ph/9811011; S. Sarkar, hep–ph/0202013; M. Drees, talk at 9th International Symposium on Particles, Strings and Cosmology (PASCOS 03), Mumbai, India, 3-8 Jan 2003, Pramana **62**, 207 (2004), hep–ph/0304030. M. Kachelriess, Comptes Rendus Physique **5**, 441 (2004), hep–ph/0406174.

[2] K. Greisen, Phys. Rev. Lett. **16**, 748 (1966); G.T. Zatsepin and V.A. Kuzmin, JETP Lett. **4**, 78 (1966).

[3] C.T. Hill, Nucl. Phys. **B224**, 469 (1983); D.N. Schramm and C.T. Hill, Contributed paper to *18th Int. Cosmic Ray Conf.*, Bangalore, India, August 1983, Cosmic Ray Conf.1983 v.2, 393; C.T. Hill, D.N. Schramm and T.P. Walker, Phys. Rev. **D36**, 1007 (1987); P. Bhattacharjee, C.T. Hill and D.N. Schramm, Phys. Rev. Lett. **69**, 567 (1992); M. Birkel and S. Sarkar, Astropart. Phys. **9**, 297 (1998), hep–ph/9804285.

[4] HIRES collab., D.J. Bird et al., Phys. Rev. Lett. **71**, 3401 (1993).

[5] J. Ellis, J. Lopez and D.V. Nanopoulos, Phys. Lett. **B247**, 257 (1990); V. Berezinsky and A. Vilenkin, Phys. Rev. Lett. **79**, 5202 1997), astro-ph/9704257; K. Benakli, J.R. Ellis and D.V. Nanopoulos, Phys. Rev. **D59**, 047301 (1999), hep–ph/9803333; K. Hamaguchi, Y. Nomura and T. Yanagida, Phys. Rev. **D58**, 103503 (1998), hep–ph/9805346, and **D59** 063507 (1999), hep–ph/9809426; K. Hamaguchi, K.I. Izawa, Y. Nomura and T. Yanagida, Phys. Rev. **D60**, 125009 (1999), hep–ph/9903207; K. Hagiwara and Y. Uehara, Phys. Lett. **B517**, 383 (2001), hep–ph/0106320. C. Coriano, A.E. Faraggi and M. Plümacher, Nucl. Phys. **B614**, 233 (2001), hep–ph/0107053; J.R. Ellis, V.E. Mayes and D.V. Nanopoulos, Phys. Rev. **D70**, 075015 (2004), hep–ph/0403144.

[6] D.J.H. Chung, E.W. Kolb and A. Riotto, Phys. Rev. **D60** (1999) 0603504, hep–ph/9809453; D.J.H. Chung, P. Crotty, E.W. Kolb and A. Riotto, Phys. Rev. **D64** 043503 (2001), hep–ph/0104100; R. Allahverdi and M. Drees, Phys. Rev. Lett. **89**, 091302 (2002), hep–ph/0203118.

[7] J.R. Ellis, V.E. Mayes and D.V. Nanopoulos, Phys. Rev. **D74**, 115003 (2006), astro–ph/0512303; N. Busca, D. Hooper and E.W. Kolb, Phys. Rev. **D73**, 123001 (2006), astro–ph/0603055.

[8] C.T. Hill and D.N. Schramm, Phys. Lett. **B131**, 247 (1983); P. Gondolo, G. Gelmini and S. Sarkar, Nucl. Phys. **B392**, 111 (1993), hep–ph/9209236; C. Barbot, M. Drees, F. Halzen and D. Hooper, Phys. Lett. **B555**, 22 (2003), hep–ph/0205230.

[9] S.L. Dubovsky and P.G. Tinyakov, JETP Lett. **68**, 107 (1998), hep–ph/9802382; V. Berezinsky and A.A. Mikhailov, Phys. Lett. **B449**, 237 (1999), astro–ph/9810277; G.A. Medina-Tanco and A.A. Watson, Astropart. Phys. **12**, 25 (1999), astro–ph/9903182; N.W. Evans, F. Ferrer and S. Sarkar, Astropart. Phys. **17**, 319 (2002), astro–ph/0103085

[10] V. Berezinsky and M. Kachelriess, Phys. Lett. **B422**, 163 (1998), hep–ph/9709485; Phys. Lett. **B434**, 61 (1998), hep–ph/9803500; and Phys. Rev. **D63**, 034007 (2001), hep–ph/0009053; C. Coriano and A.E. Faraggi, Phys. Rev. **D65**, 075001 (2002), hep–ph/0106326; A. Ibarra and R. Toldra, JHEP **0206**, 006 (2002), hep–ph/0202111; R. Aloisio, V. Berezinsky and M. Kachelriess, Phys. Rev. **D69**, 094023 (2004), hep–ph/0307279.

[11] C. Barbot and M. Drees, Phys. Lett. **B533**,107 (2002), hep–ph/0202072, and Astropart. Phys. **20**, 5 (2003), hep–ph/0211406; C. Barbot, Comput. Phys. Commun. **157**, 63 (2004), hep–ph/0306303.

[12] C. Barbot, M. Drees, F. Halzen and D. Hooper, Phys. Lett. **B563**, 132 (2003), hep–ph/0207133.

[13] S. Bornhauser and M. Drees, Astropart. Phys. **27**, 30 (2007), hep–ph/0603162

[14] F.W. Stecker et al., Nucl. Phys. Proc. Suppl. **136C**, 433 (2004), astro–ph/0408162.

[15] EUSO Collab., Ph. Gorodetzky et al., Nucl. Phys. Proc. Suppl. **151**, 401 (2006), astro–ph/0502187.

[16] L. Anchordoqui, H. Goldberg and P. Nath, Phys. Rev. **D70**, 025014 (2004), hep–ph/0403115.

[17] A. Datta, D. Fargion and B. Mele, JHEP **0509**, 007 (2005), hep–ph/0410176.

[18] M. Takeda et al., Astropart. Phys. **19**, 447 (2003), astro–ph/0209422.

[19] High Resolution Fly's Eye Collab., T. Abu-Zayyad et al., Astropart. Phys. **23**, 157 (2005), astro–ph/0208301.

[20] R.A. Vazquez et al., Astropart. Phys. **3**, 151 (1995); M. Ave, J.A. Hinton, R.A. Vazquez, A.A. Watson and E. Zas, Phys. Rev. Lett. **85**, 2244 (2000), astro–ph/0007386, and Phys. Rev. **D65**, 063007 (2002), astro–ph/0110613; AGASA collab., K. Shinozaki et al., Astrophys. J. **571**, L120 (2002).

[21] R. Ghandhi, C. Quigg, M.H. Reno and I. Sarcevic, Astropart. Phys. **5**, 81 (1996), hep–ph/9512364.

[22] S.I. Dutta, Y. Huang and M.H. Reno, Phys. Rev. **D72**, 013005 (2005), hep–ph/054208.

[23] V. Berezinsky and M. Kachelriess, Phys. Lett. **B422**, 163 (1998), hep–ph/9709485.

[24] See e.g. E. Jeong and G.F. Smoot, astro–ph/0612706.

[25] IceCube Collab., A. Achterberg et al., Astropart. Phys. **26** (2006) 155, astro–ph/0604450; see also http://icecube.wisc.edu/ .

[26] H. Baer and X. Tata, *Weak Scale Supersymmetry: From Superfields to Scattering Events*, Cambridge, UK: Univ. Pr. (2006).

[27] E. Witten, Nucl. Phys. **B188**, 513 (1981); N. Sakai, Z. Phys. **C11**, 153 (1981); S. Dimopoulos and H. Georgi, Nucl. Phys. **B193**, 150 (1981); R.K. Kaul and P. Majumdar, Nucl. Phys. **B199**, 36 (1982).

[28] J. Ellis , S. Kelley and D.V. Nanopoulos, Phys. Lett. B260 (1991) 131; U. Amaldi, W. de Boer and H. Fürstenau, Phys. Lett. B260 (1991) 447; P. Langacker and M. Luo, Phys. Rev.D 44 (1991) 817; C. Giunti, C.W. Kim and U.W. Lee, Mod. Phys. Lett. A6 (1991) 1745.

[29] For a review, see G. Jungman, M. Kamionkowski and K. Griest, Phys. Rep. **267** (1996) 195, hep-ph/9506380.

[30] WMAP Collab., D.N. Spergel et al., Astrophys. J. Suppl. **148**, 175 (2003), astro–ph/0302209; WMAP Collab., D.N. Spergel et al., Astrophys. J. Suppl. **170**, 377 (2007), astro–ph/0603449.

[31] J.A. Grifols and A. Mendez, Phys. Rev. **D26**, 1809 (1982); J.R. Ellis, J.S. Hagelin and D.V. Nanopoulos, Phys. Lett. **B116**, 283 (1982); R. Barbieri and L. Maiani, Phys. Lett. **B117**, 203 (1982); T.C. Yuan, R. Arnowitt, A. H. Chamseddine and P. Nath, Z. Phys. **C26**, 407 (1984); S.P. Martin and J.D. Wells, Phys. Rev. D64 (2001) 035003, hep–ph/0103067.

[32] Muon $g-2$ Collab., G.W. Bennett et al., Phys. Rev. Lett. **89**, 101804 (2002), Erratum–ibid. **89**, 129903 (2002), hep–ex/0208001, and Phys. Rev. Lett. **92**, 161802 (2004), hep–ex/0401008.

[33] M. Davier, S. Eidelman, A. Höcker and Z. Zhang, Eur. Phys. J. **C31**, 503 (2003), hep–ph/0308213; K. Hagiwara, A.D. Martin, D. Nomura and T. Teubner, Phys. Rev. **D69**, 093003 (2004), hep–ph/0312250, and Phys. Lett. **B649**, 173 (2007), hep–ph/0611102; J.F. de Troconiz and F.J. Yndurain, Phys. Rev. **D71**, 073008 (2005), hep–ph/0402285; M. Passera, J. Phys. **G31**, R75 (2005), hep–ph/0411168; F. Jegerlehner, hep–ph/0703125.

[34] J.R. Ellis, S. Heinemeyer, K.A. Olive, A.M. Weber and G. Weiglein, arXiv:0706.0652 [hep-ph].

[35] ATLAS collab., *Detector and physics performance technical design report*, Vol. 2, Ch. 20, CERN–LHCC–99–15; CMS Collab., S. Abdullin et al., J. Phys. **G28**, 469 (2002), hep–ph/9806366.

[36] P.R. Harrison and C.H. Llewellyn Smith, Nucl. Phys. **B213**, 223 (1983); Erratum ibid. **B223**, 542 (1983); S. Dawson, E. Eichten and C. Quigg, Phys. Rev. **D31**, 1581 (1985); H. Baer and X. Tata, Phys. Lett. **B160**, 159 (1985).

[37] W. Beenakker, R. Hopker, M. Spira and P.M. Zerwas, Phys. Rev. Lett. **74**, 2905 (1995), hep–ph/9412272, and Nucl. Phys. **B492**, 51 (1997), hep–ph/9610490.

[38] A.H. Chamseddine, R. Arnowitt and P. Nath, Phys. Rev. Lett. 49 (1982) 970; R. Barbieri, S. Ferrara and C.A Savoy, Phys. Lett. B119 (1982) 343; L. Hall, J. Lykken and S. Weinberg, Phys. Rev. D27 (1983) 2359.

[39] B.C. Allanach et al., presented at *APS / DPF / DPB Summer Study on the Future of Particle Physics (Snowmass 2001)*, Snowmass, Colorado, 30 Jun - 21 Jul 2001, hep–ph/0202233.

[40] K. Choi and H.P. Nilles, JHEP **0704**, 006 (2007), hep–ph/0702146.

[41] G. Bozzi, B. Fuks, B. Herrmann and M. Klasen, arXiv:0704.1826 [hep-ph].

[42] A.T. Alan, K. Cankocak and D.A. Demir, Phys. Rev. **D75**, 095002 (2007), hep–ph/0702289.

[43] J.F. Gunion and H.E. Haber, Nucl. Phys. **B272**, 1 (1986), Erratum-ibid. **B402**, 567 (1993).

[44] Particle Data Group, W.-M. Yao et al., Journal of Physics G **33**, 1 (2006).

[45] CTEQ Collab., H.L. Lai et al., Eur. Phys. J. **C12**, 375 (2000), hep–ph/9903282.

[46] B.C. Allanach, Comput. Phys. Commun. **143**, 305 (2002), hep–ph/0104145.

[47] W. Porod, Comput. Phys. Commun. **153**, 275 (2003), hep–ph/0301101.

[48] H. Baer, A. Mustafayev, H. Summy and Xerxes Tatam arXiv:0708.4003.

[49] H. Baer, V.D. Barger, D. Karatas and X. Tata, Phys. Rev. **D36**, 96 (1987).

[50] M.M. Nojiri and M. Takeuchi, Phys. Rev. **D76**, 015009 (2007), hep–ph/0701190.

[51] B.C. Allanach, M.A. Bernhardt, H.K. Dreiner, C.H. Kom and P. Richardson, Phys. Rev. **D75**, 035002 (2007), hep–ph/0609263.

[52] G.F. Giudice, M.A. Luty, H. Murayama and R. Rattazzi, JHEP **9812**, 027 (1998), hep–ph/9810442; L. Randall and R. Sundrum, Nucl. Phys. **B557**, 79 (1999), hep–th/9810155.

[53] H. Chehime, M.B. Gay Ducati, A. Duff, F. Halzen, A.A. Natale, T. Stelzer and D. Zeppenfeld, Phys. Lett. **B286**, 397 (1992).

[54] Fly's Eye Collab., D. Bird et al., Ap. J. **441** 144 (1995).

[55] AGASA Collab., H. Hayashida et al., Astropart. Phys. **10**, 303 (1999).

[56] For reviews, see P. Bhattacharjee and G. Sigl, Phys. Rep. **327**, 109 (2000), astro–ph/9811011; S. Sarkar, hep–ph/0202013; M. Kachelriess, Comptes Rendus Physique **5**, 441 (2004), hep–ph/0406174.

[57] M. Drees, R.M. Godbole and P. Roy, *Theory and Phenomenology of Sparticles*, World Scientific Publishing Company (2004).

[58] A. Djouadi, M. Drees and J.-L. Kneur, hep–ph/0602001.

[59] J.F. Gunion and H.E. Haber, Nucl. Phys. **B272**, 1 (1986).

[60] V.A. Naumov and L. Perrone, Astropart. Phys. **10**, 239 (1999), hep–ph/9804301.

[61] S.I. Dutta, M.H. Reno and I. Sarcevic, Phys. Rev. **D61**, 053003 (2000), hep–ph/9909393, and Phys. Rev. **D62**, 123001 (2000), hep-ph/0005310.

[62] E. Reya and J. Rödiger, Phys. Rev. **D72**, 053004 (2005), hep–ph/0505218.

[63] O. Stal, J. Bergman, B. Thide, L. K. S. Daldorff and G. Ingelman, Phys. Rev. Lett. **98** (2007) 071103 [arXiv:astro-ph/0604199].

[64] C. W. James and R. J. Protheroe, arXiv:0802.3562 [astro-ph].

[65] N. G. Lehtinen, P. W. Gorham, A. R. Jacobson and R. A. Roussel-Dupre, Phys. Rev. D **69** (2004) 013008 [arXiv:astro-ph/0309656].

[66] K. Mitsui, Phys. Rev. D **45** (1992) 3051.

[67] E. V. Bugaev and Yu. V. Shlepin, Phys. Rev. D **67** (2003) 034027 [arXiv:hep-ph/0203096].

[68] G. A. Askaryan, Sov. Phys. JETP **14**,441 (1962); **21**, 658 (1965)

[69] D. Zavrtanik and D. Veberic [Pierre Auger Collaboration], Nucl. Phys. Proc. Suppl. **175-176** (2008) 213.

[70] J. Abraham *et al.* [Pierre Auger Collaboration], Astropart. Phys. **29** (2008) 188 [arXiv:0712.2843 [astro-ph]].

[71] C. T. Hill, D. N. Schramm and T. P. Walker, Phys. Rev. D **36**, 1007 (1987).

[72] P. Bhattacharjee, C. T. Hill and D. N. Schramm, "Grand unified theories, topological defects and ultrahigh-energy cosmic Phys. Rev. Lett. **69**, 567 (1992).

[73] R. D. Dagkesamanskii and I. M. Zheleznyk, Sov. Phys. JETP **50**, 233 (1989).

[74] P. W. Gorham et al., PRL 93 (2004) 041101; T. H. Hankins, R. D. Ekers, J. D. O'Sullivan, MNRAS 283 (1996) 1027; A. R. Beresnyak, R. D. Dagkesamanskii, I. M. Zheleznykh, A. V. Kovalenko, V. V. Oreshko, Astronomy Reports 49 (2005) 127; E. Zas, F. Halzen and T. Stanev, "Electromagnetic pulses from high-energy showers: Implications for neutrino Phys. Rev. D **45**, 362 (1992); J. Alvarez-Muniz and E. Zas, "Prospects for radio detection of extremely high energy cosmic rays and AIP Conf. Proc. **579**, 128 (2001) [arXiv:astro-ph/0102173]; P. W. Gorham, K. M. Liewer, C. J. Naudet, D. P. Saltzberg and D. R. Williams, arXiv:astro-ph/0102435; A. R. Beresnyak, arXiv:astro-ph/0310295; C. W. James, R. M. Crocker, R. D. Ekers, T. H. Hankins, J. D. O'Sullivan, R. J. Protheroe, MNRAS 379 (2007) 3.

[75] M. Drees, arXiv:hep-ph/9611409.

[76] I. J. R. Aitchison, "Supersymmetry in particle physics: An elementary introduction,"

[77] M. Nagano and A. A. Watson, Rev. Mod. Phys. **72** (2000) 689.

[78] M. E. Peskin and D. V. Schroeder, “An Introduction To Quantum Field Theory,” *Reading, USA: Addison-Wesley (1995) 842 p*

[79] E. Witten, Nucl. Phys. B **188** (1981) 513; M. Veltmann, Act. Phys. Polon **B12** (1981) 437-57; R. K. Kaul, Phys. Lett. B **109** (1982) 19.

[80] R. Haag, J. T. Lopuszanski and M. Sohnius, Nucl. Phys. B **88** (1975) 257.

[81] S. R. Coleman and J. Mandula, Phys. Rev. **159** (1967) 1251.

[82] G. Abbiendi *et al.* [OPAL Collaboration], Eur. Phys. J. C **8** (1999) 255 [arXiv:hep-ex/9809031].

[83] A. C. Kraan, arXiv:hep-ex/0505002.

[84] S. M. Wang [CDF Collaboration], arXiv:0705.2896 [hep-ex].

[85] T. P. Cheng and L. F. Li, “Gauge Theory Of Elementary Particle Physics,” *Oxford, Uk: Clarendon (1984) 536 P. (Oxford Science Publications)*

[86] K. Inoue, A. Kakuto, H. Komatsu and S. Takeshita, Prog. Theor. Phys. **71** (1984) 413.

[87] S. L. Glashow, Nucl. Phys. **22** (1961) 579; S. Weinberg, Phys. Rev. Lett. **19** (1967) 1264; A. Salam, in Ëlementary Particle Theory: Relativistic Groups and Analyticity (Nobel Symposium No. 8) ed. N. Svartholm (Stockholm, Almqvist and Wiksell) (1968) 367; G. ’t Hooft, Nucl. Phys. B **35** (1971) 167; P. W. Higgs, Phys. Rev. Lett. **13** (1964) 508, Phys. Rev. **145** (1966) 1156.

[88] F. Halzen and A. D. Martin, “Quarks And Leptons: An Introductory Course In Modern Particle Physics,” *New York, Usa: Wiley (1984) 396p*; D. J. Griffiths, “INTRODUCTION TO ELEMENTARY PARTICLES,” *NEW YORK, USA: WILEY (1987) 392p*

[89] B. Mele, arXiv:hep-ph/9312285.

[90] S. Ask, arXiv:hep-ex/0305007.

[91] E. Nagy [CDF and D0 Collaborations], Acta Phys. Polon. B **38** (2007) 545.

[92] J. L. Rosner, arXiv:hep-ph/0108195.

[93] LHC Home Page: “http://lhc.web.cern.ch/lhc/”.

[94] Tevatron Main Page: “http://www-bdnew.fnal.gov/tevatron/”.

[95] Link: “http://math.ucr.edu/home/baez/physics/General/open_questions.html#particle”

[96] S. Bornhauser and M. Drees, Phys. Lett. B **650** (2007) 407 [arXiv:0704.3934 [hep-ph]].

[97] S. Bornhauser, M. Drees, H. K. Dreiner and J. S. Kim, Phys. Rev. D **76** (2007) 095020 [arXiv:0709.2544 [hep-ph]].

[98] Link: “http://www.astrolink.de/p012/p01208/index.htm”

[99] J. L. Goity and M. Sher, Phys. Lett. B **346** (1995) 69 [Erratum-ibid. B **385** (1996) 500] [arXiv:hep-ph/9412208].

[100] H. K. Dreiner, arXiv:hep-ph/9707435.

[101] U. Nierste, Int. J. Mod. Phys. A **21** (2006) 1724 [arXiv:hep-ph/0511125].

[102] R. B. Appleby, arXiv:hep-ph/0311210.

[103] T. Sjostrand, S. Mrenna and P. Skands, "PYTHIA 6.4 physics and manual," JHEP **0605** (2006) 026 [arXiv:hep-ph/0603175].

[104] J. L. Hewett, arXiv:hep-ph/9810316.

[105] see, e. g., 3.7 of S. Weinberg, "The Quantum theory of fields. Vol. 1: Foundations," *Cambridge, UK: Univ. Pr. (1995) 609 p*